

VOLUME 37

OCTOBER 1959

NUMBER 10

Canadian Journal of Physics

Editor: H. E. DUCKWORTH

Associate Editors:

L. G. ELLIOTT, *Atomic Energy of Canada, Ltd., Chalk River*
J. S. FOSTER, *McGill University*
G. HERZBERG, *National Research Council of Canada*
L. LEPRINCE-RINGUET, *Ecole Polytechnique, Paris*
B. W. SARGENT, *Queen's University*
G. M. VOLKOFF, *University of British Columbia*
W. H. WATSON, *University of Toronto*
G. A. WOONTON, *McGill University*

Published by THE NATIONAL RESEARCH COUNCIL
OTTAWA CANADA

CANADIAN JOURNAL OF PHYSICS

Under the authority of the Chairman of the Committee of the Privy Council on Scientific and Industrial Research, the National Research Council issues **THE CANADIAN JOURNAL OF PHYSICS** and five other journals devoted to the publication, in English or French, of the results of original scientific research. Matters of general policy concerning these journals are the responsibility of a joint Editorial Board consisting of: members representing the National Research Council of Canada; the Editors of the Journals; and members representing the Royal Society of Canada and four other scientific societies.

EDITORIAL BOARD

Representatives of the National Research Council

- | | |
|--|--|
| I. McT. Cowan, <i>University of British Columbia</i> | H. G. Thode (Chairman), <i>McMaster University</i> |
| A. Gauthier, <i>University of Montreal</i> | D. L. Thomson, <i>McGill University</i> |

Editors of the Journals

- | | |
|---|--|
| D. L. Bailey, <i>University of Toronto</i> | K. A. C. Elliott, <i>Montreal Neurological Institute</i> |
| T. W. M. Cameron, <i>Macdonald College</i> | Léo Marion, <i>National Research Council</i> |
| H. E. Duckworth, <i>McMaster University</i> | R. G. E. Murray, <i>University of Western Ontario</i> |

Representatives of Societies

- | | |
|---|--|
| D. L. Bailey, <i>University of Toronto</i> | K. A. C. Elliott, <i>Montreal Neurological Institute</i> |
| Royal Society of Canada | Canadian Physiological Society |
| T. W. M. Cameron, <i>Macdonald College</i> | P. R. Gendron, <i>University of Ottawa</i> |
| Royal Society of Canada | Chemical Institute of Canada |
| H. E. Duckworth, <i>McMaster University</i> | R. G. E. Murray, <i>University of Western Ontario</i> |
| Royal Society of Canada | Canadian Society of Microbiologists |
| Canadian Association of Physicists | T. Thorvaldson, <i>University of Saskatchewan</i> |
| | Royal Society of Canada |

Ex officio

- Léo Marion (Editor-in-Chief), *National Research Council*
J. B. Marshall (Administration and Awards), *National Research Council*

Manuscripts for publication should be submitted to Dr. H. E. Duckworth, Editor, Canadian Journal of Physics, Hamilton College, McMaster University, Hamilton, Ontario.
For instructions on preparation of copy, see **NOTES TO CONTRIBUTORS** (back cover).

Proof, correspondence concerning proof, and orders for reprints should be sent to the Manager, Editorial Office (Research Journals), Division of Administration and Awards, National Research Council, Ottawa 2, Canada.

Subscriptions, renewals, requests for single or back numbers, and all remittances should be sent to Division of Administration and Awards, National Research Council, Ottawa 2, Canada. Remittances should be made payable to the Receiver General of Canada, credit National Research Council.

The journals published, frequency of publication, and prices are:

Canadian Journal of Biochemistry and Physiology	Monthly	\$9.00 a year
Canadian Journal of Botany	Bimonthly	\$6.00 a year
Canadian Journal of Chemistry	Monthly	\$12.00 a year
Canadian Journal of Microbiology	Bimonthly	\$6.00 a year
Canadian Journal of Physics	Monthly	\$9.00 a year
Canadian Journal of Zoology	Bimonthly	\$5.00 a year

The price of regular single numbers of all journals is \$2.00.



Canadian Journal of Physics

Issued by THE NATIONAL RESEARCH COUNCIL OF CANADA

VOLUME 37

OCTOBER 1959

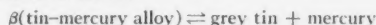
NUMBER 10

THE GREY TIN \rightleftharpoons WHITE TIN TRANSITION IN TIN-MERCURY ALLOYS¹

R. W. SMITH

ABSTRACT

The characteristics of the transition between white tin (β) and the grey modification (α) in zone-refined tin containing various amounts of mercury have been investigated. From dilatometric measurements, it is shown that the transition temperature of the reaction:



is $-8.15^\circ \pm 0.1^\circ$ C. Above this temperature, mercury will attack grey tin to form a white tin amalgam. The compound HgSn_{12} , previously reported not to undergo transformation, is shown to transform below this temperature. Measurements are given of the rates of growth of islands of grey tin on the surfaces of a number of tin-mercury alloys at -30° C. These indicate that the rate of $\beta \rightarrow \alpha$ transformation is virtually independent of the mercury content of the alloy.

The results are discussed and a mechanism is advanced to account for the large displacement of the $\alpha \rightleftharpoons \beta$ transition temperature observed when mercury is alloyed with tin in contrast to the small changes brought about by other additions.

1. INTRODUCTION

The tin-mercury system is of particular interest in a study of the $\alpha \rightleftharpoons \beta$ transformation in tin because mercury will react with white tin (β) for a considerable interval below the transition temperature. Thus, a number of observations on the transformation characteristics of this system have been made by the author during wider studies of this transition.

Earlier, Groen and Burgers (1954) reported the formation of compact pieces of grey tin in contrast to the fragmentary product usually obtained when tetragonal white tin is transformed into the diamond cubic grey modification. Further investigation revealed that this compact nature had resulted, in part, from mercurial contamination (Groen 1954; Hall 1955). Groen also reports that the hexagonal phase, HgSn_{12} , formed in β -tin when mercury is present in excess of 0.2 at.%, is unchanged upon transformation of the tetragonal phase.

More recently, Ewald and Tufte (1958, 1959) observed that free mercury appears upon transformation of a tin-mercury alloy. This enabled them to produce single crystals of grey tin for semiconductor studies, containing

¹Manuscript received June 2, 1959.

Contribution from the Department of Metallurgical Engineering, University of Toronto, Toronto, Ontario.

0.001 at.% or less of mercury by deposition from a supersaturated solution of tin in mercury at temperatures between -20 and -30°C . They report that mercury will suddenly attack these grey tin crystals to form a white tin solid solution if the temperature rises above 1°C .

Since a number of the above observations appeared at variance with the author's, a more thorough study has been made.

2. EXPERIMENTAL PROCEDURE AND OBSERVATIONS

(a) *The $\alpha \rightleftharpoons \beta$ Transition Temperature*

The transition temperature of the tin-mercury system, i.e., that temperature at which the β -alloy is in equilibrium with all its transformation products, was investigated as follows:

Alloys were prepared from zone-refined tin* and high-purity mercury†:

Alloy Hg 1	0.1 at. % Hg
Alloy Hg 2	6.0 at. % Hg
Alloy Hg 3	20.2 at. % Hg

Alloy Hg 2 was found to be much harder than Hg 1, whilst Hg 3 was weak and brittle, its surface being wet with mercury.

Three glass dilatometers were used, each containing a 5-g specimen with xylene as the inert fluid (Smith and Raynor 1957). All had a 2-mm diameter capillary column and, after being sealed, they were calibrated from -20° to $+50^{\circ}\text{C}$. Exposure at -27°C for a few days resulted in a visually complete transformation. Slight crumbling occurred in specimen T81 (alloy Hg 1), T82 showed a few large cracks but was little changed in shape, and T83 (Hg 3) was now composed of large sponge-like lumps. Droplets of mercury were also seen on the latter two specimens.

The volume changes which had accompanied $\beta \rightarrow \alpha$ transformation were evaluated at -10°C and are shown in Table I, together with those computed for complete transformation to pure grey tin and free mercury. Densities for

TABLE I
Progress of $\beta \rightarrow \alpha$ transformation in tin-mercury alloys*

Specimen	T81	T82	T83
Mercury content, at. %	0.1	6.0	20.2
' β ' density, g/cc	7.31	7.66	8.70
Specimen weight, g	5.065	5.078	5.735
Measured volume increase, cc	0.188	0.159	0.147
Calculated volume increase, cc	0.188	0.170	0.165
Calculated retained ' β ', † %	<1	6.5	11.2
Measured volume change as % ‡ original ' β ' volume	27.1	24.0	22.2

*Calculated for -10°C .

†The assigned accuracy of these experiments is 1%.

‡27.1% for pure tin.

*Vulcan extra pure tin (99.998%) was zone-refined to a purity of 99.9999% Sn (as indicated by $\beta \rightarrow \alpha$ transformation rates and analysis).

†Analar Reagent (>99.999% Hg).

pure tin of 5.75 g/cc for α (Thewlis and Davey 1954) and 7.31 g/cc for β (Lee and Raynor 1954) have been used in these calculations.

Following this, the dilatometers were placed in a thermostat at -4.8°C , the levels of the menisci being noted at regular intervals. After 18 hours, they were returned to a refrigerator at -27°C . The observed volume contractions were interpreted as transformation of α -tin, 0% in T81, 35% in T82, and 100% in T83, of that calculated in Table I. This was then repeated at other temperatures, always allowing at least 24 hours between successive tests. The results are shown in Table II. Clearly, mercury begins to attack grey tin just below -8°C and reaction will go to completion comparatively swiftly at temperatures above -4.8°C .

TABLE II

The effect of temperature on the $\alpha \rightarrow \beta$ transformation in tin-mercury alloys

Temp., $^\circ\text{C}$	Test duration, hr	Order of test	% of α transformed		
			T81, 0.1 at.% Hg	T82, 6.0 at.% Hg	T83, 20.2 at.% Hg
+8.0	72	7	<2	35	100
-4.8	18	1	0	35	100
-6.6	12	4	0	15	23
-7.5	24	5	0	14	5
-8.0	140	6	0	2	1
-8.5	20	3	0	0	0
-10.0	24	2	0	0	0

NOTE: All specimens rested at -27°C for 24 hours between tests.

To establish more closely the temperature at which mercury will begin to react with grey tin, 70-g samples of alloys Hg 1, Hg 2, and Hg 3 were carried through the above procedure in dilatometers with 1-mm capillary columns, but no resting period was allowed between tests. Table III contains the results.

TABLE III

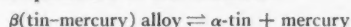
The transition temperature of the $\alpha \rightleftharpoons \beta$ transformation in tin-mercury alloys

Temp., $^\circ\text{C}$	Test duration, hr	Order of test	Change in meniscus height, cm		
			T28, 0.1 at.%	T41, 6.0 at.%	T42, 20.2 at.%
-7.8	26	2	<0.1	-4.7	-4.2
-8.0	22	1	<0.1	-2.4	-0.7
-8.3	18	3	<0.1	+3.0	+3.5
-8.3	120	4*	<0.1	+3.8	+2.1

NOTE: Transition temperature is $-8.15^\circ \pm 0.1^\circ\text{C}$.

*The final positions assumed by the menisci during test 4 were those occupied at this temperature at the beginning of these tests.

Negative signs indicate a falling meniscus and $\alpha \rightarrow \beta$ transformation, a change of meniscus position of 3 cm being equivalent to approximately 1% transformation. The transition temperature of the reaction:



is $-18.5^\circ \pm 0.1^\circ\text{C}$.

(b) The Linear Rate of $\beta \rightarrow \alpha$ Transformation

The effect of mercury content on the linear rate of phase-boundary displacement was determined by inoculating small sections of white tin (approximately $1.5 \times 1.5 \times 0.5$ cm) with grey tin and maintaining them at -30°C . After a grey tin wart had become established, its boundary positions were noted at regular intervals to enable the rate of advance of a single α - β interface to be calculated for each specimen. These are shown in Table IV.

TABLE IV
Linear rate of $\beta \rightarrow \alpha$ transformation in tin-mercury alloys at -30°C

Composition	Rate of transformation ($\pm 10\%$), mm/hr
Zone-refined tin (99.9999% Sn)	2.0
Zone-refined tin + 0.1 at.% Hg	0.23
Zone-refined tin + 6.0 at.% Hg	0.24
Zone-refined tin + 20.2 at.% Hg	0.20
Vulcan extra pure tin (99.998% Sn)	1.2
Vulcan extra pure tin + 0.25 at.% Hg	0.24

It is seen that the presence of mercury in zone-refined tin reduces the rate of $\beta \rightarrow \alpha$ transformation considerably, but that this reduction is virtually independent of mercury concentration (for the range studied). Also, the rate of transformation of Vulcan tin, whose principal impurity is lead, is reduced by mercury to that of the other alloys.

3. DISCUSSION

From the tin-mercury phase diagram (Tin Research Institute 1949), alloy Hg 2 would appear to consist entirely of the compound HgSn_{12} . Yet this alloy underwent almost complete $\beta \rightarrow \alpha$ transformation, thus establishing that HgSn_{12} does transform, with the ejection of free mercury. Also, the work of Section 2(a) shows conclusively that the temperature at which mercury will attack grey tin is $-8.15^\circ \pm 0.1^\circ\text{C}$, significantly lower than that reported by Ewald and Tufte. Absence of transformation of HgSn_{12} reported by Groen (1954) was probably due to experiments being carried out above this temperature, any mercury rejected during transformation of the tetragonal phase forming more of this compound. (Hexagonal crystals, HgSn_{12} , always form from β -tin and mercury above -10°C (Hansen 1936).)

It is of interest to note that in other experiments performed with alloy Hg 1 a transition temperature of 12.9°C was observed (Smith (to be published))—a value which lies in the range expected for dilute tin alloys (Raynor and Smith 1958). From this and the evidence in Tables II and III, it may be concluded that any mercury ejected during $\beta \rightarrow \alpha$ transformation of a tin-mercury alloy will recombine with some of the grey tin to form an amalgam as the temperature rises above -8.15°C . The remainder of the grey tin will then begin to transform to the white modification at 12.9°C . The volume changes observed in tests 1 and 7 of Table II would further suggest that the average composition of the new amalgam formed at these temperatures corresponds to the formula HgSn_5 .

In other studies by the author (to be published), the rate at which mercury will attack grey tin is considerably reduced in tin-germanium alloys. A droplet of mercury was placed on the surface of a coherent piece of the grey modification of a 1 wt.% tin-germanium alloy at 25° C. No change was observed for about 48 hours, after which amalgamation gradually took place. It is presumed that the presence of the covalent germanium increased the stability of the grey tin bonds and so reduced the rate of attack. Ewald (1954) reported that 0.75% germanium will also render grey tin stable at +50° C.

The results of Table IV are of particular interest for, apparently, as the α -phase advances into a tin-mercury alloy, mercury is rejected at the α - β interface. This mercury-enriched boundary layer can only have a limited width and so, as transformation proceeds and further mercury is rejected, regions of free mercury will be created behind the interface, probably appearing in cracks in the grey tin matrix. The independence of transformation rate upon mercury content would suggest that the governing factor is the diffusion rate of tin atoms through the mercury-enriched α - β phase boundary.

Since the presence of lead or mercury reduces the rate of $\beta \rightarrow \alpha$ transformation in zone-refined tin, the rate in the Vulcan extra pure tin-mercury alloy would be expected to be lower than in the zone-refined tin-mercury alloys. The similarity of the experimental values would suggest that the inhibiting actions of lead and mercury are not additive, that of the lead being reduced by the latter. This view is supported by Groen's report (1954) that the presence of mercury in 0.03% lead-tin alloy actually increases the previously very small rate of transformation. The following mechanism is suggested to account for this.

Any material present in the white tin but insoluble in the α -phase will be rejected at the α - β phase boundary and provide a barrier to its free movement. If, however, the inhibiting impurity atom is rejected, together with mercury, into the mercury-enriched interface, continuing transformation will result in it being transported, by diffusion, along the boundary layer until it can be deposited in a pocket of free mercury. Thus, the inhibiting action of α -insoluble impurities will be greatly reduced by the presence of mercury.

The expulsion of mercury when a tin-mercury alloy transforms provides a considerable clue to understanding the $\alpha \rightleftharpoons \beta$ transformation in tin generally. It supports the assumption made above that covalent grey tin can dissolve only trace amounts of solute with metallic bonding. The necessary rejection of such solute on $\beta \rightarrow \alpha$ transformation of tin alloys would thus tend to reduce both the thermodynamic instability of the white tin when below its transition temperature and also the rate of conversion upon transformation, both of which are observed. Also, it is extremely helpful in an understanding of the very small effect that most metallic alloying additions have on the transition temperature of pure tin (Raynor and Smith 1958). Upon initial $\beta \rightarrow \alpha$ transformation, presumably most of the solute is rejected and rendered inactive since it cannot redissolve in the white tin phase as the temperature is raised. In contrast, rejected mercury, being very mobile even at -30° C, can readily recombine as the temperature rises above -8.15° C to form a white tin solid solution and so displace the transition temperature considerably.

ACKNOWLEDGMENT

Grateful acknowledgment is made to the National Research Council of Canada for financial assistance throughout the course of this work.

REFERENCES

- EWALD, A. W. 1954. *J. Appl. Phys.* **22**, 11, 1436.
EWALD, A. W. and TUFTE, O. N. 1958. *J. Appl. Phys.* **29**, 7, 1007.
——— 1959. *J. Phys. Chem. Solids*, **8**, 523.
GROEN, L. J. 1954. *Nature*, **174**, 836.
GROEN, L. J. and BURGERS, W. G. 1954. *Proc. Koninkl. Akad. Wetenschap. Amsterdam, B*, **57**, 79.
HALL, E. O. 1955. The mechanism of phase transformations in metals, Symposium November, 1955 (Monograph, 1956, Inst. of Metals).
HANSEN, M. 1936. *Aufbau der Zweistofflegierungen* (Julius Springer, Berlin), p. 809.
LEE, J. A. and RAYNOR, G. V. 1954. *Proc. Phys. Soc. B*, **67**, 737.
RAYNOR, G. V. and SMITH, R. W. 1958. *Proc. Roy. Soc. A*, **244**, 101.
SMITH, R. W. The transition temperature of the transition between the grey and white allotropes of zone-refined tin and its dilute alloys (to be published).
SMITH, R. W. and RAYNOR, G. V. 1957. *Proc. Phys. Soc. B*, **70**, 1135.
THEWLIS, J. and DAVEY, A. R. 1954. *Nature*, **174**, 1011.
TIN RESEARCH INSTITUTE. 1949. Equilibrium data for tin alloys.

HEAVY-LIQUID BUBBLE CHAMBERS¹

ROBERT W. WILLIAMS²

ABSTRACT

Experience with some high-Z liquids or fluid mixtures in bubble chambers, at M.I.T. and from other groups, is discussed. Measurement procedures are analyzed, and optimum methods are presented for angle measurements, $p\beta c$ determination from multiple scattering, and momentum determination from magnetic curvature. Magnetic fields will be useful even in strongly scattering liquids. Combined use of magnetic and scattering determination is not much better than one alone. Results are presented on detection efficiency for high-energy gamma rays, and on the severe effects of radiation straggling on energy measurements on electron pairs.

INTRODUCTION

The bubble chamber was invented only 6 years ago (Glaser 1953) but it is at present the principal tool of high-energy physics. Propane or liquid hydrogen has been used in most experiments to date, but the possibility of using liquids of high atomic number, and therefore good gamma-ray detection properties, was early emphasized by Glaser, who has constructed a xenon chamber (Brown, Glaser, and Perl 1956). Other liquids have been investigated by the Massachusetts Institute of Technology (M.I.T.) group (Pless and Williams 1957; Yamamoto 1957; Jones 1958), the Cal Tech group (Alyea *et al.* 1957; Bugg 1958), and several European groups (Argan *et al.* 1958; Bertanza *et al.* 1958; Bullock *et al.* 1958). The primary objective is a short mean free path for gamma-ray materialization. At least two experiments on the neutral decay modes of strange particles have already been undertaken with heavy-liquid chambers, and more are expected. Figure 1 is a photograph from a run started by the Cambridge bubble chamber group (M.I.T., Harvard, Brandeis, and Brown Universities) using a propane-methyl iodide chamber at the Brookhaven cosmotron; three electron-positron pairs and a small electron shower are visible.³

The present paper examines the properties of some practical high-Z liquids, and analyzes some of the measurements which can be made in such a chamber. The high density of the liquid greatly reduces the precision of momentum determination by magnetic curvature, without affording multiple-scattering measurements comparable with those in nuclear emulsion. However, the greater stopping power leads to more frequent range determinations, and the shortened mean free path for nuclear interactions is important in some experiments.

¹Manuscript received June 5, 1959.

Contribution from Department of Mathematics, McGill University, Montreal, Que.

²On leave from Massachusetts Institute of Technology, Cambridge, Massachusetts. Present address: Department of Physics, University of Washington, Seattle, Washington.

³This experiment will be resumed when the cosmotron is again operating. A xenon exposure made at Berkeley by the Michigan group is presently being analyzed.

CHARACTERISTICS OF HEAVY-LIQUID CHAMBERS

Nearly any liquid which is stable at temperatures approaching its critical temperature would function as a bubble-chamber liquid; problems of temperature and pressure, corrosiveness, expense, and toxicity limit the choice. The theory of bubble-chamber operation (Pless and Plano 1956; Seitz 1958) indicates that surface tension is the controlling property: if vapor pressure at operating conditions is not to be too high, the surface tension should be low. The surface tension of a high- Z liquid can be lowered by admixture of a lighter liquid, or even a dissolved gas. The properties of mixed-fluid chambers are not strikingly different from those of pure-liquid chambers; they were first investigated by Argan and Gigli (1956); the application to high- Z chambers was made by Pless and Yamamoto (Yamamoto 1957; Pless and Williams 1957), who showed that propane and methyl iodide yield a convenient mixture.

Table I gives some characteristics of high- Z bubble-chamber liquids which have been tested by various groups. Xenon and WF_6 present special difficulties of procurement or handling; the other compounds are articles of commerce.

TABLE I
Properties of some bubble-chamber liquids

	Xe	WF_6	$\text{CH}_3\text{I}-\text{CF}_3\text{Br}$	CF_3Br	$\text{C}_3\text{H}_8-\text{CH}_3\text{I}$	$\text{C}_3\text{H}_8-\text{CH}_2\text{I}$	C_3H_8
Volume fraction	1	1	.6-.4	1	.5-.5	.78-.22	1
Weight fraction	1	1	.69-.31	1	.18-.82	.4-.6	1
Operating density, g cm^{-3}	2.3	2.4	1.79	1.57	1.14	0.78	0.44
Radiation length, X_0 , g cm^{-2}	8.6	9.1	10.7	16.5	10.8	13.7	46.5
Radiation length, l_0 , cm	3.7	3.8	6	10.5	9.5	17.6	105
100-Mev gamma mean free path, cm	6.2	6.3	10	19	17	31	216
Density of H, g cm^{-3}	0	0	.026	0	.057	.067	.080
Fraction of A. P. events on H	0	0	.06	0	0.19	0.27	0.4

The characteristic length for radiative energy loss by an extreme relativistic particle is the radiation length (defined, for example, by Rossi 1952); it is also the natural unit for related processes such as pair production and Coulomb scattering. We list the radiation length (including Born approximation and atomic-electron corrections) for the various liquids, and also the effective mean free path for pair production of 100-Mev gamma rays. The latter includes the pairs created in the field of atomic electrons (one of the three electrons is usually very low energy compared with the other two), but excludes any pairs for which one electron has too low an energy (<4 Mev) to make a recognizable pair. We found the discussion of Ashkin and Bethe (1953) convenient for pair-production cross sections.

The presence of hydrogen in the mixture proves to be very desirable, despite the fact that one cannot make good production cross-section measurements. One finds that some of the events (for example, associated production of a Λ and K^0 particle in certain angular ranges) have overdetermined kinematics so that they can be definitely identified as H events, and can therefore

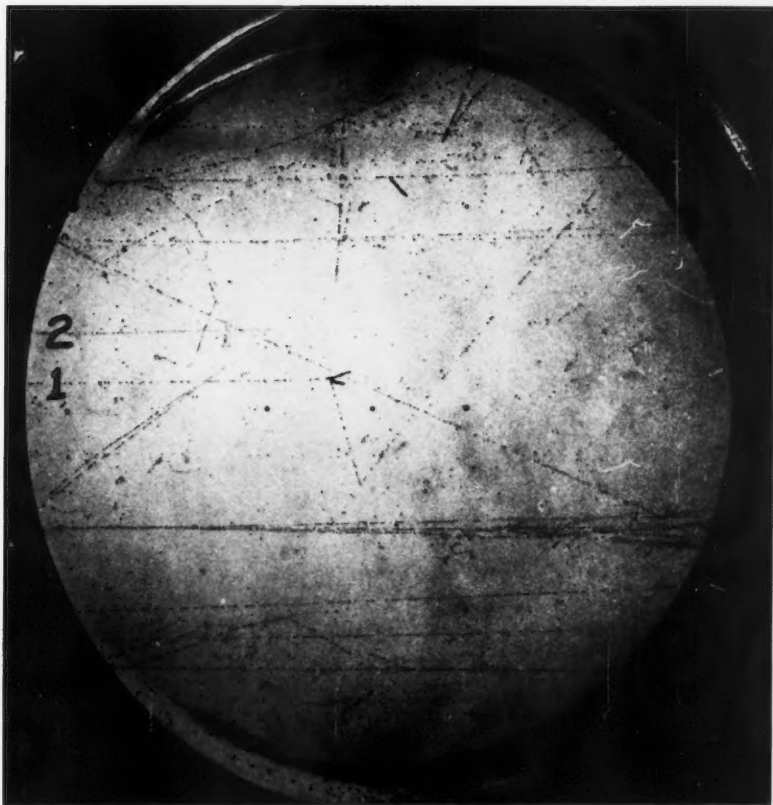


FIG. 1. Negative pions of 900-Mev incident from the left on a methyl iodide - propane mixture. Two gamma rays from the end of track 1 and one from track 2 create pairs in the chamber. A small electron shower is also visible.



be used to determine beam energy and measurement accuracy. A thorough discussion of the separation of hydrogen events from carbon events in propane will be found in the work of the Columbia group (Eisler *et al.* 1958). We have used their results on the reaction $\pi^- + p \rightarrow \Lambda + K^0$ to estimate the number of such associated-production events in heavy liquids, and the fraction occurring on free protons, as follows: Eisler *et al.* find the cross section for associated production on carbon to be four times that on a free proton: $\sigma_{AP}(C) = 4\sigma_{AP}(H)$ at a π^- energy about 1 Bev. For heavier nuclei we assume that associated production occurs in the same ratio to carbon as the measured inelastic cross sections for high-energy pions (Cronin *et al.* 1957), that is, that the *fraction* of inelastic events yielding strange particles when pions strike complex nuclei is independent of A . This would not be true of a proton beam, but is probably a fair approximation for pions. Table I gives the fraction of associated-production events occurring on free H, for the various liquids.

MEASUREMENT ACCURACY

The mechanism of bubble formation in a bubble chamber is very probably associated with delta rays of low energy (order of 1 kev), most of which have a range considerably less than 1 micron. The bubbles grow much too rapidly to undergo noticeable diffusion, so that, in the absence of turbulence or statistical asymmetry in bubble growth, the center of a bubble should correspond to the path of the particle which seeded it to better than 1 micron. The accuracy of track location, as Glaser has pointed out (Brown *et al.* 1956), may in principle be comparable with that of a photographic plate rather than that of a cloud chamber, although the number of locations per centimeter is only 20 to 50, as in a cloud chamber. In practice one is forced to drastic compromises in the optics of bubble-track recording: the bubbles must grow to perhaps 100 microns in order to be visible, and a small numerical aperture must be used to have manageable photography and a reasonable depth of field. The result is that the standard error in the location of one point on a track may be of the order of 0.005 to 0.01 cm. The accuracy is most critical in the application of multiple scattering to momentum determinations; in a multiple-scattering experiment with a small chamber and good optics Kirillov *et al.* (1958) seem to have had a standard error (estimated from equation (1) below) of only 0.002 to 0.003 cm.

A. Angle Determinations

Most of the relevant measurements (kinematic reconstruction, momentum determination from magnetic curvature, $p\beta c$ from multiple scattering) depend on determining the angle of a portion of the track. The problem, in one plane, is the least-squares fit of a straight line of length d to a number of measurements, b , per centimeter, each of which has an r.m.s. error ϵ_b . (We use ϵ throughout for absolute errors, r for relative errors.) This gives an angle error

$$(1) \quad \epsilon_\theta = \epsilon_b d^{-3/2} (12/b)^{1/2} \text{ radians.}$$

b can be no greater than the bubble density, of course, and in practice will

often be less. ϵ_z , the error in the direction perpendicular to the photographic plane, and its corresponding dip-angle error, will be greater by a geometrical factor depending on the stereo system. For two cameras separated by distance D , at objective distance u , the factor, assuming independence of the errors ϵ_y in bubble location in the two images, is $\sqrt{2}u/D$. If the largest usable angle at the lens is θ_m , one often has $\tan \theta_m \sim D/u$, so that the factor is typically about 5 ($\theta_m \sim 15^\circ$).

The optimum measurement length d_0 , in the absence of distortions, will be determined by minimizing the measurement error, above, combined with the error due to multiple scattering. It is convenient to express multiple-scattering angles in terms of the formula

$$(2) \quad \theta = (E_s/p\beta c)(d/l_0)^{1/2},$$

where d is the track length l_0 the radiation length, $p\beta c$ the momentum-velocity product in Mev, and E_s a "constant" which varies slowly with β , d , and with the Z of the material, and of course depends numerically on what angle one is measuring. (We assume singly charged particles.)

Table II gives values of E_{pm} for the mean projected angle between true tangents at the ends of the track. We want instead the projected r.m.s. angle

TABLE II

Projected mean Coulomb scattering angle in radians between tangents to a track of length d , in material of radiation length l_0 and atomic number Z , for particle velocity β . Table gives δ in the formula

$$\theta_{pm} = \frac{12 \text{ Mev}}{p\beta c} \left(\frac{d}{l_0} \right)^{1/2} (1 + \delta)$$

$Z \backslash d/l_0$	10^{-2}	10^{-1}	1	10	
6	-0.12	-0.05	+0.01	+0.07	$\beta = 0.3$
29	-0.11	-0.03	+0.05	+0.12	
82	-0.17	-0.07	+0.08	+0.09	
6	-0.18	-0.10	+0.03	+0.03	$\beta = 0.7$
29	-0.15	-0.06	+0.02	+0.09	
82	-0.17	-0.08	-0.01	+0.09	
6	-0.20	-0.12	-0.05	-0.01	$\beta = 1$
29	-0.23	-0.13	-0.05	-0.03	
82	-0.19	-0.09	-0.00	-0.08	

corresponding to the least-squares fit of a straight line to the track. Scott (1952) gives, for Gaussian statistics, the factors $\sqrt{\pi/2\sqrt{26/35}} = .765$; from Table II we find $E_{pm} \sim 10$ as a typical value for short fast tracks in heavy liquid; so for our analysis we can assume $E_{rms} = .765 E_{pm} \sim 8$, and the multiple-scattering error $\epsilon_{MSS} = (8/p\beta c)(d/l_0)^{1/2}$. Minimizing the sum of the squares of the errors yields

$$(3) \quad d_{opt} = (0.75 p\beta c \epsilon_y \sqrt{l_0/b})^{1/2};$$

the corresponding minimum angle error is

$$(4) \quad \epsilon_{\theta 0} = 8.6 \epsilon_y^{1/4} (p\beta c)^{-3/4} b^{-1/8} l_0^{-3/8},$$

where the units are centimeters, million electron volts, and radians.

It is noteworthy that the dependence of the error on l_0 is not strong, so that the heavy-liquid chambers will be only a factor of two or three worse than propane chambers in this respect. The Columbia group (Eisler *et al.* 1958) reports average angle errors of about .004 radian in propane (which implies, for $p\beta c \sim 400$ Mev, a location error $\epsilon_y \sim .01$ cm). When a magnetic field is present there will be a correction to the apparent direction; this is discussed in Section C.

B. Multiple Scattering

The possibility of using multiple-scattering measurements to determine the $(p\beta c)$ of bubble-chamber tracks, following the well-known techniques of nuclear emulsions, has been explored in several laboratories; Teem and co-workers (Alyea 1957) have discussed results from a very small WF_6 chamber, while Kirillov and co-workers (1958) report on measurements in propane. The crucial point here is the measurement accuracy, since for an arbitrarily good accuracy one can obtain an estimate of $(p\beta c)$ limited only by the total number of bubbles. It is convenient to consider first the theoretical expression for mean-scattering angle, then the actual measurement, and to defer to the next section discussion of the problem when a magnetic field is present.

Multiple scattering is discussed in detail by Scott (1952); the most convenient statistic is the mean absolute projected angle (the actual track is projected onto a plane containing the initial direction of the particle, and the angle θ_p between the initial direction and the projection of the final direction is considered). Within the restrictions of a small-angle approximation the full distribution (not a Gaussian approximation) is derived, and the mean angle is calculated under the assumption that any single scattering more than four times the average scattering for the whole track will be rejected—Scott calls this the cutoff case. For very high momenta and long tracks the finite size of the nucleus causes a decrease in scattering not calculated by Scott. Cooper and Rainwater (1955) have given numerical results for the scattering distribution including nuclear-size effects, but bubble-chamber scattering measurements will not ordinarily extend to such high-momentum, long-track cases. Rejection of large-angle scatterings (the cutoff procedure described below) greatly reduces the error caused by inaccurate treatment of the tail of the distribution.

Scott's numerical results (or, equivalently, those of Moliere which agree very closely) for the projected mean angular deflection, θ_{pm} , of a particle traversing a distance d , are presented as a table of values of E_s (equation (2)) in Table II, which has been taken from the larger table of Barkas and Rosenfeld (1958). These values are for the non-cutoff case.

To estimate $(p\beta c)$ from multiple-scattering measurements one would like the true direction at every point along the track. One has available the positions of certain points, within a certain error (the "noise", assumed Gaussian with standard deviation ϵ_y) and one must integrate out the noise (and subtract out what is not integrated out) to obtain the average changes in direction, from second differences or some comparable operation. The

following method, which must be fairly close to optimum, is frequently used in nuclear emulsion work⁴ and will serve for analysis.

One divides the track of length l into $n+1$ equal segments, and makes a least-squares fit of a straight line to each track segment. The n angles α_i between adjacent lines then give the observed mean scattering $\alpha'_{\text{obs}} = 1/n \sum |\alpha_i|$. Any angle α_j which is more than four times the mean angle α'_{obs} is then excluded from the data and the "cutoff" mean, α_{obs} , is computed. The remaining contribution of "noise" scattering will include the error given in equation (1); it may also include appreciable contribution from the measuring engine and from turbulence. The mean noise scattering, ϵ_n , for a given cell length $l/(n+1)$, can be determined from measurements on high-momenta "straight" tracks.⁵ The best estimate for the true mean angle of scattering will be

$$(5) \quad \alpha_{\text{sc}} = (\alpha_{\text{obs}}^2 - \epsilon_n^2)^{1/2}.$$

Table II gives the mean change in direction of a path of length d ; α_{sc} , however, is the (cutoff) mean change in direction between two best-fit lines, each of length d . Scott presents results for a related case, the cutoff mean angle between two chords (Scott 1952, equation (8f); note that his t is $2d$) and states that the effect of a least-squares fit can be included by multiplying his results for α by $\sqrt{39/35} = 1.05$. In terms of Scott's function $C_{m;co}$ the scattering constant, in a medium of radiation length $X_0 \text{ g cm}^{-2}$, for α_{sc} becomes

$$(6) \quad E_\alpha = 0.59Z(X_0 C_{m;co}/A)^{1/2}$$

and the multiple-scattering estimate of $(p\beta c)$ is

$$(7) \quad p\beta c = \frac{E_\alpha}{\alpha_{\text{sc}}} \left[\frac{l}{(n+1)l_0} \right]^{1/2}.$$

To compare with Table II we compute a representative E_α for bubble-chamber measurements: $Z = 29$, $\beta \approx 1$, $d/l_0 = 0.1$. This gives $E_\alpha = 8.44 \text{ Mev}$, while from Table II, $E_{\text{pm}} = 10.4 \text{ Mev}$.

To find an optimum value of n —that is, an appropriate noise-integrating length—we use equation (1) for a single segment r.m.s. angle to get a mean difference noise angle given by

$$(8) \quad \epsilon_n = \left[\frac{48}{\pi} \frac{(n+1)^3}{bl^3} \right]^{1/2} \epsilon_p.$$

Since the relative error in α_{obs} is proportional to $1/\sqrt{n}$, an optimum n , say n_0 , must exist which minimizes the relative error in α_{sc} , and therefore in $(p\beta c)$. The nature of the noise distribution and the accuracy with which ϵ_n is known will influence one's choice of the best ratio $\epsilon_n/\alpha_{\text{sc}}$; for photoplate

⁴In nuclear emulsion work, however, chord-fitting may be done by eye. Bubble-chamber tracks are usually measured on a semiautomatic co-ordinate recorder and the line segments would be fitted by a computer.

⁵Moyal (1950) gives a method for subtracting the noise by using the internal statistics of the track; essentially, $1/n \sum \alpha_i \alpha_{i+1}$ differs from zero only because of correlations introduced by noise. The method of the text should be superior if a good estimate of ϵ_n is available.

work the problem is discussed by Dilworth *et al.* (1950) and by Voyvodic (1954). If we assume that ϵ_n is accurately known and its fluctuations are Gaussian, then from (5), (7), and (8) we can find the optimum ratio by statistical analysis; it proves to be $\epsilon_n/\alpha_{se} = 1/\sqrt{7} = 0.38$. Conservative practice would suggest a greater cell length, to lessen the contribution of ϵ_n , but for bubble-chamber accuracy this should serve well enough. From (7) and (8), taking E_α to be 8.5 Mev we have

$$(9) \quad n_0 = \left(\frac{l^4 b}{l_0 \epsilon_y^2} \right)^{\frac{1}{2}} \left(\frac{0.8 \text{ Mev}}{p\beta c} \right)^{\frac{1}{2}},$$

which is essentially the same as (3). Even a crude guess for $(p\beta c)$ will serve to estimate n_0 .

The relative standard deviation in the mean-scattering angle can be estimated from the statistical discussion of Scott (1952), who finds about $.85/\sqrt{n}$ if there is no noise; with our noise ratio this is increased by $(1+1/7)$ to give

$$(10) \quad r = \frac{0.97}{\sqrt{n_0}}.$$

This is also the relative error in $(p\beta c)^{-1}$, or in $(p\beta c)$, if r is small enough. However, the distribution function of α_{se} is not Gaussian, and in any case its inverse, for typical values of r , will be decidedly asymmetric. As a fairly optimistic example consider a track 20 cm long with $p\beta c = 300$ Mev, $\epsilon_y = 0.005$ cm, $b = 10 \text{ cm}^{-1}$, $l_0 = 10$ cm. Then $n_0 = 18$, $r = 0.23$. Apart from an increase in track length it appears difficult to visualize dramatic improvements in r , because of the insensitivity of (9); a decrease in $l_0 \epsilon_y^2$ by a factor of 10 would only decrease r by a factor of 1.33.

In practice corrections must be made for the dip of the track (since it is usually more accurate and convenient to project onto a plane parallel to the film plane rather than a plane containing the beginning of the track), and for energy loss along the track. Although scattering increases as the particle loses energy, very little improvement in statistical accuracy is obtained by progressive shortening of the cell length. To make an energy-loss correction one must either estimate β or assign a mass to the particle. Using the approximation (Annis *et al.* 1953) $p\beta c = \text{const. } R^{0.55}$, one finds in first approximation that the estimate of equation (7) should be raised by $(1+0.28 l/R_0)$ to give the $p\beta c$ at the beginning of the track. (R_0 is the range corresponding to the initial energy.)

Subtraction of magnetic curvature is considered in Section C. Experimental tests of the multiple-scattering theory in nuclear emulsion, and further references, can be found in the paper of Rosendorff and Eisenberg (1958).

A case of particular interest is the identification of a particle which stops in the chamber, by estimating its mass from multiple scattering. The problem has been solved by Olbert and collaborators (Annis 1953), who give the distribution function for a variable related to the scattering angles and residual range, measured at n points along the track. For a single track of reasonable (20–30 cm) length the separation between pions and protons, for

example, is not very good: the small-scattering part of the pion distribution (it is a chi-squared curve with n degrees of freedom) overlaps the proton distribution considerably, so that tracks with little scattering are ambiguous. Widely scattered tracks, however, can be identified as pions with good confidence. The appropriate cell length $[l/(n+1)]$ can be estimated by applying equation (3) to the beginning of the track; little is gained by decreasing the cell length toward the end of the track. The "error" in mass (half-width at $1/\sqrt{e}$ point) is about $\Delta m/m = 1.6/\sqrt{n}$. One sees from equation (3) that the high Z of the liquid is not of great advantage in multiple-scattering measurements, since the standard deviation varies only as $l_0^{1/8}$.

A homogeneous group of stopping particles can lead to a fairly good estimate of their mass by the Olbert method; results for a propane chamber are given by Kirillov *et al.* (1958).

C. Magnetic Curvature

A magnetic field of modest magnitude (15–20 kilogauss, say) can lead to useful momentum measurements in a chamber of even quite short radiation length l_0 ; and of course one can visualize much larger fields with pulsed magnets. The general problem of extracting the maximum information from combined magnetic and multiple-scattering measurements has been considered by a number of authors: the most explicit and useful result is the work of Kim (1958). However, the results are disappointing in the sense that one finds little improvement over the usual practice of choosing only the better of the two estimates.

Kim proves the validity of making the individual magnetic and multiple-scattering estimates of $(pc)^{-1}$, and taking the weighted average. This leads to an improvement in the error, r , by a factor which is always less than $\sqrt{2}$. In a numerical example in which each estimate separately has a minimum error of 10%, Kim finds that the combined error is 8%.

We shall therefore confine this discussion to the individual estimates.

1. Correction to Multiple Scattering

The magnetic field causes a non-zero mean angular deflection which must be estimated by finding the net angular deflection

$$\alpha_T = \sum_{i=1}^n \alpha_i;$$

the scattering angle is then

$$\alpha_{\text{obs}} = \frac{1}{n} \left(\sum_i |\alpha_i| - \alpha_T \right),$$

and all goes through as before.

2. Magnetic Estimate of Momentum

The momentum component of a particle, p_t , transverse to a uniform magnetic field B is related to the angle θ_{mag} through which its projected path would turn in the absence of scattering by

$$(11) \quad (p_t c)^{-1} = \theta_{\text{mag}} / (3 \times 10^{-4} B l_t)$$

where pc is in Mev, B in gauss, and the length of projected path l_t in centimeters. It is well known that the best estimate for track curvature, in the presence of a fixed amount of multiple scattering and noise, is obtained from α_T , the observed net deflection of the track (see, for example, Scott 1949; or Moyal 1950). Random scattering, in other words, automatically averages itself out in the most efficient way and no amount of inspection of the shape of the curve can improve on this. One normally estimates $(p_t c)^{-1}$ by substituting α_T for θ_{mag} in (11), with a standard deviation given by the root-mean-square multiple-scattering angle, θ_{rms} , estimated (using Gaussian statistics) from (2) or from $\sqrt{(\pi/2)n\alpha_{sc}}$. However, Kim (1958) shows that the maximum-likelihood estimate of θ_{mag} is smaller than α_T when scattering is prominent; he gives a graphical solution but for practical cases his approximate relation is adequate:

$$(12) \quad (\theta_{mag})_{est} \approx \alpha_T \left[1 - \left(\frac{\theta_{rms}}{\theta_{mag}} \right)^2 \right] = \alpha_T (1 - r_m^2),$$

where the relative standard error in the magnetic estimate, r_m , is given from (2) with $E_{rms} = 14$ Mev, and (11), by

$$(13) \quad r_m = \frac{4.7 \times 10^4}{\beta B \cos \phi \sqrt{l l_0}}.$$

Here B is in gauss, l is the true track length in centimeters, and ϕ is the dip angle. Exclusion of large single scatterings will reduce r_m by 10 or 15%.

The correct estimate for the initial direction of a track must include the effect of the mean curvature of the track, $C = \theta_{mag}/l_t$; this applies to the direction measurements of Section A as well as to the estimation of the total angle α_T . A least-squares fit of a parabola of *known* curvature C to a segment of track of length d shows that the slope given by the straight-line least-squares formula must be corrected by $1 \pm (1/2)Cd$. The corrected estimate for the total angle is therefore

$$(14) \quad \alpha_{corr} = \alpha_T \left(1 + \frac{d}{l_t} \right)$$

and this should be used in (12), iterated if necessary.

The ratio of magnetic to multiple-scattering error can be used to indicate which method is preferable; for non-dipping tracks it is

$$(15) \quad \frac{r_m}{r_\alpha} = \frac{10^4}{B \beta^{5/4}} \left(\frac{440 \text{ Mev}}{pc} \right)^{1/2} \left(\frac{b}{l_0 \epsilon_\nu} \right)^{1/8}$$

in the usual units, and is independent of track length. With $\epsilon_\nu = 0.005$ cm, $b = 20$ cm⁻¹, $l_0 = 10$ cm, and $B = 20,000$ gauss, this would be $r_m/r_\alpha = (0.65/\beta^{5/4})(440/pc)^{1/4}$, and our previously cited example ($p\beta c = 300$ Mev, $l = 20$ cm) will have an error of 18%, if it is a meson.

Under our assumptions of no turbulence and excellent optics the uncertainty of a magnetic determination will usually have a contribution from measurement errors which is less than half of the error due to scattering, r_m .

From (4) and (13) the ratio may be written

$$(16) \quad \frac{r_{\text{meas}}}{r_m} = \frac{1}{l^{\frac{1}{3}}} \left(\frac{p\beta c}{1.8 \text{ Mev}} \right)^{\frac{1}{3}} \left(\frac{l_0 \epsilon_y^2}{b} \right)^{1/8}.$$

Energy loss along the track will often be an important correction. If one assumes a power law relation between momentum and range, and assigns a mass, one can find the initial momentum from the observed total angle; in first approximation (11) gives the momentum at the center of the track, and (13) is correct if β refers to the center of the track.

The latter part of a track which is near the end of its range does not add much information to a momentum determination. A practical cutoff point can be obtained from equation (3) by requiring that the fractional energy change in distance d not exceed some reasonable value.

3. Sign of the Charge

When r_m is large one can still ask if the sense of the net deflection gives a reliable indication of the particle's charge; this problem was solved by Moyal (1950). Both the total deflection α_T and mean-scattering angle α_{sc} must be measured, and an estimate of $|\theta_{\text{mag}}|$ must somehow be made, independently of α_T (one might estimate $p\beta c$ from α_{sc} , and guess at β from bubble density, or a mass assignment, or one might have limits on $|\theta_{\text{mag}}|$ from external considerations). Then the confidence level of the sign indicated by α_T (that is, the fraction of such observations which would give the right answer if there were equal a priori probability for either sign) is

$$P = \left\{ 1 + \exp \left[- \frac{4|\alpha_T \theta_{\text{mag}}|}{\pi \alpha_{sc}^2 (n+1)} \right] \right\}^{-1}.$$

D. Measurements on Electrons

To obtain information on high-energy gamma rays one must look at electron pairs; the opening angle is too loosely correlated with gamma-ray energy, and usually too small, to be of much use, so one has to estimate the electron energies. The accuracy of this measurement, in a high- Z liquid, is severely limited by the uncontrollable effects of radiation straggling. The large fluctuations of energy loss by radiation are a familiar phenomenon in electron measurements; to illustrate we point out that a high-energy electron traversing one-half a radiation length will suffer an *average* energy loss of one-half, but a most probable loss of zero; the straggling function rises monotonically to infinity at zero energy loss.

There are two types of measurements we might consider. The first is the determination of a parameter of a known distribution from observations on the energies of a sample of electrons. The procedure is straightforward: one "folds" the distribution with the appropriate radiation straggling function, and determines the parameter from the folded distribution by maximum-likelihood or equivalent methods. This method has had a number of applications; it is described, for example, by Vilain and Williams (1954) with reference to the electron spectrum from muon decay, and was applied to a

bubble-chamber measurement by Pless *et al.* (1957); we shall not discuss it further. The second, and usually more pertinent, problem is the estimation of the energy of an individual electron, which we discuss in this section.

The probability, $\pi(E_0, E, t)dE$, that an electron of energy E_0 have an energy E in dE after $t = l/l_0$ radiation lengths has been given by Eyges (1949) in various approximations, of which the one appropriate to an energy region $\sim 10^8$ ev is the Bethe-Heitler straggling formula

$$(17) \quad \pi(E_0, E, t)dE = \frac{1}{(\frac{3}{4}t-1)!E_0} [\ln(E_0/E)]^{(\frac{4}{3})t-1} dE;$$

we are neglecting collision loss. What we want is an inverse problem: given an observed energy E_{obs} (from magnetic curvature, say), with what confidence can we say that this electron's original energy E_0 lay within some specified range; that is, what fraction out of all electrons that give E_{obs} in dE_{obs} would come from that range if the experiment were repeated indefinitely? Evidently this may depend on the distribution-in- E_0 , say $H(E_0)dE_0$, of all possible electrons which might be observed in the experiment. The usual situation is that distribution functions for errors, collision loss, etc., are so well behaved that the answer to our question is essentially independent of the form of the a priori distribution $H(E_0)$. We shall show that this is *not* the case for radiation straggling, taking the physically "most reasonable" form for $H(E_0)$, the uniform distribution per logarithmic energy interval,

$$(18) \quad H(E_0)dE_0 = K dE_0/E_0.$$

If we could measure the energy E of the electron after a path length t we could use, as our inverse problem, the fraction of all electrons of energy E in dE which come from the range E to $E+\Delta E$, which is clearly

$$f = \int_E^{E+\Delta E} \pi(E_0, E, t)H(E_0)dE_0 / \int_E^{\infty} \pi(E_0, E, t)H(E_0)dE_0.$$

However, we must use the entire path for our measurement, and from the total track deflection, which is the integral of the reciprocal of the energy, we obtain the observed energy E_{obs} . To make progress we assume that the entire energy loss ΔE occurs at the midpoint of the track,⁶ whence

$$(19) \quad 2/E_{\text{obs}} = 1/E_0 + 1/E.$$

Now we can calculate the fraction of all electrons of energy E_{obs} which come from the range E_{obs} to $E_{\text{obs}}+\delta E$; it is

$$(20) \quad F = \int_{E_{\text{obs}}}^{E_{\text{obs}}+\delta E} \pi(E_0, E, t) \frac{\partial E}{\partial E_{\text{obs}}} H(E_0)dE_0 / \int_{E_{\text{obs}}}^{\infty} (\text{same}),$$

where E must be eliminated by (19). Using (17), (18), and (19), we can express F in terms of the incomplete gamma function, tabulated by Pearson (1922). In Pearson's notation it is

⁶One can see that a more accurate treatment would give the same results to the lowest order in $\Delta E/E$.

$$(21) \quad F(r, t) = I\left(\frac{\ln(1+2r)}{\sqrt{4/3}t}, \frac{4}{3}t-1\right),$$

where we have put $\delta E/E_{\text{obs}} = r$. This is not even approximately Gaussian; however, we may identify as a "standard deviation" the value of r which makes $F = 0.68$, say r_{68} . That is, there is a 68% chance that E_0 lay within $r_{68}E_{\text{obs}}$ of E_{obs} , which is the confidence level of one standard deviation in the Gaussian case.

In Fig. 2 we plot r_{68} as a function of t . We also plot r_{95} , the value which gives the confidence level 95%, which would be two standard deviations in

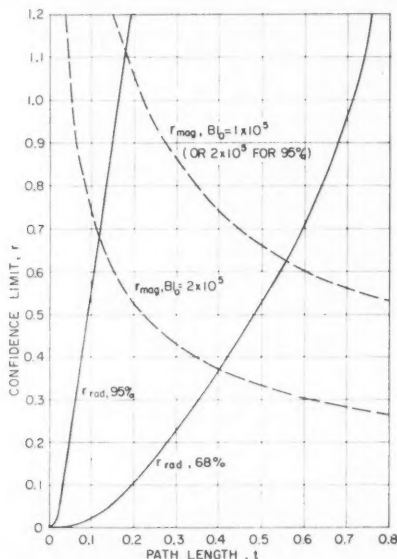


FIG. 2. Radiation straggling effect. The confidence limit $r_{\text{rad}} = \delta E/E_{\text{obs}}$ is plotted against path length in radiation lengths, t , for 68% and 95% confidence level. Dashed lines show the standard deviation in magnetic curvature measurement for two values of Bl_0 .

the Gaussian case; of course it is in this case much greater than $2r_{68}$. To pick the path length t_0 which would give the optimum estimate of E_0 we must compare r_{68} with the error in magnetic curvature r_m from (13). Figure 2 gives r_m for two values of $Bl_0 \cos \phi$: $Bl_0 \cos \phi = 1 \times 10^5$ gauss cm and 2×10^5 gauss cm. Minimizing the combined error $r_{\text{comb}}^2 = r_{68}^2 + r_m^2$, we find

$$\begin{aligned} Bl_0 \cos \phi = 1 \times 10^5, \quad t_0 = 0.4, \quad r_{\text{comb}} = 0.83, \\ Bl_0 \cos \phi = 2 \times 10^5, \quad t_0 = 0.3, \quad r_{\text{comb}} = 0.48. \end{aligned}$$

Large as they are, these errors are deceptive because they contain a contribution (though less than half) from the radiation fluctuation. If we ask for the 95% confidence limit, with the better case ($Bl_0 \cos \phi = 2 \times 10^5$), we find

a different and much shorter optimum, $t_0 \sim 0.14$, and $(r_{\text{comb}})_{95} = 1.5$. A measurement by multiple-scattering methods presumably would give the same result.

To show the degree to which the entire calculation is dependent on the form of the a priori distribution $H(E_0)$ we have calculated r_{68} for a cutoff distribution: $H(E_0) = 0$ for $E_0 > 5E_{\text{obs}}$. At $t = 0.3$, this lowers r_{68} by 13% of the value given in Fig. 2, i.e., $0.23 \rightarrow 0.20$.

The above errors will of course be multiplied by a factor $\leq \sqrt{2}$ for a gamma-ray energy (two electrons), and a factor which can be as large as 2 for a π^0 energy (four electrons). It is clear that a compromise on l_0 would be necessary if one wanted to measure gamma-ray energies to better than 50%. In the next section the effect of l_0 on gamma detection efficiency is considered.

E. Gamma-Ray Detection Efficiency

The strongest demand for a short radiation length (high average Z) is set by gamma-ray materialization probabilities. Table I gives the effective pair-production mean free path for 100-Mev gamma rays, λ ; it is about $1.8l_0$ (for 400 Mev it would be about $1.5l_0$). We here present a rough calculation of the efficiency of some typical observations, assuming a constant value for λ .

We assume a spherical observation volume, radius R , with the gamma-ray source distributed uniformly throughout it, and an isotropic, non-correlated space distribution for the gamma rays. (The latter is partly realized by K mesons and hyperons of reasonable energy which decay via neutral pions, for example.) Let $P_1(r)$ be the average probability of detecting one gamma ray which originates at r . We want \bar{P}_1 , the average of $P_1(r)$ over the sphere. To avoid the unpleasant integral we will approximate $P_1(r)$ by an algebraic expression which has the correct value and slope at $r = 0$ and $r = R$, and which approaches the correct limit (unity) in a plausible way as R/λ approaches infinity. It turns out that P at the edge of the sphere can easily be calculated and is

$$(22) \quad P_e = P_1(R) = \frac{1}{2} - \frac{\lambda}{4R} [1 - \exp(-2R/\lambda)];$$

the slope at $r = R$ can be shown to be infinite. The value of $P_1(r)$ at the center is of course

$$(23) \quad P_c = P_1(0) = 1 - \exp(-R/\lambda),$$

with zero slope at that point. The basic approximation consists of representing $P(r)$ for small R/λ as a quadrant of an ellipse, then replacing the portion from $r = 0$ to $r = P_c R$ by the uniform value P_c , for arbitrary R/λ . The result of integrating this over the sphere gives the average probability to see a single gamma ray:

$$(24) \quad \bar{P}_1 = 0.6P_c + 0.4P_e + 0.4P_e^6 - 0.4P_e^5P_c.$$

If two gamma rays are emitted (as, for example, in the decay of a neutral pion) the probability to detect them both (by our independence assumption)

is $P(r)^2$, and this can be averaged over the sphere to give \bar{P}_2 , similar to (24) but more complicated. It is felt that the approximations are good to about 5%.

In Fig. 3 we have plotted \bar{P}_1 and \bar{P}_2 as functions of R/λ . A third useful quantity, $\bar{P}_{>1} = 2\bar{P}_1 - \bar{P}_2$, is also plotted; this is the probability of seeing at least one gamma from a two-gamma event. For comparison the simple central probability P_{1c} is also shown.

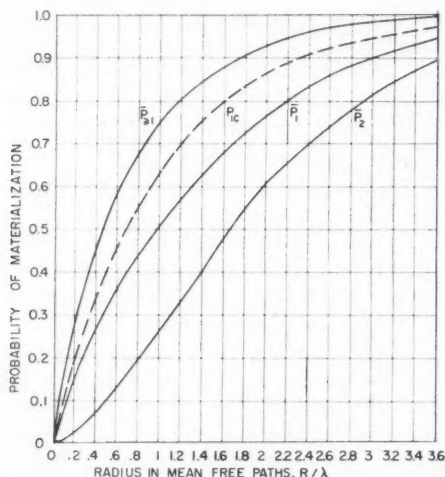


FIG. 3. Detection probability for gamma rays isotropically released throughout a spherical volume. \bar{P}_1 refers to one gamma ray, \bar{P}_2 to both gamma rays of a pair, and $\bar{P}_{>1}$ to at least one of a pair. For comparison, the dashed line gives P_{1c} , the probability at the center of the sphere.

A good detection probability—requisite for many problems in hyperon and K -meson decay—evidently demands that the radiation length should be considerably smaller than the “radius” of the chamber. In Section D we saw that this precludes accurate measurements of gamma-ray energies, unless one goes to a very large chamber or very high magnetic fields.

SUMMARY

The heavy-liquid bubble chamber can provide good ($\sim 50\%$) mean detection efficiencies for high-energy gamma rays and neutral pions over a large volume. The large mass of material has other advantages which depend on the experiment in question: charged mesons and baryons of considerable energy (typically up to ~ 100 Mev) will stop in the liquid, with consequent accurate energy determination, and observation of decay products; nuclear interaction probabilities are also relatively high. The enhanced multiple scattering should permit estimates of $(p\beta c)$ by the tedious method familiar from nuclear emulsions, but with lower accuracy than in emulsion work. A magnetic field will give momentum estimates that, within a typical range of parameters, can be either better or worse than multiple scattering; in any case they will be

easier, more reliable, and endowed with the sign of the charge. Multiple-scattering effects do not seriously interfere with geometrical (angle and position) measurements.

Measurements of electron energy present a separate problem, due to fluctuations in energy loss by radiation. A detailed consideration of this problem shows that any reasonably heavy liquid effectively prevents energy measurements to better than $\sim 50\%$ with present techniques.

ACKNOWLEDGMENTS

The author is pleased to record his indebtedness to his colleagues in the Cambridge bubble chamber group, particularly Professor I. A. Pless, for much informative discussion. The hospitality of the Mathematical Physics Group of McGill University is gratefully acknowledged.

REFERENCES

- ALYEA, E. D., GALLAGHER, L. R., MULLINS, J. H., and TEEM, J. M. 1957. *Nuovo cimento*, **6**, 1480.
- ANNIS, M., BRIDGE, H. S., and OLBERT, S. 1953. *Phys. Rev.* **89**, 1216.
- ARGAN, P. E., CONTE, M., GIGLI, A., PICASSO, E., and GONELLA, L. 1958. *Nuovo cimento*, **10**, 182.
- ARGAN, P. E. and GIGLI, A. 1956. *Nuovo cimento*, **3**, 1171.
- ASHKIN, J. and BETHE, H. A. 1953. *Experimental nuclear physics*, Vol. I, edited by E. Segre (John Wiley & Sons, Inc., New York).
- BARKAS, W. H. and ROSENFELD, A. H. 1958. Berkeley Radiation Laboratory Report UCRL-8030.
- BERTANZA, L., FRANZINI, P., MANNELLI, I., and SILVESTRINI, V. 1958. *Nuovo cimento*, **10**, 403.
- BROWN, J. L., GLASER, D. A., and PERL, M. L. 1956. *Phys. Rev.* **102**, 586.
- BUGG, D. 1958. *Rev. Sci. Instr.* **29**, 587.
- BULLOCK, F. W., DODD, C., and KALMUS, G. E. 1958. *Nuovo cimento*, **10**, 718.
- COOPER, L. N. and RAINWATER, J. 1955. *Phys. Rev.* **97**, 492.
- CRONIN, J. W., COOL, R., and ABASHIAN, A. 1957. *Phys. Rev.* **107**, 1121.
- DILWORTH, C. C., GOLDSACK, S. J., GOLDSCHMIDT-CLERMONT, Y., and LEVY, F. 1950. *Phil. Mag.* **41**, 1032.
- EISLER, F., PLANO, R., PRODELL, A., SAMIOS, N., SCHWARTZ, M., STEINBERGER, J., BASSI, P., BORELLI, V., PUPPI, G., TANAKA, H., WALOSCHEK, P., ZOBOKI, V., CONVERSI, M., FRANZINI, P., MANELLI, I., SANTANGELO, R., and SILVESTRINI, V. 1958. *Nuovo cimento*, **10**, 468.
- EYGES, L. 1949. *Phys. Rev.* **76**, 264.
- GLASER, D. A. 1953. *Phys. Rev.* **91**, 762.
- JONES, C. E. 1958. S.B. Thesis, Massachusetts Institute of Technology, Cambridge, Massachusetts.
- KIM, Y. B. 1958. *Rev. Sci. Instr.* **29**, 680.
- KIRILLOV-UGRYUMOV, V. G., KOTENKO, L. P., KUZNETSOV, E. P., and SAMOILOV, A. V. 1958. *Nuclear Instr.* **3**, 265.
- MOYAL, J. E. 1950. *Phil. Mag.* **41**, 1058.
- PEARSON, K. 1922. *Tables of the incomplete Γ -function* (Cambridge University Press).
- PLESS, I. A., BREHNER, A. E., WILLIAMS, R. W., BIZZARRI, R., HILDEBRAND, R. H., MILBURN, R. H., SHAPIRO, A. M., STRAUCH, K., STREET, J. C., and YOUNG, L. A. 1957. *Phys. Rev.* **108**, 159.
- PLESS, I. A. and PLANO, R. 1956. *Rev. Sci. Instr.* **27**, 935.
- PLESS, I. A. and WILLIAMS, R. W. 1957. M.I.T. Laboratory for Nuclear Science Annual Progress Report, May 1957, p. 104.
- ROSENDORFF, S. and EISENBERG, Y. 1958. *Nuovo cimento*, **7**, 23.
- ROSSI, B. 1952. *High-energy particles* (Prentice-Hall, Inc., New York).
- SCOTT, W. T. 1952. *Phys. Rev.* **85**, 245.
- 1949. *Phys. Rev.* **76**, 212.
- SEITZ, F. 1958. *Physics of fluids*, **1**, 2.
- VILAIN, J. H. and WILLIAMS, R. W. 1954. *Phys. Rev.* **106**, 1020.
- VOYVODIC, L. 1954. *In Progress in cosmic ray physics*, Vol. II, edited by J. G. Wilson (Interscience Publishers, Inc., New York), Chapter V.
- YAMAMOTO, R. 1957. S.B. Thesis, Massachusetts Institute of Technology, Cambridge, Massachusetts.

ULTRASONIC ATTENUATION IN SUPERCONDUCTING AND NORMAL MERCURY¹

K. L. CHOPRA AND T. S. HUTCHISON

ABSTRACT

Ultrasonic attenuation in superconducting and normal mercury has been studied with 20, 34, and 60 Mc/s longitudinal waves. The difference in attenuation between the superconducting and normal states below the transition temperature is greatly increased at the higher frequencies. The attenuation in the normal state is the same for both longitudinal and transverse critical magnetic fields and is independent of field strength between the critical value and 880 oersteds. The results disagree in some respects with those of MacKinnon and Myers. The experimental limitations of the method as a critical test of the Bardeen-Cooper-Schrieffer theory of superconductivity are discussed.

INTRODUCTION

Ultrasonic attenuation in superconducting lead, tin, indium, and aluminum (Bömmel 1954; MacKinnon 1955, 1957; Mason and Bömmel 1956; Morse, Tamarkin, and Bohm 1956; Chopra and Hutchison 1957) has been found to diminish rapidly when the temperature is lowered below the transition temperature. Recently, MacKinnon and Myers (1958) have extended this observation to the case of superconducting mercury. As mercury is readily available in a very pure state, one expects to find a marked difference of electronic absorption of ultrasound in the normal and superconducting states. These authors have observed quite different changes in attenuation with temperature in two specimens for one of which the purity is specified as 99.999%. The observations were carried out at 10 Mc/s. At this frequency a significant diffraction loss occurs in addition to the two unknown seal losses arising from the mercury to copper and copper to quartz end junctions employed. These losses are probably significantly greater than the attenuation in the superconducting mercury. We have eliminated the copper disks and one seal and have been able to work at the higher frequencies of 20, 34, and 60 Mc/s thus reducing the diffraction losses. MacKinnon and Myers have also observed an unusual increase in attenuation at the lower temperature with a transverse magnetic field. The attenuation in the normal state, as obtained by applying the critical transverse magnetic field, has been found to be much higher than that obtained by applying the critical longitudinal field. These results are unusual and need verification.

EXPERIMENTAL ARRANGEMENT

Measurements of ultrasonic attenuation were made by the conventional pulse technique. Pulses (about 1.5-microsecond duration) of the required frequency of oscillation were fed at a rate of about 1000 per second to a 1/2-in.

¹Manuscript received June 26, 1959.

Contribution from the Department of Physics, Royal Military College of Canada, Kingston, Ontario.

X-cut quartz crystal which converts them into pulses of longitudinal waves of the same frequency. The quartz crystal at the end of the cylindrical specimen acted as a transmitter of the initial pulse as well as the receiver of the successive echoes. The pulse and its echoes were amplified by a preamplifier and a wide band amplifier (5 to 65 Mc/s passband) and exhibited on an oscilloscope (Tektronix 514D). The pulses were photographed or their amplitudes measured by means of a scale and a cathetometer. The ultrasonic attenuation was calculated from the rate of decay of the successive echoes.

The cylindrical specimens were prepared by freezing mercury in a cylindrical bakelite container of inner diameter 35 mm. Four specimens of length varying from 1 cm to 4 cm were used in different runs. The mercury used for these specimens was supplied by the Fisher Scientific Company and contained less than 0.0005% gold and silver and 0.0001% base metals. After the quartz crystal was wetted with distilled water, it was placed on the liquid mercury specimen. The specimen container floated on a small pool of mercury. It was fixed in position by first freezing the pool. The mercury specimen was then slowly cooled with its top and bottom surfaces parallel and horizontal. The thin layer of ice sealed the quartz crystal to the mercury specimen. The ice seal has been found to be quite satisfactory at low temperatures with sufficiently low seal loss to enable us to make measurements on several echoes at 60 Mc/s.

The cryostat used was of conventional design. Temperatures down to 1.2° K were obtained by pumping and maintained by a Cartesian manostat. The temperature was determined by measuring the vapor pressure over the liquid helium bath. Temperatures up to 4.6° K were obtained by pressurizing the helium Dewar.

Magnetic fields were obtained by two liquid air cooled Helmholtz coils; one was used for longitudinal fields and the other produced a field perpendicular to the axis of the Dewar and the specimen. The highest field available to us during this work was 880 oersteds.

RESULTS

Figure 1 shows a plot of the attenuation of 60 Mc/s longitudinal waves in pure mercury as a function of temperature. The 'normal state' curves were obtained by applying the critical magnetic field along the direction of the specimen (longitudinal) and perpendicular to the direction of the specimen (transverse). The critical fields used were taken from the known threshold curve for mercury. To remove the uncertainties introduced by the frozen-in flux, the specimen was warmed above the transition temperature after each pair of superconducting and normal measurements.

Figure 2 shows a plot of attenuation of 20, 34, and 60 Mc/s longitudinal waves in pure mercury as a function of temperature. The dotted curves are those of the normal state obtained by applying the critical longitudinal magnetic field.

To study the dependence of ultrasonic attenuation on the transverse magnetic field, the attenuation at various temperatures is plotted against

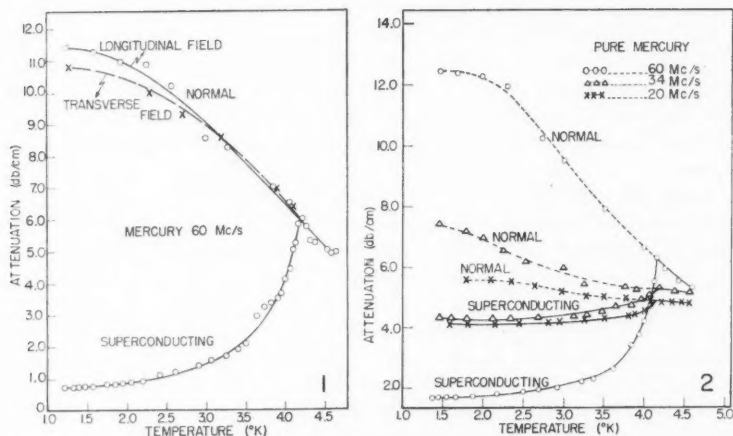


FIG. 1. Temperature dependence of ultrasonic attenuation of 60 Mc/s longitudinal waves in superconducting and normal states of pure mercury.

FIG. 2. Temperature dependence of ultrasonic attenuation of 20, 34, and 60 Mc/s longitudinal waves in superconducting and normal states of pure mercury.

transverse magnetic field as shown in Fig. 3. These plots are quite similar to those obtained by applying a longitudinal magnetic field. The latter are not shown here. The increase in attenuation with transverse field reported by MacKinnon and Myers is not observed.

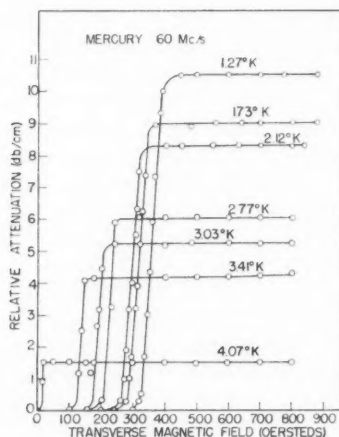


FIG. 3. Ultrasonic attenuation of 60 Mc/s longitudinal waves in pure mercury at various superconducting temperatures as a function of the applied transverse magnetic field.

DISCUSSION

The temperature dependence of ultrasonic attenuation in the superconducting state is similar to that observed in other superconductors. The dependence on frequency of the difference of attenuation in the normal and superconducting states is quite marked. Our results show that for frequencies below 20 Mc/s, a very small change in attenuation will be observed.

In the normal state, the attenuation increases rapidly as the temperature is lowered. The increase is the same for both longitudinal and transverse fields. Furthermore, the attenuation is independent of the applied magnetic field (both longitudinal and transverse) as long as it is greater than the critical field up to a value of 880 oersteds. Measurements at higher magnetic fields are desirable.

Recently, attempts have been made (Morse and Bohm 1957) to use ultrasonic attenuation measurements to verify the Bardeen-Cooper-Schrieffer (BCS) theory of superconductivity (1957). According to this theory, the ratio of attenuation in the superconducting state (α_s) to that in the normal state (α_n) is given by:

$$(\alpha_s/\alpha_n) = 2/[\exp\{\epsilon_0(T)/kT\} + 1]$$

where $2\epsilon_0(T)$ is the energy gap at the Fermi surface and has been calculated by Bardeen. Apart from the question of the validity of the above-mentioned equation, there is little doubt that the ultrasonic attenuation measurements up to date are too crude to be able to distinguish between this relation and a power law. The superconducting attenuation (α_s) measured includes losses due to the seal (between crystal and specimen), diffraction, non-parallelism of the ends of the specimen, etc. Over the temperature ranges studied, these losses are assumed to be constant. Another uncertain factor is the normal attenuation α_n . No two observers have obtained the same dependence of α_n with temperature. In fact, whereas the measurements on single crystals of lead by Bömmel (1954) and tin by Mason and Bömmel (1956) show a marked dependence of α_n on temperature, which is somewhat similar to that observed here in Fig. 1 for pure mercury, those of Morse and Bohm (1958) on single crystal of tin and pure polycrystalline indium show little dependence of α_n on temperature. This is probably because the measurements of α_n are quite sensitive to the purity of the specimen. The values of α_s will also be affected by the presence of frozen-in magnetic flux if a determination of α_s follows immediately a measurement of α_n with the normal state produced by a magnetic field. The presence of this error is difficult to assess from the literature since few authors have reported on the details of their experimental procedures.

The results of Fig. 1 indicate by the marked rise in α_n with decreasing temperature a high degree of purity in the specimen. The α_s values also seem to approach a 'background' value as expected if the seal losses, etc. are constant. It is interesting to note, if perhaps not too significant for the reasons given above, that the theoretical curve calculated on the basis of the BCS theory predicts a less rapid fall of attenuation, with temperature below T_c , than is

here experimentally found. The comparison is made in Fig. 4. Morse and Bohm (1957) have observed a similar qualitative disagreement with BCS theory in the case of superconducting tin and indium.

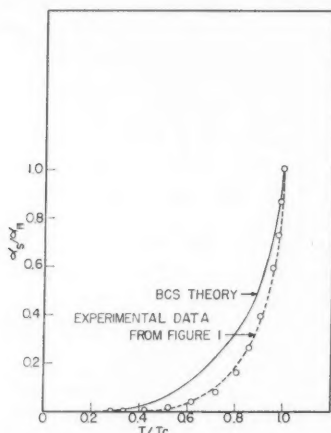


FIG. 4. Theoretical and experimental variation of α_s/α_n against T/T_c .

ACKNOWLEDGMENTS

This work is supported by the Defence Research Board of Canada, Grant No. 7510-14, Project No. D44-75-10-14, whose assistance is gratefully acknowledged. We are also grateful to Mr. W. Horback and Dr. C. K. Hoyt for assistance during the runs.

REFERENCES

- BARDEEN, J., COOPER, L. N., and SCHRIEFFER, J. R. 1957. Phys. Rev. **108**, 1175.
 BÖMMEL, H. E. 1954. Phys. Rev. **96**, 220.
 CHOPRA, K. L. and HUTCHISON, T. S. 1957. Can J. Phys. **36**, 805.
 MACKINNON, L. 1955. Phys. Rev. **100**, 655.
 ——— 1957. Phys. Rev. **106**, 70.
 MACKINNON, L. and MYERS, A. 1958. Proc. Phys. Soc. **73**, 290.
 MASON, W. P. and BÖMMEL, H. E. 1956. J. Acoust. Soc. Am. **28**, 930.
 MORSE, R. W. and BOHM, H. V. 1957. Phys. Rev. **108**, 1094.
 MORSE, R. W., TAMARKIN, P., and BOHM, H. V. 1956. Phys. Rev. **101**, 1610.

FIRST ADSORBED LAYER OF NITROGEN ON PYREX AT 77.4° K¹

J. P. HOBSON

ABSTRACT

A measure of the nitrogen adsorption isotherm on pyrex (Corning 7740) at 77.4° K has been made for pressures above the adsorbed layer ranging from 10^{-3} to 10^{-9} mm Hg. Ultrahigh-vacuum techniques were used. Geometric adsorbing areas were 60 and 32 cm². Coverages ranged approximately from 0.001 to 0.3 monolayer. Full equilibrium was probably not achieved but the data could be represented by the Dubinin-Radushkevich equation,

$$\log \sigma = C - D \left(\log \frac{P}{P_0} \right)^2,$$

for P/P_0 from 10^{-6} to 10^{-11} , where σ is the amount adsorbed.

I. INTRODUCTION

Experimental data on the physical adsorption of nitrogen below pressures of 10^{-5} mm Hg and at temperatures near the normal boiling point are scarce, even though ionization gauges readily operate below this range (Dushman 1949; Alpert 1953). Further isotherm data for pressures below 10^{-5} mm Hg appeared desirable because:

(a) Surface coverages are less than one monolayer in this range and the experiments should provide decisive tests for basic theories of physical adsorption (de Boer 1956).

(b) Low coverage data has been related to the heterogeneity of solid surfaces (Halsey 1952).

(c) Recent theories of chemisorption include as an essential part the van der Waal's interaction between gas and surface (Kisliuk 1957).

(d) Calculations of the thermodynamic functions of adsorption (Drain 1954) may readily be made if isotherms are taken at different temperatures.

(e) A detailed knowledge of the physical adsorption of nitrogen is desirable because of its wide use in the measurement of surface areas (Joy 1953).

(f) The design of vacuum systems containing refrigerated traps may be facilitated by such low pressure data.

It was observed by Hobson and Redhead (1958) that physical adsorption on surface areas of the order of 50 cm² was readily detectable in systems of volume about 1 liter at very low pressures (approximately 10^{-10} mm Hg). This observation was extended to give a measurement of the helium adsorption isotherm at very low pressures at 4.2° K on pyrex (Hobson 1959). The present work applies the same exploratory method to the physical adsorption of nitrogen.

With nitrogen a Bayard-Alpert gauge (Bayard and Alpert 1950) was used as the pressure-sensitive element because its low pumping speed was useful.

¹Manuscript received July 8, 1959.

Contribution from the Radio and Electrical Engineering Division, National Research Council, Ottawa, Canada.

Issued as N.R.C. No. 5341.

This gauge pumps as it measures (Young 1956; Bills and Carleton 1958) and may re-emit some of the gas which it has pumped (Varnerin and Carmichael 1957). However, these gauge processes had not been examined by the above authors in the pressure range used in the present measurements, and for unambiguous interpretation of some of the adsorption data, at least a semi-quantitative knowledge of these processes was required. The gauge processes have been examined concurrently with the adsorption measurements and a paper on these processes will be submitted for publication shortly.

II. APPARATUS

The apparatus is shown in Fig. 1. It is almost identical with that reported previously for helium adsorption (Hobson 1959). The envelope was pyrex

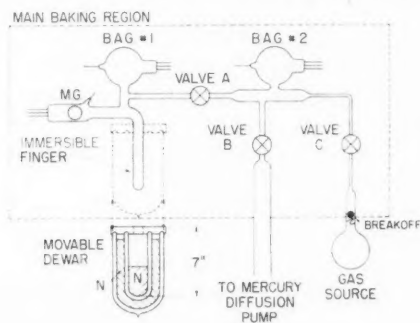


FIG. 1. Apparatus.

glass (Corning 7740). The valves were ultrahigh-vacuum valves (Alpert 1953; Bills and Allen 1955). The Bayard-Alpert gauges (B.A.G. Nos. 1 and 2) were of standard design and were operated with collector at ground potential (i.e., zero); filament, +45 volts; grid, +300 volts; and grid current variable between 8 milliamperes and 40 microamperes. The ion current of B.A.G.-1 was continuously recorded up to currents of 3×10^{-7} amperes. The main adsorption volume, V_1 (938 cm³), was to the left of valve A and contained a magnetron pressure gauge not used in the measurements, a Bayard-Alpert gauge (B.A.G.-1) which was the major measuring element of the experiment, and a finger which could be immersed in liquid nitrogen at 77.4° K. Use of a double Dewar reduced the loss rate of N₂ in the inner Dewar to a low value. The level of liquid in the inner Dewar was visible at all times and could readily be adjusted to a fixed mark on the finger. Valve A controlled nitrogen flow into V_1 . Valve C controlled flow from the gas source of spectroscopically pure nitrogen to the central volume, V_2 , where pressure, P_2 , was measured by B.A.G.-2. V_2 could be pumped through valve B with a mercury diffusion pump suitably trapped with liquid nitrogen.

The system was prepared for measurement by baking the region shown in Fig. 1 for 15 hours at 450 to 400° C with all valves open and with the mercury

diffusion pump running. Before measurements were begun pressures of 10^{-10} mm Hg were obtained in V_1 with valve A closed and B.A.G.-1 operating at 8 milliamperes. This background pressure is mainly the result of the gauge pumping against the helium diffusing through the pyrex envelope (Rogers, Buritz, and Alpert 1954). In V_2 a background pressure of 2×10^{-10} mm Hg was obtained with valve C open prior to breaking the seal of the gas source.

III. EXPERIMENTAL PROCEDURE

A typical adsorption isotherm run was performed as follows. After B.A.G.-1 was outgassed with valves A and B open, A was closed and equilibrium obtained in about 40 minutes. The finger was then immersed to a fixed mark with the grid current of B.A.G.-1 (I^-) 8 milliamperes to keep the helium background pressure low. This immersion caused a pressure drop of about 20%. I^- was next reduced to 80 microamperes (or 40 microamperes) to reduce the pumping speed of the gauge during adsorption measurements, and was left at this value. Upon reduction of I^- the pressure in V_1 began to rise slowly because the pumping speed of the gauge to helium was also reduced. The rise was recorded until its characteristics were established (after 20 to 30 minutes) and the pressure reading at any future time due to helium diffusion could be predicted. After valve A was closed a steady high nitrogen pressure was established in V_2 ($P_2 \sim 10^{-3}$ mm Hg) by manipulation of valves B and C. Valve A was then cracked open and nitrogen allowed to bleed into V_1 until a pressure of about 2×10^{-9} mm Hg, or about five times the estimated background pressure, was established. Valve A was then closed and P_1 allowed to stabilize for 15 to 20 minutes. The pressure in excess of estimated background was taken as the nitrogen pressure above the layer adsorbed on the inside surface of the finger. The Dewar was then lowered, permitting the adsorbed nitrogen to desorb. The pressure reached a peak, from whose magnitude the quantity of N_2 adsorbed was calculated, and then the gas in V_1 was pumped down by B.A.G.-1 until the characteristic pumping time of order minutes could be established. There followed a set of operations shown in Fig. 2. This set was repeated at increasing pressures up to pressures of 10^{-3} mm Hg. With reference to Fig. 2 it may be seen that the pressure fall when the finger was immersed (characteristic time τ_T) was much faster than when the gauge was

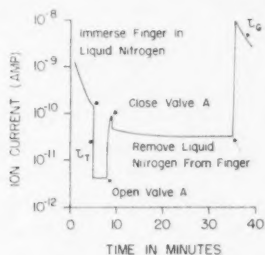


FIG. 2. Experimental sequence.

pumping alone; that is, $\tau_G \gg \tau_T$. This relation held throughout the pressure range investigated and indicates that the slowly pumping gauge represents a minor fraction of the total pumping speed of the system in the presence of liquid nitrogen. The variations observed in τ_G will be discussed in the paper on gauge processes.

Figure 2 was analyzed with the following relations:

$$(1) \quad \text{gauge pressure } P_1 = (I^+)/(kI^-) \text{ mm Hg}$$

where I^+ is the gauge ion current,

I^- is the gauge electron current,

and k is the gauge constant = 25 (mm Hg) $^{-1}$ for the gauges used.

Over most of the pressure range covered the pressure P above the adsorbed layer at $T = 77.4^\circ \text{ K}$ differed from P_1 at $T = 295^\circ \text{ K}$ according to the thermomolecular formula,

$$(2) \quad \frac{P}{P_1} = \sqrt{\frac{T}{T_1}} = \sqrt{\frac{77.4}{295}} = 0.512.$$

For P_1 from 5×10^{-5} to 10^{-3} mm Hg, eq. (2) was corrected with the formula of Liang (1951).

Once valve A was closed it was assumed that

$$(3) \quad n_a + n_g + n_i = C \text{ (constant)}$$

where n_a is the number of molecules physically adsorbed,

n_g is the number of molecules in gaseous phase,

and n_i is the number of molecules ionically pumped by the gauge since closure of A.

Now

$$(4) \quad n_g = aP_1$$

where $a = 3.31 \times 10^{19}$ molecules per mm Hg for $V_1 = 938 \text{ cm}^3$. (Where necessary a minor correction was applied to eq. (4) because a small portion of V_1 was not at room temperature.)

$$(5) \quad \frac{dn_i}{dt} = \frac{aP_1}{\tau_G} \text{ molecules/second} \quad (\text{if } \tau_G \text{ is in seconds}).$$

Combining eqs. (1) and (5),

$$(6) \quad n_i = \frac{1}{\tau_G} \frac{a}{kI^-} \int_0^t I^+ dt$$

where $\int_0^t I^+ dt$ is the ionic charge in coulombs obtained by integrating the observed current following closure of A.

When liquid nitrogen is removed from the finger n_a is reduced to zero. Since n_g and n_i are given by eqs. (4) and (6), respectively, C in eq. (3) may then be found. Once C is known, n_a can be found at any time by combining eqs. (3), (4), and (6). The adsorption isotherm is concerned with the simultaneous value of n_a and of P . The values given in Section IV were obtained just before liquid nitrogen was removed from the Dewar.

The adsorbing area was taken as the simple geometric area of the inside surface of the finger (inside diameter, 2.2 cm; outside diameter, 2.5 cm) lying below the plane of the liquid nitrogen level. A copper-constantan thermocouple bound to the outside of the finger showed no change in temperature while immersed in the liquid. The temperature rose 20° K per millimeter immediately above the liquid surface, which indicates a sharp change in the temperature of the pyrex at the liquid surface. Standard adsorbing areas of 60 cm² and 32 cm² were used in the measurements.

IV. RESULTS

Figure 3 gives the results of six runs with I^- either 80 microamperes or 40 microamperes, giving gauge pumping speeds differing by a factor of 2, and

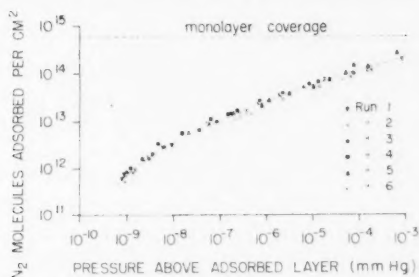


FIG. 3. Adsorption isotherm measurements for nitrogen on pyrex at 77.4° K.

- Run 1: $I^- = 80 \mu\text{amp}$, $A = 60 \text{ cm}^2$, pressure increasing.
 Run 2: $I^- = 80 \mu\text{amp}$, $A = 60 \text{ cm}^2$, pressure increasing.
 Run 3: $I^- = 80 \mu\text{amp}$, $A = 60 \text{ cm}^2$, pressure increasing.
 Run 4: $I^- = 80 \mu\text{amp}$, $A = 22 \text{ cm}^2$, pressure increasing.
 Run 5: $I^- = 40 \mu\text{amp}$, $A = 32 \text{ cm}^2$, pressure increasing.
 Run 6: $I^- = 80 \mu\text{amp}$, $A = 60 \text{ cm}^2$, pressure decreasing.

with adsorbing areas of 60 or 32 cm². Most runs were made on successive days with the adsorbent kept at room temperature overnight at a pressure in the 10⁻¹⁰ mm Hg range. One run (open circles) was performed with pressure decreasing, that is, the opening of valve A (Fig. 2) reduced rather than increased the pressure in V_1 . The dashed line in Fig. 3 has been drawn visually. Monolayer coverage based on a nitrogen molecular area of 16.2 Å² has been included for reference.

The approach to physical adsorption equilibrium is shown in Fig. 4. The solid lines show the observed time dependence of the pressure following closure of valve A (Fig. 2) at three well-separated pressures, for a run with increasing pressures. If no pumping gauge were present in the system it would be expected that these pressures would become time-independent when physical adsorption equilibrium had been achieved. But from eq. (3) $n_a + n_g$ continuously falls since n_l continuously increases (eq. (6)). Thus a pressure falling with time is to be expected even when physical adsorption equilibrium has been essentially achieved. An approximation to the expected fall is given by the

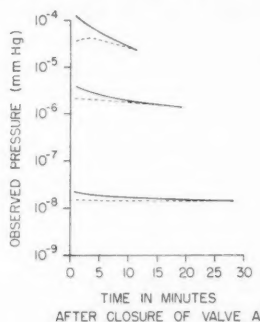


FIG. 4. Approach to equilibrium: solid line, observed; dotted line, calculated.

dashed lines in Fig. 4, which have been obtained by calculating n_a from eqs. (3), (4), and (6) for the runs shown, and obtaining the appropriate pressure from Fig. 3. Identity in slope between the solid and dashed lines is an indication that physical adsorption equilibrium has been achieved. The dashed line has arbitrarily been joined to the solid line at the end point. The approach to final equilibrium is apparently slow and true equilibrium was probably not achieved in these measurements. It may be noted that the true equilibrium values are expected to be lower than those observed. Failure to standardize the time between closure of A and desorption (see Fig. 2) contributes to the scatter in Fig. 3.

V. DISCUSSION

Figure 5 compares the present results with some other results on the physical adsorption of nitrogen at temperatures near the normal boiling point of nitrogen. The units are those commonly used in the adsorption literature. No

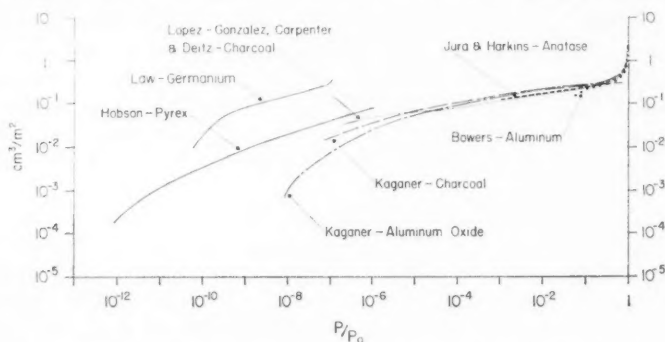


FIG. 5. Comparison of experimental results on the physical adsorption of nitrogen near $T = 77.4^\circ \text{K}$.

Lopez-Gonzalez, Carpenter, and Deitz (1955), Char 27, $T = 77.7^\circ \text{K}$; Jura and Harkins (1944), $T = 77.7^\circ \text{K}$; Bowers (1953), $T = 77.4^\circ \text{K}$; Kaganer (1957), aluminum oxide, $T = 77.4^\circ \text{K}$; Kaganer (1958), coconut charcoal, $T = 77.6^\circ \text{K}$; Law (1955), $T = 77^\circ \text{K}$.

absolute calibration of B.A.G.-1 was made in the present experiments and the assumption of equality between geometric and adsorbing areas was arbitrary. Thus detailed quantitative comparisons between the present results and those of others are not significant but comparisons of the general forms of the results should be significant.

There is a general continuity between our results for small (approximately 50 cm^2) plane surfaces and the results of Lopez-Gonzalez *et al.* (1955) using a surface area of $3 \times 10^5 \text{ cm}^2$. Law (1955), using a small surface of germanium (approximately 10 cm^2), finds the first layer complete at a pressure of 4 to $5 \times 10^{-5} \text{ mm Hg}$ (P/P_0 approximately 10^{-7}), whereas the other results of Fig. 5 indicate the adsorption of a quantity corresponding to the first layer at P/P_0 approximately 10^{-1} . However, despite the absolute difference, the results of Law (1955) and Kaganer (1957) have the same general form, and, in particular, Henry's law of proportionality between quantity adsorbed and pressure above the adsorbed layer is either achieved or approached in the saturation range $10^{-10} < P/P_0 < 10^{-8}$, whereas in the present results Henry's law is not valid for $P/P_0 > 10^{-12}$. In seeking an analytic expression for our results we tested the Dubinin-Radushkevich equation (Dubinin and Radushkevich 1947) employed by Kaganer (1957, 1958) for $P/P_0 \gtrsim 10^{-8}$. This equation is

$$(7) \quad \log \sigma = C - D(\log P/P_0)^2$$

where σ is the amount adsorbed,

P is the pressure above the adsorbed layer,

P_0 is the equilibrium vapor pressure above the liquid at the same temperature,

and D is a constant dependent on the square of the absolute temperature,
and

$$(8) \quad C = \log \sigma_m$$

where σ_m is the quantity adsorbed in the first layer. Points from the dashed line of Fig. 3 are plotted in Fig. 6 in the co-ordinates suggested by eq. (7), with

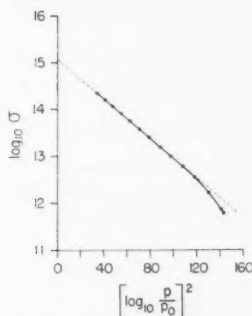


FIG. 6. Test of the Dubinin-Radushkevich equation.

σ expressed in molecules/cm². The result is a straight line for $10^{-11} \leq P/P_0 \leq 10^{-6}$. This result was not anticipated, particularly in view of Kaganer's rejection of this equation for $P/P_0 \lesssim 10^{-5}$. The value of σ_m obtained from eq. (8) by extrapolating the result of Fig. 6 to $P = P_0$, as done by Kaganer (1957), is $\sigma_m = 1.1 \times 10^{15}$ molecules/cm². This is almost a factor 2 above the expected monolayer coverage of 6.2×10^{14} molecules/cm², but the discrepancy appears to be within the possible error of the experiment. The value of D obtained from the slope of Fig. 6 is 0.0212, which is within the range found by Kaganer (1958) for various adsorbents (0.0169 to 0.0564). Thus the application of eq. (7) to our data gives results generally compatible with those of Kaganer (1957) but at much lower saturation values.

The approach to equilibrium shown in Fig. 3, while slow, is nevertheless much faster than the approach to equilibrium shown by Lopez-Gonzalez *et al.* (1955) in their Fig. 4. In the latter case a single isotherm point, if taken $\frac{1}{2}$ hour after the beginning of the process of equilibrium, would have yielded pressures over the adsorbed layer some three orders of magnitude above the equilibrium level. The shorter times of the present experiment are probably the result of the thermal contact between bath and adsorbing surface. The characteristic thermal time of pyrex in the present experiment is

$$(9) \quad t = \frac{d^2 c \rho}{k} \text{ seconds}$$

where d is the thickness of the wall,

c is the specific heat,

ρ is the density,

and k is the thermal conductivity.

For pyrex at 77° K, t is of order a few seconds, which is experimentally confirmed by the small value of τ_T shown in Fig. 2.

VI. CONCLUSIONS

1. Ultrahigh-vacuum techniques are applicable to measurements of the physical adsorption of nitrogen on small surface areas.
2. Use of these techniques can reduce the time required to reach equilibrium.
3. The physical adsorption of nitrogen on pyrex at 77.4° K was found to follow the Dubinin-Radushkevich equation for P/P_0 from 10^{-6} to 10^{-11} .

ACKNOWLEDGMENTS

The author wishes to thank all members of the Electron Physics Group of the Radio and Electrical Engineering Division of these laboratories for many and varied contributions to this work.

REFERENCES

- ALPERT, D. 1953. *J. Appl. Phys.* **24**, 860.
 BAYARD, R. T. and ALPERT, D. 1950. *Rev. Sci. Instr.* **21**, 571.
 BILLS, D. G. and ALLEN, F. G. 1955. *Rev. Sci. Instr.* **26**, 654.
 BILLS, D. G. and CARLETON, N. P. 1958. *J. Appl. Phys.* **29**, 692.

- BOWERS, R. 1953. *Phil. Mag.* **44**, 467.
- DE BOER, J. H. 1956. *Advances in Catalysis*, **8**, 17.
- DRAIN, L. E. 1954. *Sci. Progr.* **42**, 608.
- DUBININ, M. M. and RADUSHKEVICH, L. V. 1947. *Proc. Acad. Sci. U.S.S.R.* **55**, 331.
- DUSHMAN, S. 1949. *Vacuum technique* (John Wiley & Sons, Inc., New York), Chap. 6.
- HALSEY, G. D. 1952. *Advances in Catalysis*, **4**, 259.
- HOBSON, J. P. and REDHEAD, P. A. 1958. *Can. J. Phys.* **36**, 271.
- HOBSON, J. P. 1959. *Can. J. Phys.* **37**, 300.
- JOY, A. S. 1953. *Vacuum*, **3**, 254.
- JURA, G. and HARKINS, W. D. 1944. *J. Am. Chem. Soc.* **66**, 1356.
- KAGANER, M. G. 1957. *Proc. Acad. Sci. U.S.S.R.* **116**, 603.
- KAGANER, M. H. 1958. *Proc. Acad. Sci. U.S.S.R.* **122**, 416.
- KISLIUK, P. 1957. *Phys. and Chem. Solids*, **3**, 95.
- LAW, J. T. 1955. *J. Phys. Chem.* **59**, 543.
- LIANG, S. CHU, 1951. *J. Appl. Phys.* **22**, 148.
- LOPEZ-GONZALEZ, JUAN DE DIOS, CARPENTER, F. G., and DEITZ, V. R. 1955. *J. Research Natl. Bur. Standards*, **55**, 11.
- ROGERS, W. A., BURITZ, R. S., and ALPERT, D. 1954. *J. Appl. Phys.* **25**, 863.
- VARNERIN, L. J. and CARMICHAEL, J. H. 1957. *J. Appl. Phys.* **28**, 913.
- YOUNG, J. R. 1956. *J. Appl. Phys.* **27**, 926.

DESIGN OF GRADIENTLESS FURNACES¹

M. J. LAUBITZ

ABSTRACT

Temperature distributions in cylindrical furnaces are discussed, and design data are given which permit the construction of short furnaces in which the temperature varies less than 0.5% along the central half of the length of the heater. Formulae are also given for the calculation of temperature distributions in conventional furnaces with uniformly wound heaters.

1. INTRODUCTION

Many high-temperature experiments require the absence of temperature gradients along the working space, and in preparing for such experiments one is faced with the problem of designing a furnace to meet that requirement. Yet information pertinent to the design of high-temperature furnaces is exceedingly vague. One sometimes encounters estimates of temperature distribution in particular furnaces, or meets such enlightening statements as "to minimize the temperature gradient inside the furnace, the winding density was increased towards the ends of the heater". However, detailed information facilitating the design of furnaces to meet particular requirements seems to be missing. It was to alleviate this deficiency of information that we have undertaken an extensive study of small cylindrical laboratory furnaces. The object in view was twofold: primarily, to obtain definite design formulae for construction of furnaces with extended gradientless regions; and secondarily, to obtain formulae which would permit the calculation of temperature distributions in conventional furnaces with uniformly wound heaters.

2. DESIGN OF GRADIENTLESS FURNACES

2.1 *Description of the Problem*

The furnace considered here is described by the following parameters (Fig. 1): it is of length L , outer radius r_b , and inner radius r_a . It is important to notice that r_a refers to the outside dimensions of the tube on which the heater, of length L_H , is wound. The furnace is filled with an insulation of conductivity K_p . It is water-cooled along r_b , and its top and bottom are characterized by a surface conductance h_r . The inside tube of the furnace contains the "charge", that term covering all of the materials and objects that are inserted into the furnace.

In the normal procedure of designing a furnace for an experiment, the charge is given, and it determines both the gradients that can be tolerated and the dimensions of the region over which the gradients have to be controlled. Gradientless regions can always be obtained in furnaces with uniformly

¹Manuscript received July 20, 1959.

Contribution from the Division of Applied Physics, National Research Council, Ottawa, Canada.

Issued as N.R.C. No. 5342.

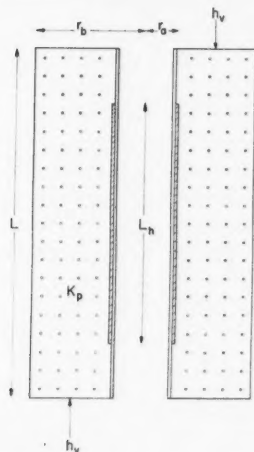


FIG. 1. Cross section of the cylindrical furnace showing the parameters that describe it.

wound heaters if these furnaces are made very long and thin. Frequently, however, such furnaces are unacceptable because of the space they occupy, awkwardness in handling, or their large power consumption. Short furnaces with extensive gradientless regions can be constructed if the winding distribution along the length of the heater is non-uniform, the non-uniformity being a function of both furnace parameters and charge. One can look at this non-uniformity as being determined by the over-all heat flow pattern, which can be divided conveniently into two parts: the heat flowing predominantly through the furnace proper, and the heat flowing predominantly down the central tube and charge. These two flow patterns are, of course, not independent of each other, but it turns out that they can be treated as such to a good approximation.

The heat flow pattern and temperature distribution in the furnace proper are functions of three geometrical parameters, r_b/r_a , L/r_a , and L_h/L , of the winding distribution along the heater, and of the ratio of heat transfer parameters K_p/Lh_r . A formal analytical solution can be obtained for these functions, being for the general case a double infinite series of Bessel functions of the first and second kind, of real and imaginary arguments. This solution is much too complicated to be of any practical use; it was therefore decided to tackle that part of the problem by means of an electrical analogue.

The heat flowing down the central tube is a function of its geometrical parameters and of the heat conductivity of that tube and of the charge. It was found that this part of the heat loss can be calculated accurately enough in the linear flow approximation and subsequently added to the main flow pattern. The winding distribution of the heater is then arranged so as to meet both heat flow requirements.

2.2 Heat Flow through the Furnace Proper

The flow patterns in the furnace proper were determined by means of an electrical analogue, the chief characteristics of which are here briefly described. Because of the cylindrical symmetry of the furnace, only a two-dimensional resistor network was required. The longitudinal grid of the network was linear, each subdivision corresponding to a length $L/15$ of the furnace. The radial grid was logarithmic, the junctions being concentrated in the region of interest close to r_a ; it had six subdivisions in the distance $r_b - r_a$. The resistors used in constructing the network were of 0.2% accuracy. Power was supplied by batteries and the voltages were measured with a precision vacuum tube voltmeter. The resistors employed in the network determined the geometrical ratios r_b/r_a and L/r_a , and for each set of these ratios a number of boundary conditions was applied: These corresponded to various values of L_H/L , K_p/h_vL , and to various power input distributions along the heater. The results of interest to the design of gradientless furnaces are those which give the power distribution along the heater for a constant heater temperature as a function of r_b/r_a , L/r_a , L_H/L , and K_p/h_vL , and which are listed in Tables I and II. Table I gives the power input factor, q , from

TABLE I
Power input factor, q , for gradientless furnaces

r_b/r_a	L/r_a	K_p/h_vL	q		
			$L_H/L = 1$	$L_H/L = 11/15$	$L_H/L = 7/15$
4	32	∞	4.54	3.45	2.24
4	32	0	4.87	3.47	2.26
4	16	∞	4.56	3.66	2.45
4	16	0	5.18	3.72	2.47
4	8	∞	4.56	3.91	2.87
4	8	0	7.07	4.38	2.98
8	16	∞	3.02	2.57	1.85
8	16	0	4.47	2.84	1.92
4	16	∞	4.56	3.66	2.45
4	16	0	5.18	3.72	2.47
2	16	∞	9.10	6.85	4.43
2	16	0	9.53	6.85	4.43

which the power, Q_M , required to raise the furnace to a temperature T_0 can be calculated by means of the equation

$$(1) \quad Q_M = qK_pLT_0$$

where K_p is the conductivity of the insulation and L is the length of the furnace, q is, of course, dimensionless. Table II gives the power distribution factor, a_n , from which the power distribution along the heater can be calculated from

$$(2) \quad Q(l_n)/Q(l_0) = 1.000 + a_n \times 10^{-3}.$$

It must be remembered that as the analogue has a finite grid, the power

TABLE II
Power distribution factor, a_n , for gradientless furnaces

r_b/r_a	L/r_a	$K_p/h_e L$	$L_H/L = 1$										$L_H/L = 11/15$										$L_H/L = 7/15$									
			a_0	a_1	a_2	a_3	a_4	a_5	a_6	a_7	a_8	a_9	a_{10}	a_{11}	a_{12}	a_{13}	a_{14}	a_{15}	a_{16}	a_{17}	a_{18}	a_{19}	a_{20}	a_{21}	a_{22}	a_{23}	a_{24}	a_{25}	a_{26}	a_{27}	a_{28}	a_{29}
4	32	∞	0	0	0	0	0	0	0	0	0	0	0	0	0	3	14	190	0	0	14	190										
4	32	0	0	0	0	0	0	4	12	41	468	0	0	4	9	23	205	0	4	15	193											
4	16	∞	0	0	0	0	0	0	0	0	0	0	0	11	23	86	424	0	5	62	414											
4	16	0	0	0	0	6	14	63	221	624	0	0	11	23	93	474	0	5	62	420												
4	8	∞	0	0	0	0	0	0	0	0	0	0	11	26	59	150	579	0	26	132	610											
4	8	0	0	6	20	59	141	278	720	2480	0	13	47	114	280	942	0	27	151	666												
8	16	∞	0	0	0	0	0	0	0	0	0	0	8	20	51	142	501	0	26	110	513											
8	16	0	0	8	22	56	133	258	592	2019	0	11	33	93	233	781	0	28	126	554												
4	16	∞	0	0	0	0	0	0	0	0	0	0	11	33	93	233	781	0	5	62	414											
4	16	0	0	0	0	6	14	63	221	629	0	0	11	23	93	474	0	5	62	420												
2	16	∞	0	0	0	0	0	0	0	0	0	0	0	0	0	9	145	0	0	9	145											
2	16	0	0	0	0	0	0	0	0	20	358	0	0	0	0	9	151	0	0	9	150											

distribution is given not as a continuous function, but as discontinuous values pertinent to a basic interval of length l . For our analogue, $l = L/15$, and these intervals are so numbered that l_0 refers to the middle section of the furnace. Thus $Q(l_n)$ is the power dissipated by the $(n+1)$ th section of the heater counted from the center (the central section being $n = 0$) and, as the center is a plane of symmetry, will be the same for either end.

Both the q 's and the a 's are given only for two values of the heat transfer parameter $K_p/h_e L$: zero and infinity. $K_p/h_e L = \infty$ corresponds to perfect insulation at the ends, while $K_p/h_e L = 0$ to perfect water-cooling, which can absorb any amount of heat without an increase in temperature. These form the limits for any realistic furnace ends, and as for most cases the values of q and a for $K_p/h_e L$ equal to infinity are close to those for it equal to zero, there seemed little point in including intermediate values in the tables. Some of the ratios studied, such as $L/r_a = 8$ or $L_H/L = 1$, have in themselves little practical value. They are included, however, to facilitate graphical interpolation.

As mentioned before, the analogue had a grid of 6×15 . It was decided to run a check calculation on a finer grid, to observe the possible effect of grid size on the results. The calculation was done by the relaxation procedure on a grid of 12×25 , for a furnace with parameters $r_b/r_a = 4$, $L/r_a = 14$, $L_H/L = 19/25$, and $K_p/h_e L = 0$, and the results were compared with those interpolated from the analogue tables. The agreement is quite remarkable. The power input factors agree to within 0.1% and the power input distributions, shown in Fig. 2, also agree very well, indicating that the grid selected for the analogue is sufficiently fine.

In designing the analogue the conductivity of the insulation filling the furnace which the analogue represents was assumed to be independent of temperature. This is, however, no real limitation, as the results can easily be adjusted to include insulation whose conductivity is not constant. By using Kirchhoff's substitution (Carslaw and Jaeger 1959) it can be very easily

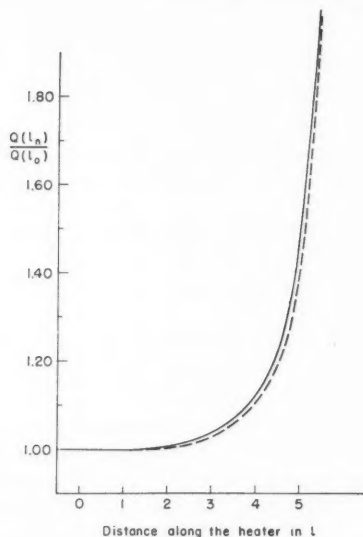


FIG. 2. Power distribution along the heater of a gradientless furnace $r_b/r_a = 4$, $L/r_a = 16$, $L_H/L = 11/15$, and $K_p/h_v L = 0$.

Solid line, given by analogue of grid 6×15 ; broken line, given by analogue of grid 12×25 .

shown that for $K_p/h_v L = \infty$ or 0 , the use of insulating powder with conductivity varying arbitrarily with temperature will leave the power distribution factor unaffected. The power input will be changed only by the substitution of an effective conductivity, K_e , for K_p in eq. 1, where

$$K_e = \frac{1}{T_0} \int_0^{T_0} K_p(T) dT.$$

$K_p(T)$ is the temperature-dependent conductivity of the insulation. It must be stressed that these results are valid only if $K_p/h_v L = 0$ or ∞ . For any other $K_p/h_v L$ the power distribution factor will be affected, but, as before, the values for $K_p/h_v L = 0$ and ∞ form the limits of its variation.

2.3 Central Tube Losses

The analogue considers only the heat flowing through the furnace proper. Heat, of course, flows also along the central tube and charge towards the ends. This heat flow is part of the over-all flow pattern, but, as mentioned before, will be treated here as independent of the furnace body flow, and in the linear approximation. Such an approximation is justified because the heat flowing down the tube is usually only a small part of the total heat loss. Thus, the quantity of heat flowing down the central tube, Q_E , is given by

$$(3) \quad Q_E = K_E A_T \frac{T_0 - T_E}{\Delta X}$$

where T_0 is the temperature in the center of the furnace,
 T_E is the temperature of the end of the furnace,
 $A_T = \pi r_a^2$ is the cross-sectional area of the central tube,
 K_E is the equivalent conductivity of tube and charge taken at
 a temperature of $\frac{1}{2}(T_0 + T_E)$,
 ΔX is the distance from the place on the heater where provision
 for the supply of Q_E is made to the end of the furnace.
 If the heater is so arranged that Q_E is provided in its end sections, then

$$\Delta X = 8/15L - 1/2L_H.$$

In order to be able to use eq. 3, one must make some sort of estimate of T_E . In our experiments we have found T_E to be a very slowly varying function of T_0 , being for most furnaces about 180°C for $T_0 = 500^\circ\text{C}$ and 250°C for $T_0 = 1300^\circ\text{C}$. In fact, we have found that in the range of $T_0 = 500^\circ\text{C}$ to 1300°C , $T_E = 200^\circ\text{C}$ gives Q_E in close agreement with experimental results.

Inspection of eqs. 2 and 3 reveals a bad feature of gradientless furnaces, namely that if the furnace is to operate over a range of temperatures, the heater winding has to be made in two parts. This arises from the fact that the temperature dependence of Q_M and Q_E are quite different, making the ratio of Q_E/Q_M a function of temperature. If, therefore, the end losses Q_E are to be provided by merely increasing the winding density of the heater in its end sections, the furnace will be strictly gradientless at one temperature only. To have the furnace operate over a range of temperatures, a separately controlled heater must be provided to supply Q_E . This auxiliary heater can be arranged in various ways; we ourselves have tried three different methods. One was to insert small end heaters in the shape of plugs into the central tube; another was to wind the auxiliary heater on top of the two end sections of the main heater; and the third was to wind the main heater extending only for a length $(L_H - 2l)$, and to wind the two end sections separately. The two end heaters supply then not only Q_E , but also the power $Q(l_n)$ of the main heater end section. Of these three arrangements the first gave the best temperature distribution, but the third was easiest to construct and most convenient to handle.

2.4 Comparison of Design Data with Experiment

Several furnaces were constructed to check the design data obtained from the analogue and calculations. The first experiment was made to check the accuracy of the temperature distribution predicted by the analogue. This was done by comparing analogue and observed temperature distributions for a furnace with parameters $r_b/r_a = 4$, $L/r_a = 16$, $L_H/L = 11/15$ and with a uniformly wound heater. The results are shown in Fig. 3. They agree well, the largest deviation being 1.3%.

Next, a gradientless furnace was constructed with parameters $r_b/r_a = 4$, $L/r_a = 16$, $L_H/L = 11/15$, and of length 20 cm. The heater was wound in two parts, with the main winding arranged according to Table II, and an auxiliary winding put over the end sections of the main heater. Figure 4

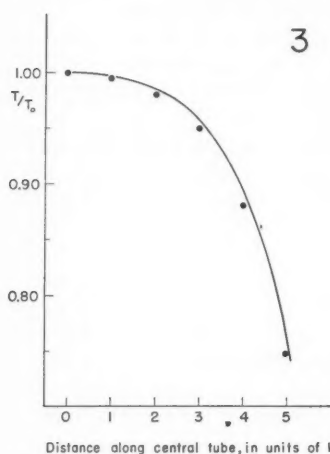


FIG. 3. Temperature distributions in a furnace with uniformly wound heater with parameters $r_b/r_a = 4$, $L/r_a = 16$, $L_H/L = 11/15$, and $T_0 = 1000^\circ\text{C}$. Dots, observed distribution; solid line, predicted by analogue.

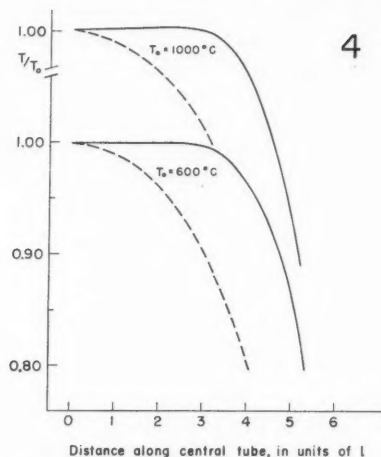


FIG. 4. Observed temperature distributions for furnaces with parameters $r_b/r_a = 4$, $L/r_a = 16$, $L_H/L = 11/15$.

Solid lines, proper gradientless furnace with a two-winding heater; broken lines, uniformly wound furnace.

shows the central temperature distributions observed at $T_0 = 600^\circ\text{C}$ and $T_0 = 1000^\circ\text{C}$. At each T_0 sets of temperature distributions were measured for various ratios of Q_E/Q_M . The results illustrated in Fig. 4 were the best obtained and the experimental values of Q_E/Q_M and Q_M for these distributions are compared in Table III with those calculated from eqs. 1 and 3. Figure 4

TABLE III
Observed and calculated power inputs for gradientless furnaces
with parameters $r_b/r_a = 4$, $L/r_a = 16$, $L_H/L = 11/15$

Design temp. $T_0, ^\circ\text{C}$	Q_M , watts		Q_E/Q_M	
	Calculated	Observed	Calculated	Observed
600	141	135	.197	.208
1000	277	265	.154	.149

shows also temperature distributions for a furnace with the same parameters but a uniformly wound heater.

The winding of the heater for the furnace described above was quite complicated due to the variation of the winding density along its length. It was decided to test experimentally a simplified winding scheme in which the main heater was uniformly wound along all but the very end sections, where the winding density was increased according to Table II. These end sections had a further winding superimposed on them to provide Q_E . The furnace had the

same parameters as above. Figure 5 shows the results obtained at two central temperatures, $T_0 = 500^\circ\text{C}$ and 1000°C , for various Q_E/Q_M . It is seen that at the lower temperature the simplification of the winding has no significant effect on the temperature distribution. At the higher temperature, however,

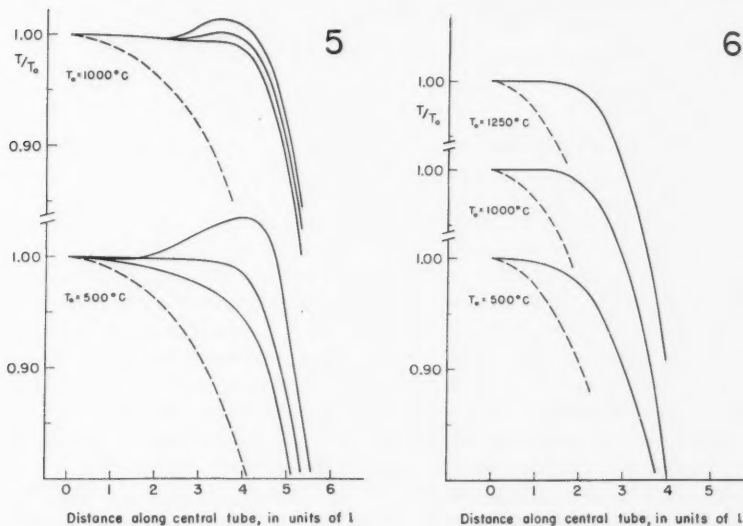


FIG. 5. Temperature distributions for furnaces with parameters $r_b/r_a = 4$, $L/r_a = 16$, $L_H/L = 11/15$.

Solid lines, simplified gradientless furnace with a two-winding heater; broken lines, uniformly wound furnace.

FIG. 6. Temperature distributions for furnace with parameters $r_b/r_a = 4$, $L/r_a = 16$, $L_H/L = 7/15$.

Solid lines, gradientless furnace with a single-winding heater designed for 1250°C ; broken lines, uniformly wound furnace.

it is impossible to obtain a true gradientless region with the simplified winding. It may be mentioned here that the values of Q_M and Q_E/Q_M calculated from eqs. 1 and 3 agreed well with those observed for optimum temperature distribution.

The two previously described experiments were carried out with furnaces in which the heater had a double winding. To conclude the experiments, a furnace was constructed with a single-winding heater, designed to operate at the temperature of 1250°C . The furnace had parameters $r_b/r_a = 4$, $L/r_a = 16$, $L_H/L = 7/15$, and was 20 cm long. Figure 6 shows the temperature distribution obtained for a central temperature T_0 of 500°C , 1000°C , and 1250°C , and Table IV gives the length of the region in which the temperature varied by less than 0.5%. It is seen from that table that the furnace could be successfully used in the temperature range of 1000°C to 1300°C (maximum temperature permitted for heater wire), but that the uniform temperature region is

TABLE IV

Temperatures, power consumption, and length of gradientless region of the furnace with parameters $r_b/r_a = 4$, $L/r_a = 16$, $L_H/L = 7/15$

Power input, watts	Central temp., °C		Length of gradientless region, % of L_H
	Calculated	Observed	
83	500	506	32
173	1000	1005	49
216	1250	1243	53

substantially restricted at 500° C. Table VI also shows the comparison between the design temperature, and the central temperature reached with a power input calculated for that design temperature from eqs. 1 and 3.

2.5 Discussion and Summary

In practical work the term "gradientless" does not mean precisely zero gradient, but it is usually defined with respect to a certain maximum limit on the gradients that can be tolerated in the experiment. In our work on furnaces, we have arbitrarily taken a region as "gradientless" if the maximum variation in temperature encountered in that region is equal to or less than 0.5%, the temperature being expressed in degrees Celsius. With reference to that definition, all the furnaces that we have constructed according to the above outlined procedures had a gradientless region of 50 to 60% of the heater length, roughly five times longer than that which would be obtained with uniformly wound heaters. Although such furnaces are a substantial improvement on the conventional ones, they still fall short of the ideal in which the gradientless region extends over the whole length of the heater. This shortcoming, we believe, is mainly due to the method employed in supplying the end losses, Q_E . Ideally, Q_E should be supplied by a wafer-thin circular heater located inside the central tube at the ends of the main heater. It seems likely that for best results this heater would have to be wound non-uniformly, producing more heat at the edges than at the center. With such means of supplying Q_E the length of the gradientless region should approach L_H , its limit. It is debatable, however, whether the extra extension in the length of the gradientless region is worth the trouble of constructing such complicated end heaters.

By way of summary the steps necessary to the design of a gradientless furnace will be briefly described. The starting point is the charge, which is determined by the experiment to be undertaken. Its dimensions give r_a and L_H , the latter on the assumption that the gradientless region extends over one half of the length of the heater. Then the ratios r_b/r_a and L/r_a are determined, usually as a compromise between keeping L/r_a a minimum for ease of handling and r_b/r_a a maximum to keep the power consumption low, and at the same time avoiding a wildly varying winding distribution which complicates the construction of the heater. Q_E and Q_M are then computed from the known parameters, the design temperature T_0 , and the conductivities

of the materials employed in construction. In that connection two references may be given for the thermal conductivity of ceramics; Kingery *et al.* (1954) gives extensive data for solid ceramics while Laubitz (1959) discusses the conductivity of powders. Knowing Q_E and Q_M with its winding distribution, the heater can be designed taking into account the nature of the power supply available and the permissible surface power load of the heater wire.

3. TEMPERATURE DISTRIBUTION IN FURNACES WITH UNIFORMLY WOUND HEATERS

3.1 The Pure Radial Heat Flow Approximation

In most cylindrical furnaces, the heater is wound on a core whose conductivity is much larger than that of the insulation used in the body of the furnace, and if the conductivity of the charge is not negligible, it frequently happens that the effective conductivity of the central tube and charge is several times that of the insulation. Given such a case one would expect to be able to calculate the central temperature distribution by a method analogous to one employed for a rod cooling in air. In fact this type of calculation gives remarkably good agreement with experimental results for furnaces with uniformly wound heaters if not more than 10% of the heat loss of the furnace proper occurs through the top and bottom ends.

Figure 7 shows lines obtained from the electrical analogue correlating sets of ratios r_b/r_a and L/r_a for which the end losses of the furnace proper are equal to 10% of the total loss. There are three lines given, for different values of L_H/L . These lines apply for the end condition $K_p/h_vL = 0$. $K_p/h_vL = \infty$ gives of course no end losses, and the end losses for intermediate K_p/h_vL will be somewhere between these two limits. All furnaces with uniformly wound heaters whose parameters are such as to give points on or to the left of the

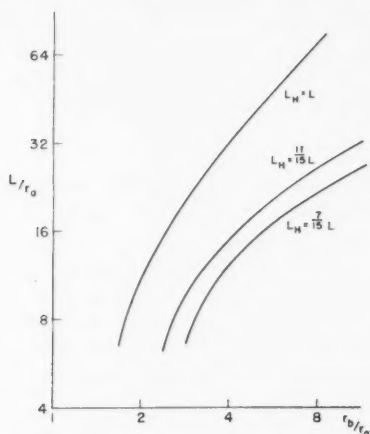


FIG. 7. Lines correlating sets of ratios of r_b/r_a and L/r_a for which the end heat losses of the furnace proper equal 10% of the total heat loss.

corresponding 10% line have, therefore, end losses less than 10% of the total loss, and their central temperature distributions can be obtained from the following equations:

$$(4) \quad T = T_0 \left[1 - \frac{\cosh cx - 1}{e^{(cL_H/2)} - 1} \right], \quad 0 \leq x \leq L_H/2$$

$$T = \frac{T_0 \sinh cL_H/2}{e^{(cL_H/2)} - 1} e^{-c(x-L_H/2)}, \quad L_H/2 \leq x \leq L/2$$

where

$$c = \frac{1}{r_a} \sqrt{\frac{2}{\ln(r_b/r_a)} \frac{K_p}{K_E}},$$

T is the temperature at point x ,

T_0 is the temperature at $x = 0$,

and x is the distance along the central tube with the origin at the center of the furnace.

The rest of the symbols are as previously defined. The power required to raise the furnace to the temperature T_0 is given by

$$(5) \quad Q = \frac{2\pi K_p L_H}{\ln(r_b/r_a)} \times \frac{T_0}{1 - e^{-cL_H/2}}.$$

3.2 Comparison with Experiment

Two furnaces were constructed to check eqs. 4 and 5, one with parameters $r_b/r_a = 2$, $L/r_a = 26$, $L_H/L = 11/15$, of length 40 cm, and the other with $r_b/r_a = 4$, $L/r_a = 16$, $L_H/L = 11/15$ and of length 20 cm. Both had an

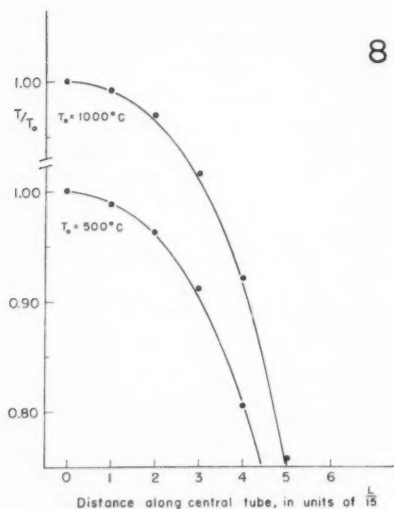


FIG. 8. Temperature distributions for a furnace with parameters $r_b/r_a = 4$, $L/r_a = 16$, $L_H/L = 11/15$ and a uniformly wound heater.

Dots, observed distribution; lines, calculated distribution.

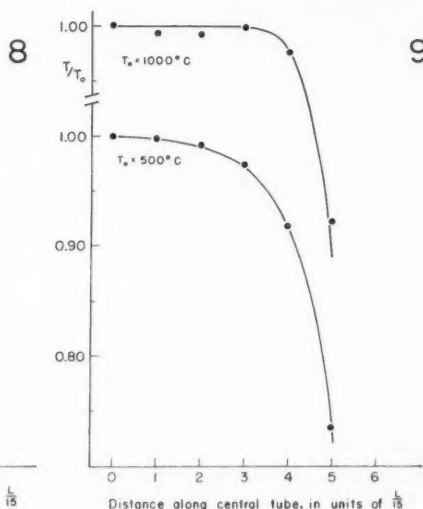


FIG. 9. Temperature distributions for a furnace with parameters $r_b/r_a = 2$, $L/r_a = 26$, $L_H/L = 11/15$ and a uniformly wound heater.

Dots, observed distribution; lines, calculated distribution.

effective conductivity of tube and charge about ten times that of the insulation. Figures 8 and 9 show the experimental and calculated temperature distribution while Table V compares the observed and calculated power

TABLE V
Observed and calculated power inputs for furnaces with uniformly wound heaters

Furnace parameters			Central temp. T_0 , °C	Power input, watts	
r_b/r_a	L/r_a	L_H/L		Calculated	Observed
4	16	11/15	500	111	100
4	16	11/15	1000	278	273
2	26	11/15	500	430	430
2	26	11/15	1000	1318	1321

inputs required to obtain a given central temperature T_0 . The agreement between the calculated and observed values is certainly remarkable, considering the approximations involved in eqs. 4 and 5. Both these equations were derived not only under the assumption of purely radial heat flow, but also under the further assumption that K_p and K_E are temperature independent. There is no simple way in which these equations can be generalized to include temperature-dependent conductivities, and in the calculation done for the comparison shown above average values were used for both K_p and K_E , calculated by means of the formula

$$K_{Av} = \frac{1}{T_0} \int_0^{T_0} K(T) dT.$$

It should be pointed out that the agreement between calculated and observed temperature distributions is not as good towards the ends of the furnace as it is in the central regions illustrated in Figs. 8 and 9. In the region of $x = 0.9L$ to $x = L$ the calculated temperatures differed by 20° C to 50° C from the observed ones. However, this region of the furnace is of little importance, and so no effort was made to pin down this discrepancy.

4. SUMMARY

Design data were presented in tabular form which permit the construction of short cylindrical furnaces with extended gradientless regions. These regions, where the temperature varies by less than 0.5%, extend over half the length of the heater and are roughly five times longer than in equivalent furnaces with uniformly wound heaters.

Formulae are also given to calculate the temperature distribution and power requirements of conventional furnaces with uniformly wound heaters. These formulae are not universally applicable and their limits of validity are specified.

REFERENCES

- CARSLAW, H. S. and JAEGER, J. C. 1959. Conduction of heat in solids (Oxford Clarendon Press), p. 10.
KINGERY, W. D., FRANCL, J., COBLE, R. L., and VASILOS, T. 1954. J. Am. Ceram. Soc. **37**, 107.
LAUBITZ, M. J. 1959. Can. J. Phys. **37**, 798.

THE DECAY OF Bi^{208} ¹

C. H. MILLAR, T. A. EASTWOOD, AND J. C. ROY

ABSTRACT

It has been observed that Bi^{208} decays mainly by K - and L -electron capture to the 2.615-Mev first-excited level of Pb^{208} . Decay to known Pb^{208} levels above the 2.615-Mev level has been shown experimentally not to occur in more than 3% of the Bi^{208} disintegrations, in agreement with an analysis of the mass differences in this region which indicates that such decay modes are energetically impossible. Positrons are not emitted in more than 5% of Bi^{208} disintegrations. The value of the ratio of K X-rays to 2.615-Mev γ -rays has been measured to be 0.23 ± 0.01 . Assuming that the ground state of Bi^{208} is 5^+ and that the theory of Brysk and Rose is accurate in the region near the K -capture threshold, this ratio measurement leads to a value of 2.807 Mev for the total decay energy of Bi^{208} . This agrees with the value 2.75 ± 0.10 Mev obtained from reaction cycle analysis. New measurements of the Bi^{208} half-life have revealed an error in the previous measurement, the best value now being 7.5×10^5 years to within a factor of three. Incidental to the main experiment an upper limit of 0.5% has been measured for the positron decay of Bi^{207} .

INTRODUCTION

In an earlier paper (Roy *et al.* 1958) evidence was presented for the production of long-lived Bi^{208} by the fast neutron reaction $\text{Bi}^{209}(n, 2n)\text{Bi}^{208}$. It was detected by observing the 2.6-Mev γ -ray which follows its decay to the first-excited state of Pb^{208} . Figure 1 shows the level scheme of Pb^{208} as derived

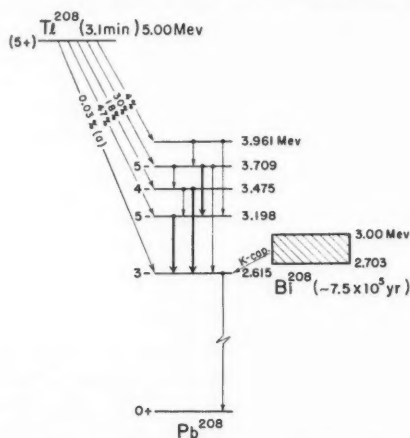


FIG. 1. Level scheme of Pb^{208} showing known decay of Tl^{208} and decay of Bi^{208} as observed in this experiment. γ -Ray transitions shown by heavy lines are those searched for in coincidence with 2.615-Mev γ -ray. Relative intensity (a) is from unpublished work of Elliott and Wolfson.

¹Manuscript received July 7, 1959.

Contribution from the Physics Division and Chemistry and Metallurgy Division, Atomic Energy of Canada Limited, Chalk River, Ontario.

Issued as A.E.C.L. No. 870.

from studies of the decay of Tl^{208} (cf. Strominger *et al.* 1958) and includes data on Bi^{208} both from the work of Roy *et al.* (1958) and the present work. The investigation described in this paper was undertaken to extend the previous work, since an accurate knowledge of the properties of Bi^{208} could provide a useful "key" for resolving the mass difference discrepancies that still exist in the Pb-Bi region.

EXPERIMENTAL

(a) Coincidence Spectrometer

From Fig. 1 it is clear that in the decay of Bi^{208} there should be Pb X-rays in coincidence with the 2.615-Mev γ -ray of Pb^{208} and, if sufficient energy is available, there might also be coincident γ -rays arising from decay through the higher-energy levels of Pb^{208} .

The coincidence γ -ray spectrometer shown diagrammatically in Fig. 2 was used to investigate these possibilities, though in some experiments a 1½-in. diameter \times ¼-in. thick crystal replaced the 2-in. \times 2-in. crystal. This smaller

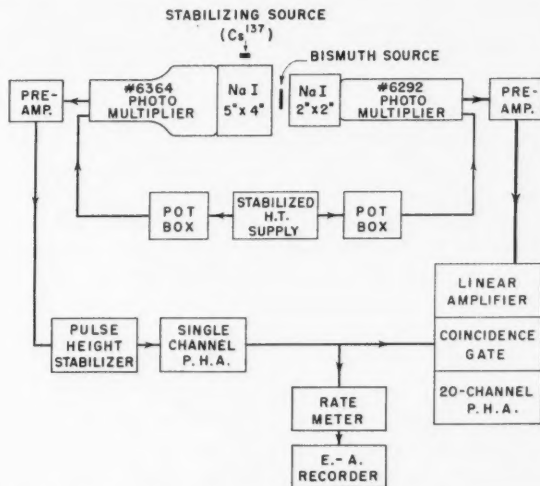


FIG. 2. Schematic diagram of coincidence crystal spectrometer used.

crystal was "black" to both K and L X-rays and the geometric efficiency was computed to be 49% for a thin source placed close to the crystal face. The detectors were enclosed in about 4 inches of lead shielding and a similar thickness of lead shielded the small crystal from the Cs^{137} stabilizing source. The spectrum from the smaller NaI(Tl) crystal was analyzed by the 20-channel pulse height analyzer which was gated by coincident 2.615-Mev γ -ray pulses selected from the spectrum of the larger crystal.

The various electronic components were conventional except for the pulse height stabilizer of which a general description is given by Graham *et al.*

(1958, p. 1086). This stabilizer acted to maintain a constant pulse height for the 662-keV photopeak from the Cs^{137} source, and was necessary since, with the weak Bi^{208} sources available, long counting periods were required and the large crystal counter had, of itself, inadequate long-term stability.

Sources of Am^{241} , Na^{22} , and Cs^{137} were used to calibrate the energy scale of the smaller crystal spectrometer. Furthermore our bismuth source contained about ten times as much Bi^{207} as Bi^{208} activity produced by an $(n, 3n)$ reaction (Eastwood and Roy 1959). Since Bi^{207} also decays by electron capture it served as a calibration source of Pb K and L X-rays. A source of Tl^{208} in equilibrium with a long-lived precursor Th^{228} was used to set the 5-in. \times 4-in. crystal spectrometer on the 2.615-MeV γ -ray photopeak.

(b) Positron Detector

The standard technique of detecting positrons by counting coincidences of annihilation quanta in two counters placed at 180° to the positron absorber was used. The apparatus is shown schematically in Fig. 3. The source was

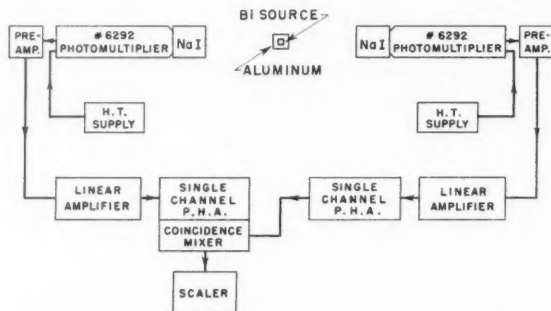


FIG. 3. Schematic diagram of positron-detecting apparatus used.

surrounded by enough aluminum to absorb 2.1-MeV positrons and the whole detector setup was enclosed by about 4 inches of lead shielding. The single-channel pulse height analyzers on the two photomultiplier outputs were set to accept only the photopeak from 511-keV annihilation radiation. The efficiency for detection of annihilation radiation quanta was about 10^{-3} whereas the efficiency for random coincidences was 10^{-6} . The absolute efficiency for counting positrons was obtained by means of a standardized Na^{22} source. The total chance and background coincidence rate was determined by displacing the source from the axis of the two detectors.

(c) Bi^{208} Sources

The method used to prepare radiochemically pure bismuth in metallic form has been described previously (Roy *et al.* 1958). For our study of the γ - and X-ray spectrum of Bi^{208} with the coincidence spectrometer a thin source was required in order to minimize self-absorption effects. The bismuth metal powder (120 mg) was therefore spread uniformly over an area of 7.9 cm^2 and

sandwiched between two films of Scotch tape. The superficial thickness of the bismuth was 15.2 mg per cm^2 but because the metal was in powder form the effective thickness was greater than this. The thickness of the Scotch tape was 8.5 mg per cm^2 . The Bi^{208} disintegration rate was obtained from the counting rate of 2.615-Mev γ -rays in a NaI(Tl) crystal γ -ray spectrometer of known efficiency (Eastwood and Roy 1959). Assuming that all disintegrations give a γ -ray of this energy, this rate was 7 disintegrations per second. The source also contained about 60 disintegrations per second of Bi^{207} , and about 40 γ -ray quanta per second (either 270 or 310 kev) from 2.6×10^6 -year Bi^{210} (Golenetskiĭ *et al.* 1958).

The source used to search for possible positron branching consisted of 100 mg of the same bismuth metal powder enclosed in a cylindrical polythene capsule with walls $1/32$ in. thick, which, in turn, was placed in an aluminum holder with walls of sufficient thickness ($5/32$ in. or 1100 mg per cm^2) to absorb 2.1-Mev positrons.

RESULTS

(a) Search for K and L X-Rays

Using the coincidence spectrometer described in the preceding section it was found that both K and L X-rays of lead are in coincidence with the 2.615-Mev γ -ray of Pb^{208} . Typical spectra are shown in Figs. 4 and 5.

Several checks were carried out to confirm that the observed X- and γ -rays did in fact originate from the decay of Bi^{208} . Despite the fact that the K and L X-rays from the Bi^{207} in the source were about ten times as intense as those from the Bi^{208} , the total source activity was so low that chance coincidences of these X-rays with the 2.615-Mev γ -ray were negligible, amounting to 0.5% and 0.1% for the L and K X-ray peaks respectively. Chance coincidences with the similar number of higher-energy γ -rays from Bi^{210} would be expected to be at least an order of magnitude less than these.

A separate experiment was carried out to show that these coincident X-rays arose from the decay of Bi^{208} and not from lead atoms of the shielding which had been ionized in the K -shell by a γ -ray or background particle which at the same time deposited sufficient energy in the large crystal to open the electronic gate. For this experiment the Bi^{208} source was enclosed in a cadmium container $\frac{1}{4}$ in. thick which was sufficient to attenuate the K X-rays of lead by a factor of about 1000, and it was found that the coincidence K X-ray counting rate was reduced to a flat distribution of about twice background intensity. It was therefore concluded that the great majority of the coincident K X-rays originated in the source.

As mentioned previously (Roy *et al.* 1958) no γ -rays from the known higher excited states of Pb^{208} were found in coincidence with the 2.615-Mev γ -ray (to an accuracy of $\sim 3\%$). This not only ruled out Tl^{208} contamination as the source of these high-energy γ -rays, but also showed that, to the same accuracy, no Bi^{208} decay to these higher states takes place. This gives some confirmation to the estimate from reaction cycle analysis that such modes of decay are energetically impossible (see Discussion below).

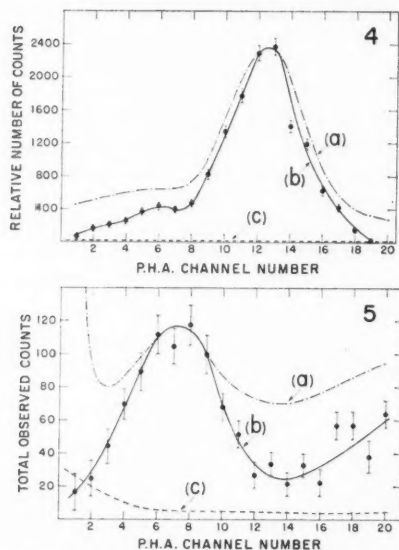


FIG. 4. Spectrum of K X-rays of lead attributed to Bi^{208} decay observed in 2-in. diameter $\times 2$ -in. $\text{NaI}(\text{Tl})$ crystal. Curves show:

(a) Pb K X-ray calibration peak obtained from Bi^{207} activity in source. Curve is normalized to curve (b) at peak.

(b) Observed points and fitted curve for high-energy X-rays counted in coincidence with 2.615-Mev γ -rays. Background has been subtracted and curve normalized to equal counting time with curve (b) Fig. 5.

(c) Coincidence background for curve (b).

(Zero on abscissa does not correspond to zero pulse height.)

FIG. 5. Spectrum of L X-rays of lead attributed to Bi^{208} decay observed in $1\frac{1}{2}$ -in. diameter $\times \frac{1}{2}$ -in. $\text{NaI}(\text{Tl})$ crystal. Curves show:

(a) Pb L X-ray calibration peak obtained from Bi^{207} activity in source. Background has been subtracted and curve normalized to curve (b) at peak.

(b) Observed points and fitted curve for low-energy X-rays counted in coincidence with 2.615-Mev γ -rays. Background has been subtracted.

(c) Coincidence background for curve (b).

(Zero on abscissa does not correspond to zero pulse height.)

(b) Search for Positron Decay

No positron decay in our Bi^{208} source could be detected. From the counting statistics at the 99% confidence level it was concluded that less than 5% positron branching occurred in the decay of Bi^{208} . Since the source contained about ten times as much Bi^{207} as Bi^{208} activity an upper limit to positron branching in the decay of Bi^{207} was set at 0.5% by this same experiment.

(c) Measurement of Ratio of K X-Rays to 2.615-Mev γ -Rays

An attempt was made to measure directly the K/L electron capture ratio in order to estimate the decay energy from electron capture theory. However, self-absorption of L X-rays in the source and to a lesser extent absorption in the source-covering and detector window introduced rather uncertain corrections of several hundred per cent so these results were without significance.

Fortunately a measure of the $K/(L+M+\dots)$ electron capture ratio can provide essentially the same information about the nucleus as does the K/L capture ratio. If it is assumed that all Bi^{208} decays occur via the 2.615-Mev level of Pb^{208} —which seems reasonable in the light of the above observations—the ratio of K X-rays to 2.615-Mev γ -rays will lead directly to a value for the $K/(L+M+\dots)$ electron capture ratio. Using the crystal spectrometer shown in Fig. 1 (with a $1\frac{1}{2}\text{-in.} \times \frac{1}{4}\text{-in.}$ crystal) we measured the ratio of K X-rays to 2.615-Mev γ -rays to be 0.23 ± 0.01 . (The necessary corrections for counter geometry, self-absorption in the source, absorption in the crystal covering, crystal efficiency, and scattering from the lead-shielding walls have been included in this value.)

An accurate value of 0.957 for the K -fluorescence yield of bismuth has been determined by Mladjenovic and Slätis (1955), who measured the Auger electron yield. Combining this with our measured ratio leads to a value of $K/(L+M+\dots) = 0.316 \pm 0.014$.

(d) *Measurement of Half-Life*

Absolute intensity measurements have been carried out on three different samples of Bi^{208} produced in separate pile irradiations of Bi^{209} . These three measurements were mutually consistent, but differed by about a factor of ten from the previous results (Roy *et al.* 1958), and a check showed that a calibration error had, indeed, been made in the previous work. The cross section for the $\text{Bi}^{209}(n, 2n)\text{Bi}^{208}$ reaction in a reactor has been re-estimated on the basis of further work on other elements (Eastwood and Roy 1959), and this new value also differs slightly from that used previously. As a result of these two changes it is now estimated that the half-life of Bi^{208} is 7.5×10^5 years to within an error of about a factor of three.

DISCUSSION

From these experiments it was concluded that Bi^{208} decays mainly by K - and L -electron capture to the first-excited state of Pb^{208} at 2.615 Mev. The energy difference between Bi^{208} and Pb^{208} is therefore greater than 2.703 Mev (i.e. 2.615 + the binding energy of a K -electron in Bi).

A value for the exact energy difference may be obtained from electron capture theory since the $K/(L+M+\dots)$ ratio indicates that the energy available for K -capture is not very much larger than the K -electron binding energy in which case this ratio gives a very sensitive measure of the decay energy (cf. Brysk and Rose 1958, Fig. 6). The theory requires a knowledge of the type of electron capture transition which in turn may be derived from a knowledge of the spins and parities of the initial and final nuclear states involved in the transition. The 2.615-Mev state of Pb^{208} has been shown experimentally to be a 3^- state (Elliott *et al.* 1954). From shell model theory, which is well confirmed for this particular region (Elliott and Lane 1957), it would appear that the ground state characteristics of $_{83}\text{Bi}^{208}$ will be the sum of the spins of the extra $h_{9/2}$ proton outside the 82-proton closed shell, and the $p_{1/2}$ neutron hole in the incomplete 126-neutron shell. Thus the ground state of Bi^{208} will

be expected to be a 4^+ or 5^+ state and on the basis of Nordheim's rules (Nordheim 1951, and also theoretical confirmation by de-Shalit 1953) it is most probable that the higher spin state is the correct choice.

If we assume that the Bi^{208} ground state is 5^+ , the electron capture decay to the 3^- first-excited state of Pb^{208} is then a first-forbidden unique transition ($\Delta J = 2$, yes) and the theory of Brysk and Rose (1958) may be used to obtain a relation between the decay energy and the ratio of K/L capture that is completely determinate and is independent of the form of interaction or the degree of parity conservation. In the notation of Brysk and Rose this expression is

$$(1) \quad K/L = \frac{q\kappa^4 g\kappa^2}{qL_1^4 gL_1^2 + qL_{II}^4 fL_{II}^2 + (9/R^2)qL_{III}^2 gL_{III}^2}.$$

In order to obtain the expression for the $K/(L+M+\dots)$ ratio for comparison with our observations it is necessary to increase the magnitudes of terms in the denominator of the above expression by factors (defined here as " r_I ", " r_{II} ", \dots), which take into account capture from the outer electron shells. These factors may be obtained to a good approximation by comparing the probability density at the origin of a hydrogen-like wave function for the M , N , O , and P electrons with that for L electrons, using Slater screening parameters to take into account the screening by the inner electrons. The expression for this factor is spin dependent so that separate relations are obtained for the L_I and the L_{II} (or L_{III}) terms as follows:

$$(2) \quad r_I \equiv \frac{L_I + M_I + \dots}{L_I} = 2^3 \sum_{n=2,3,\dots} \frac{1}{n^3} \left(\frac{Z-Z_n}{Z-Z_2} \right)^3 \\ = 1.272 \quad (Z = 83) \quad (\text{cf. Wapstra } et al. 1959, \text{ p. 61}),$$

$$(3) \quad r_{II} \equiv \frac{L_{II} + M_{II} + \dots}{L_{II}} = \frac{2^5}{3} \sum_{n=2,3,\dots} \frac{(n^2-1)}{n^5} \left(\frac{Z-Z_n}{Z-Z_2} \right) \\ = 1.247 \quad (Z = 83),$$

$$(4) \quad \left(r_{III} \equiv \frac{L_{III} + M_{III} + \dots}{L_{III}} \equiv r_{II} \right).$$

Here " n " is the total quantum number and " Z_n " is the Slater screening parameter (see, for example, Wapstra *et al.* 1959, p. 88). Thus for bismuth we obtain the expression

$$(5) \quad \frac{K}{L+M+N\dots} = \frac{q\kappa^4 g\kappa^2}{1.272qL_1^4 gL_1^2 + 1.247(qL_{II}^4 fL_{II}^2 + [9/R^2]qL_{III}^2 gL_{III}^2)}$$

in which the left-hand side is experimentally observed, the " f " and " g " values are given by Brysk and Rose (1958), and the several " q " values that appear may all be expressed as linear functions of any one of them by making use of the known electron binding energy differences for the various shells. Solving this quartic equation for " $q\kappa$ ", the neutrino energy in K -capture, we may

then obtain the energy available for the decay of Bi²⁰⁸ to the 2.615-Mev level of Pb²⁰⁸ and this is found to be 192 ± 3 kev. The error quoted is based solely on the statistics of the experiment; however, taking into account the plotting and reading errors in obtaining the "f" and "g" values from the Brysk and Rose curves increases the uncertainty to only ± 4 kev. Adding this value to the accurately known energy of the Pb²⁰⁸ first-excited state we obtain the value 2.807 for the total decay energy of Bi²⁰⁸.

It should be noted that this value for the Bi²⁰⁸ decay energy is not a direct measurement but is based on the assumptions (a) that the ground state of Bi²⁰⁸ is a 5⁺ state, and (b) that the Brysk and Rose theory is valid to this degree of precision in the energy region where the K/L ratio is changing rapidly. Since, to the authors' knowledge, there has been no experimental confirmation that the theory is, indeed, this accurate it would be unwarranted to claim to have measured the Bi²⁰⁸ decay energy to the precision implied by the calculations, even assuming that the spin assignment is correct. And, on the other hand, if the ground state of Bi²⁰⁸ is a 4⁺ state, the decay is a first-forbidden transition in which case coupling constants and nuclear matrix elements appear in the relationship corresponding to equation (5) above, and the known values of these quantities are not sufficiently accurate that any very useful information may be derived from the measurement of the $K/(L+M+\dots)$ capture ratio.

It is of interest to check whether the 5⁺ spin assignment and the decay energy which we have derived therefrom lead to a "log ft " value consistent with values found for other first-forbidden unique transitions. For unique transitions it is customary to include the shape factor (which is quite accurately known) with the "f" value to give an " f_n " value (where "n" is the degree of forbiddenness of the transition) (Wu 1955), since it is found that for these transitions the "log $f_n t$ " values form a closer grouping than do the "log ft " values. For first-forbidden unique electron-capture transitions it may be shown² that

$$(6) \quad f_1 = \frac{1}{12} \times \frac{\pi}{2} \left[q_K^4 g_K^2 + r_1 q_L^4 g_L^2 + r_{II} (q_{LII}^4 f_{LII}^2 + \frac{9}{R^2} q_{LII}^2 g_{LII}^2) \right].$$

The lifetime of Bi²⁰⁸ as reassessed in this paper is about 7.5×10^8 years and it is estimated that this is accurate to within a factor of three. This gives a value of 11.0 ± 0.5 for "log $f_1 t$ (Bi²⁰⁸)", which is somewhat higher than the range of values of 8 to 9 which is found for most known first-forbidden unique β -decay transitions (Wu 1955). On the other hand, the "log $f_1 t$ " values for the three other known first-forbidden unique K -capturing nuclides do not exhibit quite as good consistency as do the β -emitters. This is shown in Table I below in which our value for Bi²⁰⁸ has been included for comparison. Most of the data for this table were obtained from the compilation of Robinson and Fink (1955); however the "log $f_1 t$ " values were computed from equation (5)

²We are indebted to Dr. G. E. Lee-Whiting for deriving this relationship as well as for many other valuable discussions and much assistance with the theoretical interpretation of our results.

TABLE I
Properties of nuclei that decay by first-forbidden unique K -capture

Nucleus	Decay energy	Half-life, years	% electron capture	$\log_{10} f_1 t$
K^{40}	$60 \pm 8^*$	1.3×10^9	11	11.0
Ca^{41}	440 ± 20	$\sim 1.2 \times 10^5$	100	9.6
Tl^{204}	335 ± 10	4.0	2.5	8.4
Bi^{208}	(193 ± 4)	$\sim 7.5 \times 10^5$	100	11.0

*Holland and Lynch (1959). These authors note that this energy value for K^{40} is inconsistent with that derived from the ratio of L -capture to K -capture on the basis of the Brysk and Rose theory, and cite some evidence that the decay of K^{40} may not be a first-forbidden unique transition.

above and in most cases the uncertainty in the " $\log f_1 t$ " value is of the order of 0.5. From these comparisons we conclude that while our " $\log f_1 t$ " value for Bi^{208} does not fall within the range normally found for first-forbidden unique β -emitters, it is not inconsistent with the apparent wider spread of values found for the few cases of first-forbidden unique K -capture that have been observed. It is of interest to note that for the first-forbidden unique β -decay of Tl^{208} to the 2.615-Mev state of Pb^{208} the " $\log f_1 t$ " value is 9.4 which is also somewhat above the usual range.

The decay energy of Bi^{208} may also be obtained, in principle, from the reaction cycle shown in Fig. 6.

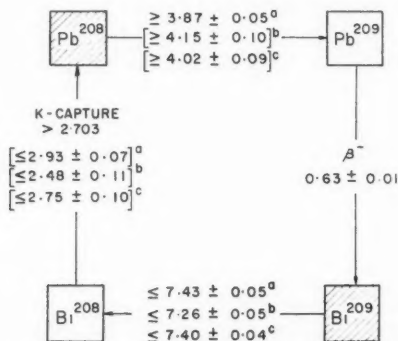


FIG. 6. Diagram showing reaction cycle used in determining expected decay energy of Bi^{208} .

(a) Values obtained from charged particle reactions.

(b) Values obtained assuming $E_n(Cu^{63}) = 10.65 \pm 0.06$ Mev.

(c) Values obtained assuming $E_n(Cu^{63}) = 10.826 \pm 0.020$ Mev.

All energies are in million electron volts. Values in parentheses are derived from reaction cycle analysis (see text).

Unfortunately some uncertainty exists as to the neutron-binding energies of Bi^{209} and Pb^{209} , and it is of value to consider two different methods that may be used to obtain these energies. The first method relies on charged particle experiments which give the limiting values labelled (a) in Fig. 6 (Harvey 1951, 1953). From these an upper limit of 2.93 ± 0.07 Mev may be

derived for the decay energy of Bi^{208} , though the true value may be less than this limit if a charged particle group corresponding to a weak ground state interaction has been missed in Harvey's work. This analysis enables one to set a reasonably reliable upper limit of 3.00 Mev for the decay energy which indicates that the decay of Bi^{208} via the second or higher excited levels of Pb^{208} is energetically forbidden (see Fig. 1), as was confirmed by our observations.

The second method of determining the Bi^{209} and Pb^{209} neutron-binding energies makes use of photoneutron threshold energies which, unfortunately, are usually measured relative to the Cu^{63} photoneutron threshold rather than absolutely. Thus it is necessary to examine the accuracy of the Cu^{63} value in order to assess the accuracy of other related photoneutron threshold measurements.

The most recently derived "best value" for the Cu^{63} photoneutron threshold energy is 10.65 ± 0.06 Mev (Van Patter and Whaling 1957), but we find that the use of neutron-binding energies based on this value leads to an inconsistency in the reaction cycle of Fig. 6. The binding energies labelled (b) in Fig. 6 are expressed relative to 10.65 Mev for Cu^{63} , the value 7.26 ± 0.05 Mev for Bi^{209} having been obtained from direct measurements (Van Patter and Whaling 1954³), and the value 4.15 ± 0.10 Mev for Pb^{209} having been derived from two independent reaction cycle analyses (Hincks and Millar 1958³). These values lead to a value of 2.48 ± 0.11 Mev for the total decay energy of Bi^{208} , and this differs from our observed lower limit of 2.703 Mev by twice the standard deviation.

On the other hand, the most recent value for the Cu^{63} neutron-binding energy obtained by mass spectrometric methods is 10.826 ± 0.020 Mev (Quisenberry *et al.* 1956). The Bi^{209} neutron-binding energy labelled (c) in Fig. 6 is based on this value (Chidley *et al.* 1958), and the corresponding value for Pb^{209} is derived as previously using this value. These lead to a Bi^{208} disintegration energy of 2.75 ± 0.10 Mev which is in agreement with the lower limit set by our observation of K X-rays, with the value obtained from the Brysk and Rose theory, and with the upper limit set by Harvey's work. It would therefore appear that the mass spectrometric value for the Cu^{63} neutron-binding energy must be accepted rather than the value derived from betatron and synchrotron experiments if we are to obtain an energy balance in this reaction cycle that is consistent with our observations.

SUMMARY

To summarize, the only observed decay mode of Bi^{208} is by K - and L -electron capture to the first-excited state of Pb^{208} , no positron emission having been detected (to an accuracy of 5%), nor electron capture to higher excited states of Pb^{208} (to an accuracy of 3%). The half-life of Bi^{208} has been re-measured to be 7.5×10^5 years to within a factor of three. We conclude that the decay energy of Bi^{208} lies between 2.703 and 3.00 Mev, and what appears

³Note that some adjustments to the original values have been made to take into account the Cu^{63} threshold value used here.

to be the most reliable reaction cycle analysis indicates a value of 2.75 ± 0.10 Mev. This agrees with the value 2.807 derived from theory on the basis of an assumed 5^+ Bi^{208} ground state from the value of 0.23 ± 0.01 observed for the ratio of K X-rays to 2.615-Mev γ -rays. Figure 1 shows these conclusions diagrammatically.

As a by-product of this study an upper limit of 0.5% has been set for the occurrence of positron decay in Bi^{207} .

ACKNOWLEDGMENTS

The authors acknowledge with gratitude their indebtedness to R. L. Graham, who assisted with preliminary measurements, to P. J. Campion, who supplied the standard Na^{22} source, to R. L. Graham, G. T. Ewan, and G. E. Lee-Whiting for many useful discussions, and to A. S. C. Hyde for technical assistance.

REFERENCES

- BRYSK, H. and ROSE, M. E. 1958. *Revs. Modern Phys.* **30**, 1169.
 CHIDLEY, B. G., KATZ, L., and KOWALSKI, S. 1958. *Can. J. Phys.* **36**, 407.
 DE-SHALIT, A. 1953. *Phys. Rev.* **91**, 1479.
 EASTWOOD, T. A. and ROY, J. C. 1959. *Can. J. Phys.* **37**, 815.
 ELLIOTT, J. P. and LANE, A. M. 1957. *In Handbuch der Physik*, Vol. 31, *edited by* S. Flügge (Springer-Verlag, Berlin).
 ELLIOTT, L. G., GRAHAM, R. L., WALKER, J., and WOLFSON, J. L. 1954. *Phys. Rev.* **93**, 356.
 ELLIOTT, L. G. and WOLFSON, J. L. Unpublished.
 GOLENETSKIĬ, S. V., RUSINOV, L. I., and FILIMONOV, Y. I. 1958. *J. Exptl. Theoret. Phys. U.S.S.R.* **35**, 1313.
 GRAHAM, R. L., GEIGER, J. S., and EASTWOOD, T. A. 1958. *Can. J. Phys.* **36**, 1084.
 HARVEY, J. A. 1951. *Phys. Rev.* **81**, 353.
 ——— 1953. *Can. J. Phys.* **31**, 278.
 HINCKS, E. P. and MILLAR, C. H. 1958. *Can. J. Phys.* **36**, 231.
 HOLLAND, R. E. and LYNCH, F. J. 1959. *Phys. Rev.* **113**, 903.
 MLADJENOVIC, M. and SLÄTIS, H. 1955. *Arkiv Fysik*, **9**, 41.
 NORDHEIM, L. W. 1951. *Revs. Modern Phys.* **23**, 322.
 QUISENBERRY, K. S., SCOLMAN, T. T., and NIER, A. O. 1956. *Phys. Rev.* **104**, 461.
 ROY, J. C., EASTWOOD, T. A., and HAWKINGS, R. C. 1958. *Can. J. Phys.* **36**, 18.
 STROMINGER, D. and HOLLANDER, J. M. 1958. *University of California Radiation Laboratory Report UCRL-8289*.
 VAN PATTTER, D. M. and WHALING, W. 1954. *Revs. Modern Phys.* **26**, 402.
 ——— 1957. *Revs. Modern Phys.* **29**, 757.
 WAPSTRA, A. H., NIJGH, G. J., and VAN LIESHOUT, R. 1959. *Nuclear spectroscopy tables* (North-Holland Publishing Co., Amsterdam).
 WU, C. S. 1955. *In Beta- and gamma-ray spectroscopy*, *edited by* K. Siegbahn (North-Holland Publishing Co., Amsterdam), p. 314.
 ROBINSON, B. L. and FINK, R. W. 1955. *Revs. Modern Phys.* **27**, 424.

RADIO STAR SCINTILLATIONS AND IONOSPHERIC DISTURBANCES¹

T. R. HARTZ

ABSTRACT

The generation mechanism for the ionization irregularities in the upper atmosphere which are responsible for radio star scintillations is considered. The general belief that scintillations are related to the spread- F phenomenon observed on ionosonde recordings is found to be an inadequate explanation for the scintillations at 53 Mc/s recorded at Ottawa. An examination of the Ottawa recordings shows that there is a definite association, both in time of occurrence and geographical location, with those ionospheric disturbances that are usually considered to be due to incoming solar particles. Since other workers at more southerly geomagnetic latitudes have associated their scintillation observations with the spread- F phenomenon which they consider to be independent of auroral activity, it would appear that two mechanisms, at least, are responsible for the radio star fluctuations: namely, the precipitation of solar corpuscles and a mechanism linked with the spread- F phenomenon. The former seems to predominate at high latitudes, the latter is probably predominant at low latitudes, while both mechanisms probably are operative in middle latitudes.

INTRODUCTION

Radio star scintillations have been studied for some years, but, while they are known to result from irregularities of ionization in the upper atmosphere, little agreement has been reached on the origin of the irregularities. Some authors favor an explanation involving the F region and the phenomenon known as spread F (Dagg 1957a), others would place the irregularities in the E region and link them to the sporadic- E phenomenon (Bolton, Slee, and Stanley 1953). In neither case, however, is the generation mechanism for the irregular structures understood fully.

Several recent papers on the subject seek to locate the mechanism for the production of the ionospheric irregularities within the terrestrial atmosphere. Booker (1958) argues in favor of atmospheric turbulence at a height between the E and F regions. However, he fails to account for the observed nighttime maximum of scintillation as a daytime maximum should fit the turbulence model much better. Dagg (1957c, d) reviews a number of existing theories, pointing out their shortcomings, and develops a suggestion that scintillation-producing F -region irregularities are transferred there from the dynamo region where they arise through turbulent winds. Neither of these hypotheses seems entirely satisfactory since no adequate explanation is presented for the known dependence of scintillation on ionospheric disturbances at high latitudes.

Dagg actually raises an interesting point when he considers the F -region irregularities that have been observed by Peterson *et al.* (1955). While such irregularities may well explain the high-latitude scintillations, Dagg feels they cannot explain scintillations observed in equatorial regions, and so he discards

¹Manuscript received May 1, 1959.

Contribution from the Radio Physics Laboratory, Defence Research Telecommunications Establishment, Defence Research Board, Ottawa, Canada. The work was performed under project PCC No. D48-95-11-30.

the idea. This action seems too drastic since no one has yet satisfactorily examined the possibility that more than one mechanism is responsible for scintillations. If the latter were the case, one might not expect much similarity between the results for high and low latitudes. Indeed, the hypothesis that two separate processes are involved would seem to account for most of the observed behavior of scintillations and, should one of the processes involve the phenomenon known as spread F , would also account for the apparent close connection with irregular ionization structures in the F region, under certain conditions. Koster (1958) has already pointed out the differences which exist between scintillations observed at an equatorial station and those observed at higher latitudes. If there is a link between F -region irregularities and scintillations one would expect that spread- F conditions at low and high latitudes would be dissimilar, and such has been shown to be the case since spread F correlates positively with magnetic activity at high latitudes, and negatively at low latitudes (Lyon, Skinner, and Wright 1958). Consequently it would seem worth while to examine the possibility that scintillations at high latitudes are primarily due to incoming particles which produce disturbed ionosphere conditions, while those in equatorial regions are primarily due to some other mechanism, possibly one that is contained entirely within the ionosphere. Under such circumstances it would seem highly likely that scintillations at temperate latitudes would be due to a combination of the two effects. (An inherent requirement of this thesis is that low-latitude spread F is not produced by the precipitating solar particles, which is consistent with the observations of Lyon, Skinner, and Wright (1958).)

The phenomenon of spread F which is observed on ionosonde recordings implies irregularities in the F -region ionization. Since this condition is a common one, it is not at all unreasonable to expect that radio waves that arrive from outside the ionosphere would be scattered by such F -region irregularities. Briggs (1958a) has recently been able to show detailed correlation between spread- F conditions and scintillations for the ionosphere in the same geographical region, which should remove some doubts on the matter. However, the lack of perfect correlation in his data leads one to suspect that he has not yet provided the complete answer, and perhaps a combination of circumstances would have resulted in a better explanation. Briggs suggested that the scintillation data he was considering were not of the type which conceivably could be linked with auroral activity, but his proviso seems based on nothing more than that positive correlation with spread- F echoes was found and that the scintillations were a nighttime phenomenon. This does not seem, of itself, an adequate basis for the selection of his data since aurora is known to occur at latitudes where the Cambridge scintillation data were obtained (Vestine 1944). Vestine's map shows that the line of sight to the radio star passes through the ionosphere at 300-km height in a geographical region for which there is a 2% occurrence of aurora at upper transit of the source, Cassiopeia A, and about 10% occurrence at lower transit. Therefore it might be expected that the contamination of the scintillation data by auroral activity should be a minor factor. However, this

argument is weakened by the well-known fact that there is not a one-to-one correspondence between visible auroral activity and the ionospheric ionization, associated with auroral disturbances, that gives rise to the radio reflections in the very-high-frequency and ultra-high-frequency bands. Collins and Forsyth (1959) have found considerable scattering of very-high-frequency waves by 'radio-aurora' in subauroral latitudes, even at times when visible aurora was not present. Accordingly, the Cambridge scintillation data may not be entirely free of that type of auroral activity which is associated with incoming particles.

It should be noted that high-latitude spread F occurs when the whole ionosphere is disturbed by incoming particles (cf. Hartz 1955*b*) and the possibility cannot be overlooked that some other ionospheric region is responsible for the high-latitude scintillations at the same time that the F signals are spread: when the radio star signal passes through an active aurora at 100-km height and through spread F at 250 km, are the scintillations produced in the E or F region? Certainly, at such times the E region is known to possess irregular ionization structures that have the shape and motions required to produce the observed scintillations (cf. Lyon and Kavadas 1958), and pronounced changes in the scintillation indices have been observed during auroras (Little and Maxwell 1952).

The Vestine map shows that the auroral activity at Ottawa is higher than at Cambridge. The line of sight from Ottawa to the Cassiopeia A source passes through the ionosphere at 300-km height in a region in which there is a 10% occurrence of visible aurora at upper transit and a 50% occurrence at lower transit. Consequently, the effects of auroral activity should be more noticeable in the Ottawa scintillation data. These data will be considered in the following sections, and, in particular, a dependence on particles of solar origin impinging on the ionosphere will be sought in the data. Since the term 'auroral activity' is rather indefinite, several measures of particle precipitation will be considered and correlated with radio star scintillations. This comparison indicates that a mechanism linked with general ionospheric disturbances is responsible for the observed fluctuations at Ottawa.

SCINTILLATION MEASUREMENTS

Radio star scintillations have been recorded at Ottawa on a frequency of 53 Mc/s for a number of years. A phase-switching interferometer receiver of more or less conventional design (Ryle 1952) has been used to monitor the intense source Cassiopeia A. The recording station was so located (latitude 45.4° N., longitude 75.9° W.) that the source never set. Continuous records were obtained with a time constant of 1.5 seconds in the meter circuit. The charts were analyzed by assigning an index to the amplitude and the rate of fluctuation for each hour of recording. Amplitude indices ranging from 0 to 5 were chosen on the basis of the ratio of the fluctuation amplitude to the amplitude of the sinusoidal recorder pattern. Examples of the respective amplitude indices are shown in Fig. 1. The rate indices used ranged from 0 to 4, where 0 meant no scintillations, 1 was assigned to describe the slowest

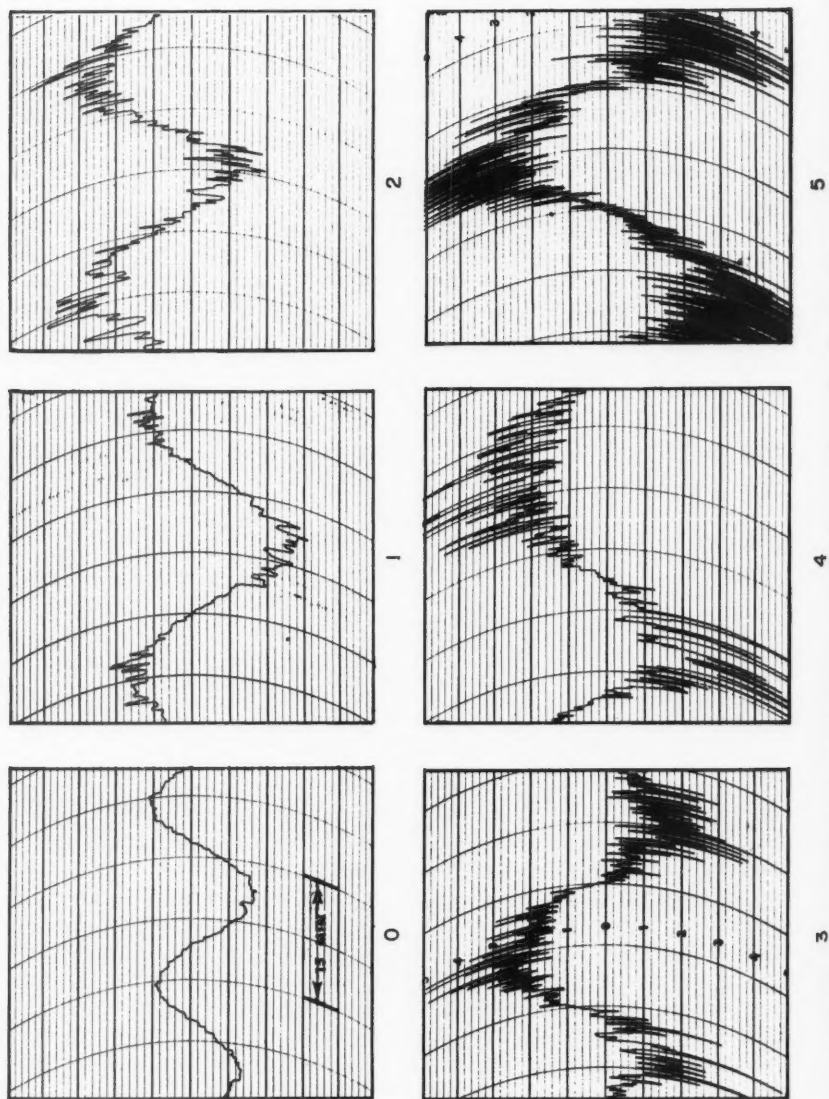


FIG. 1. Samples of the scintillation amplitude indices.

fluctuations observed, and higher indices for increased scintillation rates with 4 characterizing the most rapid rates recorded. Examples of the rate indices are shown in a paper by Reid (1957). The reader may note that the present amplitude indices differ somewhat from those described in an earlier paper (Hartz 1955a): these new indices permit a finer gradation of fluctuation amplitudes and do not affect any of the basic conclusions of the previous analysis.

The earlier work showed that the scintillations observed at Ottawa did not agree with results obtained elsewhere (Hartz 1955a). In particular, scintillations were observed at all hours of the day, and, while a nighttime maximum of occurrence was noted, it was not a large maximum. Moreover, no definite correlation with the spread- F phenomenon could be established. Further considerations disclosed that there was a significant angle-of-elevation dependence in the data, such that at low angles of elevation the fluctuations occurred more frequently. It is easy to see from the geometry involved that as the angle of elevation of the source changes at the receiving site, the distance from the zone of maximum auroral occurrence to that ionospheric region at a given height through which the rays pass also changes. Consequently, the observed angle-of-elevation dependence for scintillation occurrence can equally well be described as a dependence on the distance that the active region in the ionosphere is from the so-called Auroral Zone. In fact, the latter explanation is a much more acceptable one since Ryan and Harrower (private communication), on the basis of scintillation measurements made at Kingston, Ontario, have found that the angle-of-elevation dependence for sources in the southern sky does not correspond with that found in the northern sky.

As the Auroral Zone is considered to be that region in which most of the incoming solar particles precipitate, it seems worth while to explore the connection between the Ottawa scintillations and the incoming particles. For this it is necessary to be quite definite in the criteria which establish the occasions on which particles are said to be entering the ionosphere. Direct observations of the particles are virtually impossible, so that indirect measurements must be used if continuous data are to be obtained. In the following sections several such indirect measures of particle precipitation will be considered and their relationship to radio star scintillations will be examined.

SCINTILLATION RATES

The data for the rates of scintillation for the 2-year period from July, 1955, to July, 1957, were summed and plotted as a function of solar time, as shown in Fig. 2. In this diagram the percentage of the time that each fluctuation index occurs is shown for each hour of the day. It can be seen that the high scintillation rates predominate at night and the lower rates in the daytime. This is shown better in Fig. 3 where the percentage occurrence of high scintillation rates, that is indices 3 and 4, is plotted in curve A. For interest, the percentage occurrence of high scintillation amplitudes (Hartz 1955a) is also presented here in curve B. It is evident that some correspondence exists between the two measures as both curves indicate higher activity at night

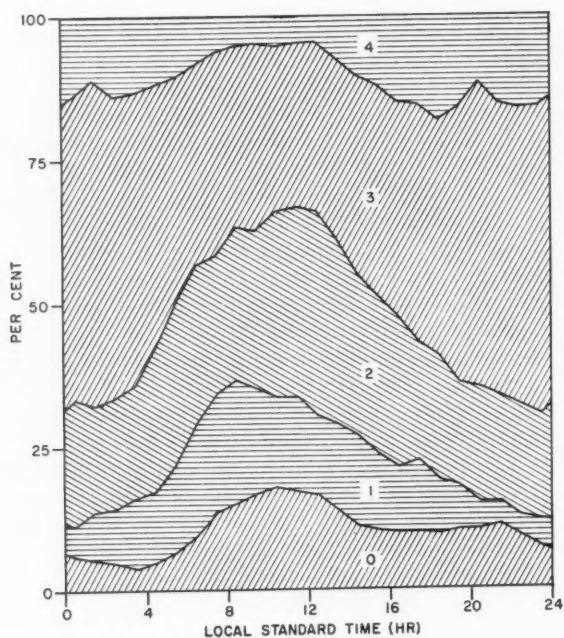


FIG. 2. Percentage occurrence of the various scintillation rates as a function of solar time.

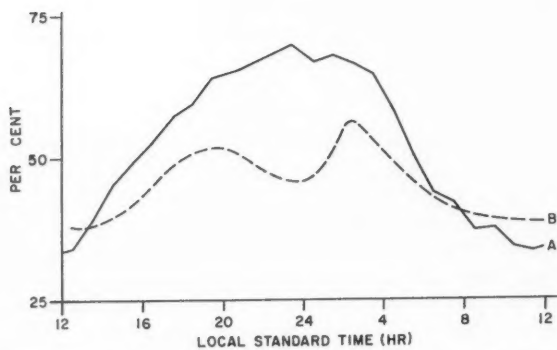


FIG. 3. Percentage occurrence (A) of high scintillation rates, and (B) of high scintillation amplitudes as a function of solar time.

than during the daytime. An hour-to-hour correlation between the unsmoothed amplitude and rate data for the 2-year period yielded a correlation coefficient of $+0.44$.

The scintillation rate data were also summed and plotted as a function of sidereal time. This is presented here as Fig. 4: the ordinate shows the per-

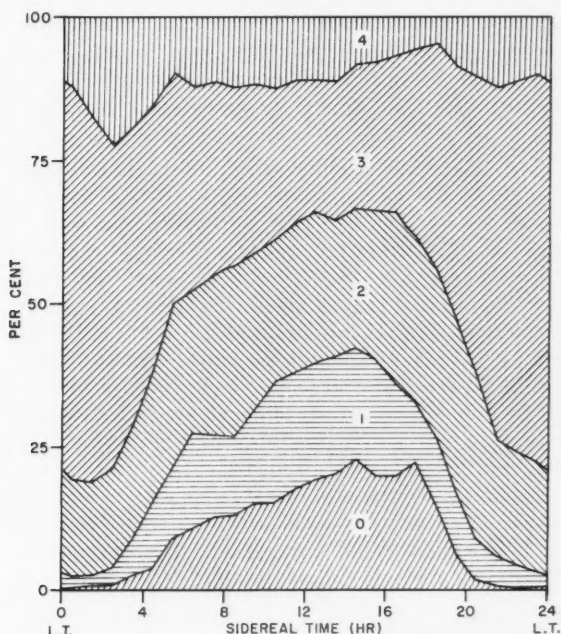


FIG. 4. Percentage occurrence of the various scintillation rates as a function of sidereal time. Lower transit of the source is taken as 0 hours.

centage occurrence of the various scintillation rates and the abscissa is the time in sidereal hours after lower transit of the source. It may be seen that at low angles of elevation of the source the higher rates (particularly index 3) predominate, while at high angles of elevation the lower rates predominate. (For Ottawa the angles of elevation at lower and upper transits of Cassiopeia A are respectively 13.9° and 76.9° .) If again one considers only the high scintillation rates, namely, indices 3 and 4, the graph shown in curve A of Fig. 5 is obtained, while curve B of that figure gives the percentage occurrence of the high scintillation amplitudes (Hartz 1955a) for comparison. Again it is apparent that there is considerable correspondence between the high scintillation rates and the high scintillation amplitudes.

From the foregoing it is readily seen that, on the average, there is a component in the scintillation data which varies with the sidereal period of 23 hours 56 minutes 4 seconds. Whether this can be considered as due to the

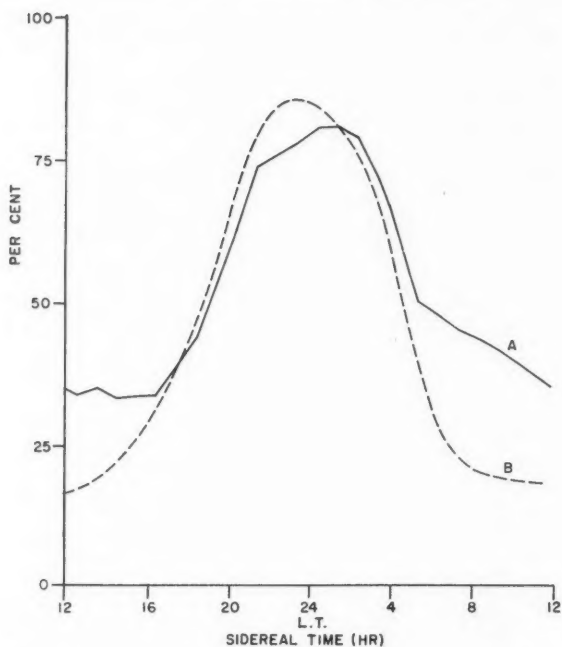


FIG. 5. Percentage occurrence (A) of high scintillation rates, and (B) of high scintillation amplitude as a function of sidereal time.

changing path length for the radiation through an ionospheric layer, or to the changing distance from the Auroral Zone of the ionospheric region where the radiation penetrates, is not immediately clear from only this evidence. Likewise, the scintillation data contain a component which varies, in general, with a period of 24 hours. No doubt this is related in some way to ionospheric conditions which depend on solar radiations. Before any conclusions could be drawn on the relation of the radio star scintillations to incoming solar particles, these respective components had to be removed from the scintillation data. This was done by applying a 24-hour running average to the data. The smoothed scintillation rate indices were then examined for evidences of incoming corpuscles on a 3-hour basis. The results are presented in the following sections.

MEASURES OF IONOSPHERIC DISTURBANCES RESULTING FROM INCOMING PARTICLES

Ionospheric disturbances may be classified according to their generation mechanisms into two main types: those which are produced by abnormal electromagnetic radiations, and those which are attributable to charged particles which enter the ionosphere. This latter category has been shown

to contain those events which are characterized by magnetometer disturbances, visual auroral displays, and abnormal variations in the electron density of the upper atmosphere. It is generally accepted that the responsible particles have a solar origin, and that as the particles enter the earth's environment they produce abnormal conditions in the ionosphere so widespread and complex that they cannot be described adequately in any way other than as a general 'ionospheric disturbance'. The accompanying magnetic storm, auroral features, etc. are only particular features of the general disturbance resulting from the precipitating particles. For the present purposes such features will be used as indicators of the incoming solar particles.

(a) *Geomagnetic Data*

The planetary indices of magnetic activity were used as indications of general ionospheric disturbances that result from incoming particles. It was felt that the planetary indices provided a measure of the currents that flow in the ionosphere, probably even in the ring current if such exists, as a consequence of the solar corpuscles. It has already been established that there is positive correlation between scintillation indices and the planetary magnetic indices and also between scintillation indices and local magnetic indices, with the coefficient of the latter being greater than that of the former (Costain 1955; Dag 1957b). This is to be expected if both scintillations and local magnetic variations are measures of related ionospheric conditions in the vicinity of the observing station. However, for the present analysis the relationship of the scintillation indices to incoming particles was sought and the planetary indices were considered more reliable for this than are local indices of magnetic activity.

The K_p indices were smoothed by applying a 24-hour running average to make them compatible with the scintillation rate data, and then a correlation was carried out on a 3-hour basis. For the 2-year period, July 1955–July 1957, a correlation coefficient of $+0.54$ was obtained for these two sets of data.

(b) *Ionospheric Data*

It was difficult to decide on a single ionospheric parameter that could be easily measured which would give a reliable indication of incoming particles. While certain observations of the F region by means of an ionosonde are probably acceptable most of the time, a difficulty arises just at times of disturbance, because of D -region absorption. A choice was finally made of the transmission quality on a long-range high-frequency communication path which skirted the Auroral Zone. The data were obtained from the Canadian Overseas Telecommunications Corporation for the trans-Atlantic circuit between Montreal and London. Hourly indices ranging from 0 to 5 had been assigned according as reception conditions were excellent, good, fair, poor, very poor, or 'black-out'. While, strictly speaking, this was not a quantitative measure, it could still serve as a reliable indication of abnormal conditions since the operator made a comparison to what would be normal reception for him. Further, the operator would adjust for the changing transmission conditions at different times of the day and year in accordance

with the changing ionosphere, and list transmission quality relative to what would be normal for that particular time.

Because the reflection process was involved, this particular measure provided disturbance data for only the lower regions of the ionosphere. To be sure, similar data could have been obtained from vertical soundings, but it would have been in a less convenient form since the automatic recorder cannot make a comparison with normal ionosphere conditions as can the manual operator. Moreover, the trans-Atlantic path was preferred to any other operational circuit since it skirted the Auroral Zone, which is considered the most likely region for the precipitation of incoming charged particles.

The trans-Atlantic quality data for the 2-year period, July 1955–July 1957, were smoothed by applying a 24-hour running average. In this way, minor fluctuations were smoothed out, as were the daytime effects of the sun's ultraviolet radiation. The major variations that remained in the data could be attributed to corpuscular radiation. These smoothed data were then correlated with the smoothed K_p data and the smoothed scintillation rate indices on a 3-hour basis. Correlation coefficients of +0.66 and +0.29 respectively were obtained.

(c) *Auroral Data*

An observer near the Northern Auroral Zone sees the aurora borealis almost every clear night, but further south the frequency of overhead aurora decreases, until in southern Canada it is a fairly rare phenomenon. While aurorae are considered to occur as a consequence of incoming charged particles, a quantitative measure of the particles is difficult to establish from the visible aurora since so many parameters are involved. A possible measure of the particles seems to be contained in the latitude at which the aurora is seen, since sightings at southern latitudes are known to occur mainly at times of intense disturbance.

Data on the position of the aurora as a function of time for a recording site at Saskatoon (latitude 52.1° N., longitude 106.6° W.) were made available to the author by Dr. D. M. Hunten. From these, the most southerly extent of the aurora for each night of observation was chosen as a measure of the auroral disturbance. The lower frame of Fig. 6 shows these observations in terms of geographic latitude for the month of January, 1956. (Note that the latitude range 54° – 50° was all that could be reported reliably from the one site, and on occasions when the aurora extended beyond the limits of observability in the south, only the limiting latitude was given.) In the diagram, the closed circles represent a weak display, while the open circle represents a more intense display.

The auroral data were so discontinuous as to make the calculation of a correlation coefficient very difficult and none was attempted. However, when portrayed in graphical form, of which Fig. 6 is an example, it was found that the maxima on the scintillation rate curves tended to occur on those days when aurora was observed at the lower latitudes, and was of increased intensity.

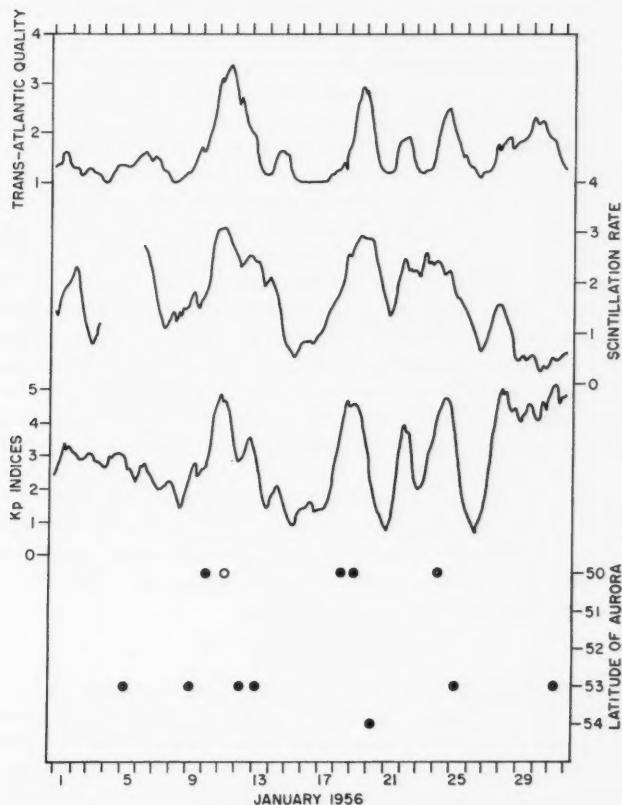


FIG. 6. Measures of ionospheric disturbance for the month of January, 1956. Plotted here are the smoothed trans-Atlantic quality indices ranging from 0 for excellent to 5 for 'black-out', the smoothed scintillation rate indices, the smoothed planetary magnetic indices, and the southernmost extent of the aurora borealis on each night for which records were available (the open circle represents a very intense display).

Also plotted in Fig. 6, for comparison, are the smoothed data on trans-Atlantic propagation quality, radio star scintillation rates, and planetary magnetic indices for January, 1956. It may be seen that the four different measures presented in the diagram are not independent, as a substantial degree of correlation exists between the respective sets of data. In particular, the large significant disturbances seem to be portrayed reliably by any one of the four, and it is only with the lesser disturbances that differences in the observed effects occur. Such differences can probably be attributed to differences in the latitude or height in the ionosphere at which the particular measurements apply. On the whole, it is believed that each phenomenon plotted here is a manifestation of corpuscular radiation from the sun.

The reader is reminded that the planetary magnetic indices are indicative of the total motion of charges in the ionosphere which arise from the incoming corpuscles. If abnormalities in the electron densities occur in the lower ionosphere these would probably affect the magnetic indices as well as the trans-Atlantic quality figures, and hence the correlation coefficient of $+0.66$. The motions of small regions of ionization at high levels in the ionosphere, which probably contribute to the observed scintillation indices, also add to the current fluctuations which determine the K_p values, and hence the correlation coefficient of $+0.54$. That higher ionospheric regions than those which determine the high-frequency quality data are involved in some of the scintillation measurements is inferred from the low correlation coefficient between scintillation rates and the short-wave quality figures, namely $+0.29$. If this is the case, it might be expected that if the trans-Atlantic quality data and the scintillation rate data were combined, and then compared with the K_p indices, a higher correlation coefficient would result. When the indices for the 2-year period were added together, and the correlation was carried out on a 3-hour basis, the result was a correlation coefficient of $+0.72$ between the trans-Atlantic quality and scintillation rate combination and the K_p data. This result is consistent with the general belief that scintillations arise in or above the F region of the ionosphere. It is also consistent with the hypothesis that a part of the scintillations arise in the E region above the level where high-frequency absorption occurs, since D -region absorption is the major factor that affects the trans-Atlantic quality data.

DISCUSSION

There can be no doubt that the radio star scintillations observed at Ottawa, and probably at other stations of comparable latitude, are definitely associated with the large ionospheric disturbances which result from incoming solar particles. (In a subsequent paper the author will show the dependence of the significant ionospheric disturbances in this period on specific solar events, and thereby establish the solar origin of the particles in each case.) There can also be no doubt that there is a definite diurnal dependence in the scintillation, but this should cause no surprise since there are other geophysical phenomena associated with incoming particles which also exhibit a diurnal variation. These include local magnetic disturbances, radar reflections from auroral ionization, and the scattering of very-high-frequency radiations in the forward direction by auroral ionization. In fact, the similarity of the curves in Fig. 3 to the diurnal variations of each of these three phenomena is sufficiently great to indicate by itself a definite relation between the respective sets of data (cf. Bullough and Kaiser 1955; Collins and Forsyth 1959). Kaiser (1956) has already drawn attention to this similarity, particularly in connection with the minimum at midnight, and has drawn the obvious conclusion that some portion of the scintillations at least must be produced in the E region by the intense irregularities which are shown to exist by the auroral radar echoes.

There seems to be little argument against Briggs's conclusion that the scintillations not associated with auroral activity are closely related to the

F-region irregularities that produce the spread-*F* echoes on ionosonde records (Briggs 1958*a*, *b*). But what of the scintillations that are associated with auroral activity? Here, the matter of the height of the scintillating region in the ionosphere requires more intensive consideration. *F*-region irregularities of ionization capable of scattering very-high-frequency radio waves are known to exist at times when aurora is present. The author has observed a forward-scatter signal at 40 Mc/s on a 3000-km circuit at a time when aurora occurred along the path: for a path of this length the ionosphere below 170 km at the mid-point was not illuminated by the transmitter nor observed by the receiver. Peterson *et al.* (1955) and Nakata (1958) have also observed return echoes from *F*-region irregularities which were associated with auroral phenomena.

On the other hand, *E*-region irregularities capable of scattering very-high-frequency radiations are well known. Recent work by Collins and Forsyth (1959) on signals scattered in the forward direction has shown that several different types of irregularities are involved, not all of which are associated with visible auroral phenomena. They were able to determine the height of the scattering region and in most cases the results showed heights of less than 100 km.



FIG. 7. Map of the Ottawa area showing lines of equal percentage auroral occurrence, after Vestine (1944). Also shown is the locus of intersection with the 300-km level of the ionosphere of a line joining Ottawa to Cassiopeia A. The numbers on the locus represent sidereal time in hours after lower transit.

Apparently, during disturbances that result from incoming solar particles all ionospheric heights are affected to some degree or other. From the information available it does not seem likely that any one height can be designated as the exclusive origin of the scintillations that occur at such times. This conclusion can be substantiated further through the following argument.

If the ionospheric region responsible for the scintillations could be confined to a limited height range, it should be possible to determine this height from the observed variation of scintillation occurrence with sidereal time. Vestine's map of auroral occurrence can be considered as representative of the geographical distribution of ionospheric structures associated with incoming particles, particularly since it is so similar to the map which portrays the magnetic disturbances (Vestine 1944). In Fig. 7 is shown a portion of this map covering the Ottawa area, and including the locus of points of intersection with the 300-km level of the ionosphere of lines drawn from Ottawa to the source in Cassiopeia. The figures on the locus are the time measured in sidereal hours after lower transit of the source. If the percentage occurrence of aurora at each hour is obtained by an interpolation process from this diagram, the values plotted in Fig. 8 are obtained. It will be seen that there is considerable similarity between this curve and the curves of Fig. 5. One might expect that a somewhat different choice of height for the scattering layer could be made which would permit

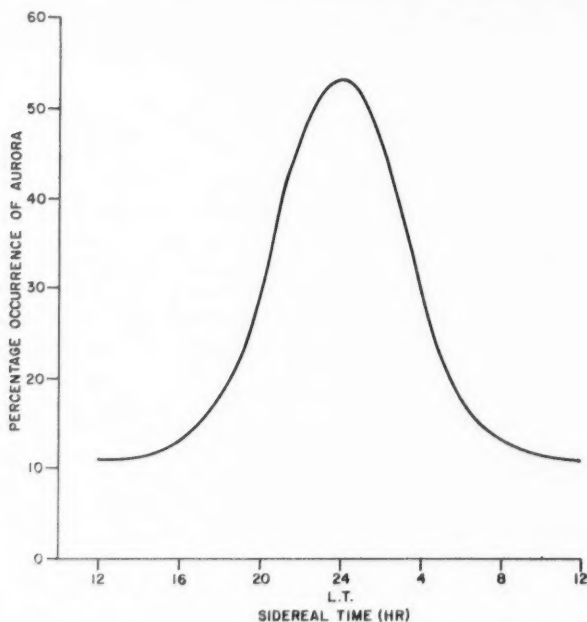


FIG. 8. The percentage occurrence of auroral activity as a function of sidereal time as deduced from Fig. 7.

better agreement with the experimental curves of Fig. 5, but this has not been possible. Almost any height less than about 600 km would have resulted in a curve of similar shape, but a close fit could only be obtained through a normalization procedure which would be difficult to justify. This may be due to the fact that the treatment has been too elementary and the scattering properties of the irregularities have not been considered properly, or to the possibility that the irregularities are actually distributed through an extensive range of heights. In the light of the foregoing argument on *E*- and *F*-region structures the latter suggestion should be given serious consideration.

SUMMARY

The radio star scintillations observed at Ottawa have been examined for a dependence on incoming charged particles which produce ionospheric disturbances. The planetary indices of magnetic activity, the quality of reception on a high-frequency path that skirted the Auroral Zone, and the lowest latitude at which aurora was observed were taken as reliable measure of ionospheric disturbances caused by solar particles. The scintillation data, from which diurnal variations had been smoothed, correlated significantly with each of the three disturbance measures, and therefore must be taken as representative of ionization structures produced by the precipitation of corpuscles. It has not been possible to determine the height of the scintillating region in the ionosphere directly, but it is known that during ionospheric disturbances man-made transmissions have been scattered in the forward direction by irregularities in the *E* region and the *F* region of the ionosphere, and therefore it is difficult to exclude the possibility that the scintillations are produced in an extensive range of heights.

At latitudes where the auroral activity is much less the scintillations are known to correlate with spread-*F* echoes and presumably originate in the *F* region. It should not be taken that such scintillations are not found in the Ottawa records, but rather that they do not predominate. The best explanation is that the recordings show the presence of both types of scintillations.

ACKNOWLEDGMENTS

The author wishes to acknowledge his indebtedness to Messrs. W. A. Sharf and W. E. Mather, and various other members of the technical staff of the Defence Research Telecommunications Establishment who assisted with the observations and undertook much of the routine maintenance of the recording equipment. Dr. G. C. Reid scaled some of the scintillation recordings and Mrs. M. Bree assisted with some of the data reduction.

The many helpful discussions with Drs. C. O. Hines and P. A. Forsyth are also gratefully acknowledged.

REFERENCES

- BOLTON, J. G., SLEE, O. B., and STANLEY, G. J. 1953. Australian J. Phys. **6**, 434.
BOOKER, H. G. 1958. Proc. I.R.E. **46**, 298.
BRIGGS, B. H. 1958a. J. Atmospheric and Terrest. Phys. **12**, 34.
——— 1958b. J. Atmospheric and Terrest. Phys. **12**, 89.

- BULLOUGH, K. and KAISER, T. R. 1955. *J. Atmospheric and Terrest. Phys.* **6**, 198.
COLLINS, C. and FORSYTH, P. A. 1959. *J. Atmospheric and Terrest. Phys.* **13**, 315.
COSTAIN, C. H. 1955. Radio star scintillations close to the auroral zone. M.A. Thesis, University of Saskatchewan, Saskatoon, Saskatchewan.
DAGG, M. 1957*a*. *J. Atmospheric and Terrest. Phys.* **10**, 204.
——— 1957*b*. *J. Atmospheric and Terrest. Phys.* **10**, 194.
——— 1957*c*. *J. Atmospheric and Terrest. Phys.* **11**, 133.
——— 1957*d*. *J. Atmospheric and Terrest. Phys.* **11**, 139.
HARTZ, T. R. 1955*a*. *Can. J. Phys.* **33**, 476.
——— 1955*b*. *Nature*, **175**, 908.
KAISER, T. R. 1956. The airglow and the aurorae (The Pergamon Press, Ltd., London).
KOSTER, J. R. 1958. *J. Atmospheric and Terrest. Phys.* **12**, 100.
LITTLE, C. G. and MAXWELL, A. 1952. *J. Atmospheric and Terrest. Phys.* **2**, 356.
LYON, A. J., SKINNER, N. J., and WRIGHT, R. W. 1958. *Nature*, **181**, 1724.
LYON, G. F. and KAVADAS, A. 1958. *Can. J. Phys.* **36**, 1661.
NAKATA, Y. 1958. Rept. Ionosphere Research, Japan, **12**, 1.
PETERSON, A. M., VILLARD, O. G., LEADABRAND, R. L., and GALLAGER, P. B. 1955. *J. Geophys. Research*, **60**, 497.
REID, G. C. 1957. *Can. J. Phys.* **35**, 1004.
RYLE, M. 1952. *Proc. Roy. Soc. A*, **211**, 351.
VESTINE, E. H. 1944. *Terrestrial Magnetism and Atmospheric Elec.* **49**, 77.

THE PHOTODISINTEGRATION OF NEON¹

H. J. HAY² AND J. B. WARREN³

ABSTRACT

A proportional counter, filled to 4-atmosphere pressure with pure neon, and a cylindrical gridded ionization chamber, filled to 9-atmosphere pressure with neon containing some helium, have been irradiated with the gamma-ray flux from a thick lithium target bombarded with 500-kev protons. Pulse height analysis led to the assignment of the following photodisintegration cross sections in millibarns:

$\text{Ne}^{20}(\gamma_{17.6}, \alpha)\text{O}^{16}$, 0.05 to the ground state of O^{16} , 0.67 to the 6.06- and 6.14-Mev levels of O^{16} , 1.80 to the 6.91- and 7.12-Mev levels of O^{16} ;

$\text{Ne}^{20}(\gamma_{14.8}, \alpha)\text{O}^{16}$, 0.086 to the ground state, about 1.0 to the 6.06- and 6.14-Mev levels;

$\text{Ne}^{20}(\gamma_{17.6}, p)\text{F}^{19}$, 21 to the ground and low-lying levels at 110, 197 kev in F^{19} , about 5 to the 1.35- and/or 1.57-Mev levels in F^{19} ;

$\text{Ne}^{22}(\gamma_{17.6}, \alpha)\text{O}^{18}$, 0.76 to the ground level.

The $\text{Ne}^{20}(\gamma, \alpha)\text{O}^{16}$ cross sections are in good accord with the selection rules put forward by Gell-Mann and Telegdi for the photodisintegration of an even-even nucleus.

1. INTRODUCTION

A study of the disintegration of neon nuclei of mass 20 by energetic photons provides an opportunity of examining two aspects of present ideas about photodisintegration processes. In the first place since Ne^{20} , on an alpha-particle model, may be regarded as a bipyramid of alpha-particle groupings, then for photon energies not big enough to disrupt the alpha structures the charge center will not oscillate with respect to the mass center under the influence of electric dipole radiation. Thus the absorption process would be expected to arise from magnetic dipole or electric quadrupole interaction. Following the excitation of the compound nucleus, if the binding between the alpha-particle configurations is relatively small, then the ejection of an alpha particle should be a quite probable process. The reaction $\text{Ne}^{20}(\gamma, \alpha)\text{O}^{16}$ was in fact the first observed photodisintegration process in neon. Erdman and Barnes (1953), and in greater detail Erdman (1953), studied this reaction using the radiation from lithium bombarded by protons and observing the disintegrations produced in neon contained in a parallel plate gridded ionization chamber. They found a surprisingly small cross section for the disintegration proceeding to the ground state of O^{16} and noticed that considerably more transitions occurred to the 6- and 7-Mev excited levels in O^{16} . Preston (1950) has given a theoretical analysis of the $\text{O}^{16}(\gamma, \alpha)\text{C}^{12}$ process which might be expected to apply to the photo-alpha disintegration of neon yielding a cross section of similar order of magnitude. Gell-Mann and Telegdi (1953) investigated the consequences of the charge independence of nuclear forces

¹Manuscript received April 27, 1959.

Contribution from Physics Department, Australian National University, Canberra, Australia.

²Present address: Nuclear Physics Division, Atomic Energy Research Establishment, Harwell, England.

³Present address: Physics Department, University of British Columbia, Vancouver, British Columbia.

on the absorption of photons by light nuclei and showed that isotopic spin conservation should lead to strong, clear-cut selection rules for the case of even-even nuclei such as $^{10}\text{Ne}^{20}$. Again, by observation of the alpha energies the disintegrations via excited states in O^{16} are quite apparent and so this technique provides another opportunity of checking the non-existence, according to the alpha-particle model, of low-lying states of the O^{16} nucleus.

A second process of interest is the photoproton disintegration $\text{Ne}^{20}(\gamma, p)\text{F}^{19}$. Studies of the gamma-ray yield from the reactions $\text{F}^{19}(p, \gamma)\text{Ne}^{20}$, $\text{F}^{19}(p, \alpha\gamma)\text{O}^{16}$, $\text{F}^{19}(p, \alpha\pi)\text{O}^{16}$ (Willard 1952; Sinclair 1954) show that the levels of the compound nucleus Ne^{20*} are reasonably well separated even at excitations of 17 Mev. Consequently, by the principle of reciprocity, the cross section $\sigma(\gamma, p)$ could show quite sharply resonant behavior which might be detectable by varying the gamma-ray energy over a small range. A direct numerical check too on the applicability of the reciprocity relation, $g_1\sigma(\gamma, p)/\lambda_p^2 = g_2\sigma(p, \gamma)/\lambda_p^2$ might also be feasible, since with modern van de Graaff accelerators the same excitation in Ne^{20} can be reached either by proton bombardment of fluorine or by absorption of 17.6-Mev quanta in Ne^{20} . The prime difficulty with the (p, γ) measurement would, of course, lie in measuring only the weak direct-capture radiation component in the large flux of other gamma radiations.

Because neon is an excellent counter gas, except for its low breakdown voltage, the photodisintegration process leading to charged particle emission may be conveniently studied by means of a proportional counter or ionization chamber technique, pulse amplitude analysis giving the energy released in the counter from the disintegrations. Moreover, the range of alpha particles is very much less than that of protons of comparable energy, so that a change in the gas pressure permits a clear distinction between groups in the pulse height distribution arising from (γ, α) reactions and those from (γ, p) reactions. This was the method used in our study of the photodisintegration of neon by the $\text{Li}^7(p, \gamma)\text{Be}^8$ radiation.

2. EXPERIMENTAL APPARATUS

(a) *Source of Radiation and Monitoring*

The gamma radiation was generated by bombarding a thick evaporated layer of metallic lithium with a resolved 500-keV energy proton beam of up to 400 microamperes from the A.N.U. Cockcroft-Walton cascade generator. This radiation comprises two components, one sharp, of energy 17.6 Mev with a spread of only 12 keV, and the other broad, centered around an energy of 14.8 Mev with a spread of about 2 Mev. The intensity ratio, $I(17.6)/I(14.8)$, at 0° to the beam amounts to 1.6/1 (Stearns and McDaniel 1951). The yield, according to Fowler and Lauritsen (1949), for a clean fresh target at the 440-keV resonance is about 1.2×10^5 gammas per microcoulomb, or 2×10^{-8} gammas per proton, and this is increased by about 10% at 500 keV by the contribution from protons above the resonance energy.

The radiation was monitored with a brass Geiger counter of similar construction to that calibrated by Barnes *et al.* (1952) having an efficiency at the mean effective photon energy of 16.4 Mev of 2.5 counts per photon per

square centimeter and this figure is believed to be reliable to within $\pm 10\%$. Generally the flux for a given charge was only about one-half that computed from the yield data; only when the target had been freshly laid down was the full yield obtained.

Background counts with the beam stopping on a clean copper target showed that very few counts in the monitor Geiger arose from X rays from the accelerator, the counting rate remaining at about 32 counts/minute with the beam on or off. Carbon build-up on the target and consequent radiation from the $C^{12}(p, \gamma)N^{13}$ reaction, with a resonant yield of $7.3 \cdot 10^{-10}$ gammas per proton at 456-kev bombarding energy, was largely avoided by placing a liquid air trap immediately in front of the target and running the target quite hot. There was no evidence after any run of a significant 10-minute positron activity from N^{13} build-up. Checks made with a neutron-sensitive, gamma-insensitive scintillation counter showed that the number of neutrons originating from the bombarded target assembly was negligible.

(b) *The Proportional Counter*

With the amount of very pure neon available to us it was decided first to investigate the (γ, α) reaction using a proportional counter, of conventional cylindrical design with a sensitive region 4 in. I.D. $\times 9\frac{5}{16}$ in. long; the .005-in. diameter central wire was provided with shield and field tubes, the latter extending $2\frac{1}{2}$ inches inside the walls at each end. After purifying the gas by circulation over hot calcium, the counter was operated at low gas gain and, with differentiating and integrating time constants of 8 microseconds, the width of the 5.16-Mev alpha group from a plutonium energy calibration source was 6%.

(c) *The Gridded Ionization Chamber*

In order to study the $Ne^{20}(\gamma, p)F^{19}$ process it was necessary to use much greater stopping power in the counter, i.e. a higher pressure and bigger volume. Consequently a cylindrical geometry, gridded ionization chamber was built as shown in Fig. 1. The main advantage of such a chamber over a proportional counter for this work is that the field at the walls may be made much larger, bearing in mind that the total applied voltage is limited by the breakdown voltage in neon, thereby reducing the effects of possible contamination. The cylindrical design makes better use of the available gas than does a parallel plate chamber.

The neon available to fill this chamber was rather impure, containing in particular 25% nitrogen and 15% helium. This gas was passed in at about 5 cc/second through a system consisting of an activated charcoal trap in liquid air, followed by a hot (350° C) calcium purifier, and followed by a further charcoal trap. Mass spectrograph analysis, kindly undertaken by Dr. J. H. Richards of this laboratory, showed the final gas composition to be Ne^{20} 70.05%, Ne^{22} 7.15%, He 22.80%, the nitrogen having been successfully removed. The presence of the helium appeared to raise the breakdown potential of the gas and it was possible to run with 4000 volts potential difference between anode and wall at a total gas pressure of 132 lb/in.², this limit actually

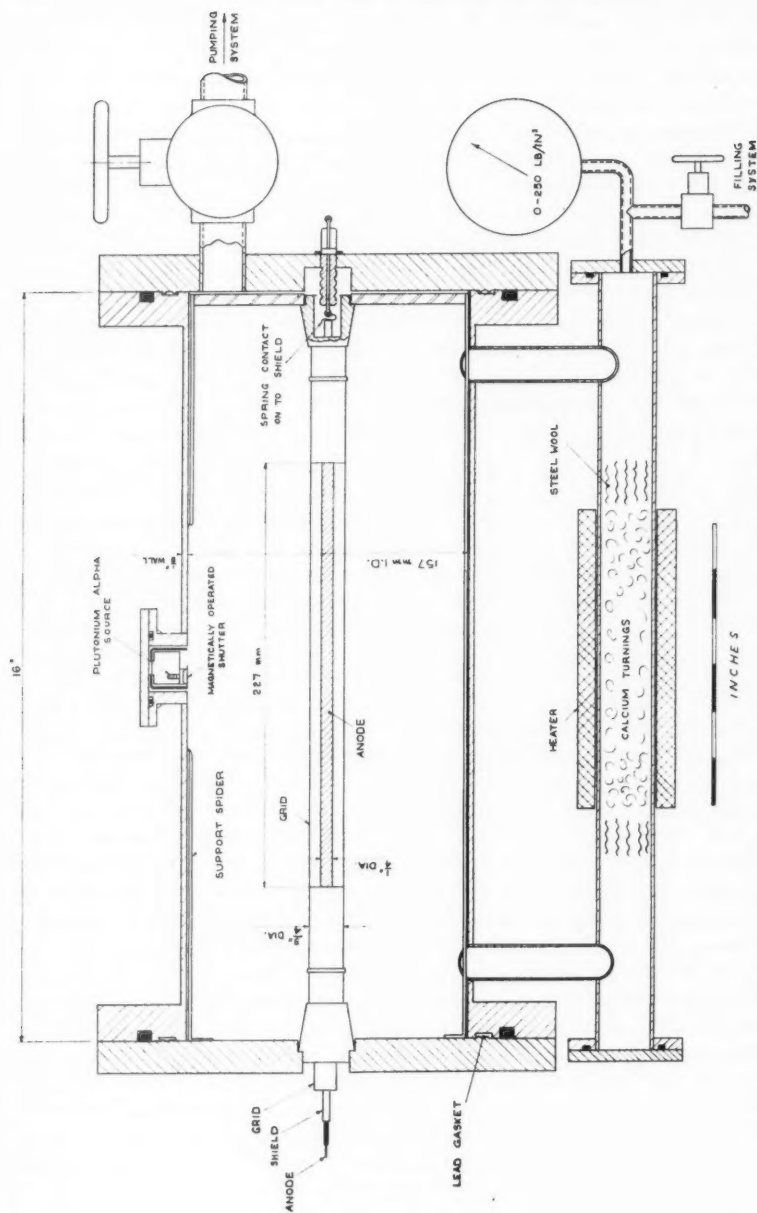


FIG. 1(a). The cylindrical gridded ionization chamber. The grid consists of 30 wires of 0.068-in. diameter 'Minaepha' wire.

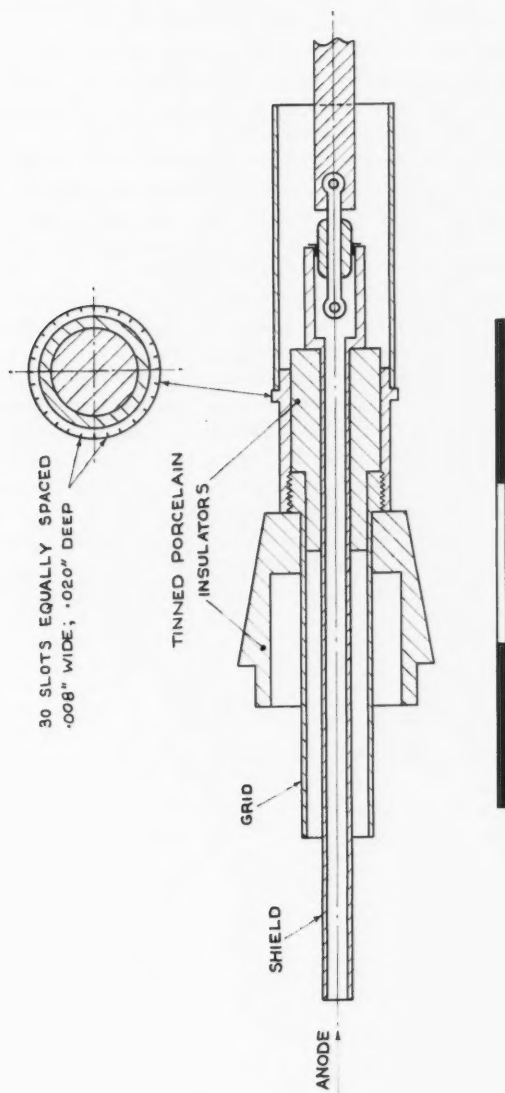


FIG. 1(b). Detail of the porcelain seal.

being set by the power supply noise as the collector was run at high potential. The grid potential was set at one-half of the anode potential as indicated by calculation, and tests made with various grid voltages showed that this choice was about optimum, though neither resolution nor pulse height was a very sensitive function of grid voltage. Calculation (Bunemann *et al.* 1949; Wilkinson 1950; Whitehouse and Galbraith 1950) showed that the grid-shielding efficiency under these conditions was 0.96 while its transparency to electrons was unity. The minimum value of E/p in the chamber was 0.019 volts/cm per mm compared with 0.005 in the proportional counter, and with this chamber there was much less difficulty with contamination. The calculated maximum electron-collection time for 10-Mev alphas of range $2\frac{1}{2}$ cm at this pressure was about 15 microseconds, while for 4.7-Mev protons of range about 6 cm it was 30 microseconds, taking the electron drift velocity to be $1\sqrt{(E/p)}$ cm per microsecond in the gas (English and Hanna 1953); experimental results showed that these figures were approximately correct.

It was found possible to achieve a width for the plutonium alpha group* of less than 5% for values of the amplifier integration and differentiation time constants in the range 5 to 50 microseconds. The wall thickness was reduced to $\frac{1}{8}$ inch around the sensitive region to reduce electron pile up. Nevertheless, with the gamma fluxes used this calibration peak was considerably broadened, to about 10% width, by the electron noise, and collimation of the beam made little improvement. The group widths obtained in photodisintegration runs were rather broader still ($\sim 12\%$), indicating a small additional spread caused either by the events being distributed uniformly

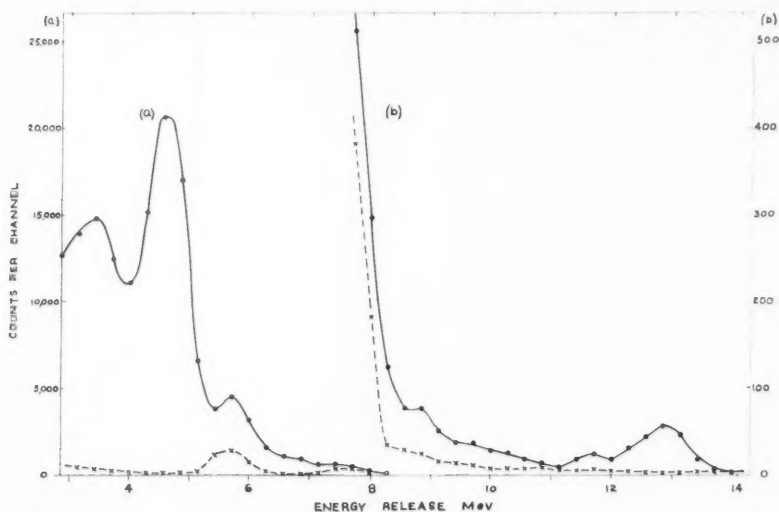


FIG. 2. Pulse height spectrum from neon-filled ionization chamber irradiated with $\text{Li}^7(p, \gamma)$ radiation and background.

*The plutonium source was kindly supplied by the Atomic Energy Research Establishment, Harwell, England.

throughout the sensitive volume or by the nature of the events themselves. This width was obtained with an integration time constant of 8 microseconds and a differentiation time of 8 or 20 microseconds, the latter being as short as was compatible with the variations in rise times. The time required for an experimental run was found to be set by electron pile up, not by the total gamma flux available. Consequently, some improvement in resolution might be achieved by the provision of thin low Z windows for the radiation which would also permit the use of higher proton beams, i.e. greater than 200 microamperes, to reduce the importance of counter background. The natural background of this chamber was quite low but two peaks were evident at energies of 5.7 and 7.5 Mev, as shown in Fig. 2.

3. POSSIBLE REACTIONS

As natural neon contains three isotopes in the proportions 90.51% Ne²⁰, 0.28% Ne²¹, 9.21% Ne²², and since the induced transitions may go to excited levels in the product nuclei, from the energetic point of view there are numerous

TABLE I

Reaction	Level in residual nucleus	Energy release, Mev	(Light) particle energy, Mev	(Light) particle range in chamber, cm	Number of events	Loss	Cross section, millibarns
(A) Type $\text{Ne}^{20}(\gamma, \alpha)\text{O}^{16}$, $Q = -4.75$ Mev							
1 $E_\gamma = 17.63$ Mev	Ground level	12.88	10.3	2.45	200	.200	.050
2	6.06 and 6.14	6.8	5.4	.82	3,130	.067	.67
3	6.91 and 7.12	5.9	4.7	.65	8,550	.056	1.80
4	9.58 (broad)	3.3	2.6	.29			
5	9.84	3.0	2.4	.26			
6	10.36	2.5	2.0	.23			
7	11.25 (broad)	1.6	1.3	.13			
11 $E_\gamma = 14.8$ Mev	Ground level	10.0	8.0	1.55	230	.128	.086
12	6.06 and 6.14	3.9	3.1	.37	2,800	.030	About 1
13	6.91 and 7.12	2.9	2.3	.25			
(B) Type $\text{Ne}^{22}(\gamma, \alpha)\text{O}^{18}$, $Q = -9.66$ Mev							
1 $E_\gamma = 17.63$ Mev	Ground level	8.0	6.4	1.08	360	0.89	.76
2	1.98 and perhaps others	6.0	4.8	.69			
11 $E_\gamma = 14.8$ Mev	Ground level	5.1	4.1	.55			
12	1.98	3.1	2.5	.28			
(C) Type $\text{Ne}^{20}(\gamma, p)\text{F}^{19}$, $Q = -12.87$ Mev							
1 $E_\gamma = 17.63$ Mev	Ground and low levels at .110, .197 Mev	4.76 to 4.56	4.5	5.93	61,300	.43	21
2	1.35	3.4	3.2	3.28	About 20,000	.24	About 5
3	1.57	3.2	3.0	2.94			
4	2.82	1.9	1.8	1.25			
11 $E_\gamma = 14.8$ Mev	Ground and low-lying levels	1.9	1.8	1.25			
(D) $\text{Ne}^{20}(\gamma, 2\alpha)\text{C}^{12}$, $Q = -11.9$ Mev							
1 $E_\gamma = 17.6$ Mev	Ground level	5.7					
11 $E_\gamma = 14.8$ Mev	Ground level	2.9					
(E) $\text{Ne}^{20}(\gamma, \alpha p)\text{N}^{15}$, $Q = -16.9$ Mev							
(F) $\text{Ne}^{20}(\gamma, n)\text{Ne}^{19}$, $Q = -16.91$ Mev							

possibilities for the energy which may be released in the chamber as kinetic energy of charged particles. If it is assumed that the energy W lost per ion pair produced by a recoil fragment (O^{16} or F^{19}) is not much different from the same quantity for protons or alphas, then the pulse amplitude produced by a photodisintegration in the chamber is directly proportional to the kinetic energy release. A pronounced difference between the value of W for light particles and the recoil fragments would tend to broaden the peaks.

In Table I are listed those reactions resulting in charged particles which were most likely to be observed in this experiment according to the current energy level diagrams (Ajzenberg and Lauritsen 1955), together with other data relevant to the gridded ionization chamber results.

4. EXPERIMENTAL RESULTS

(a) Reactions Observed

After preliminary runs had established the general form of the pulse height distributions and counting rates to be expected, the pulse spectrum was examined in detail in three sections with the kicksorter resolution in each being made compatible with a reasonable running time. Figure 2 shows a complete spectrum above 3 Mev and the corresponding time-dependent background, taken with the gridded ionization chamber and low kicksorter resolution. Figure 3 shows the pulse distribution after background subtraction, due allowance being made for the extra spreading of the two contamination peaks which would arise when the gamma flux passes through the chamber. The assignment of the groups fits well with a linear energy scale based on the position of the plutonium alpha peak at 5.16 Mev.

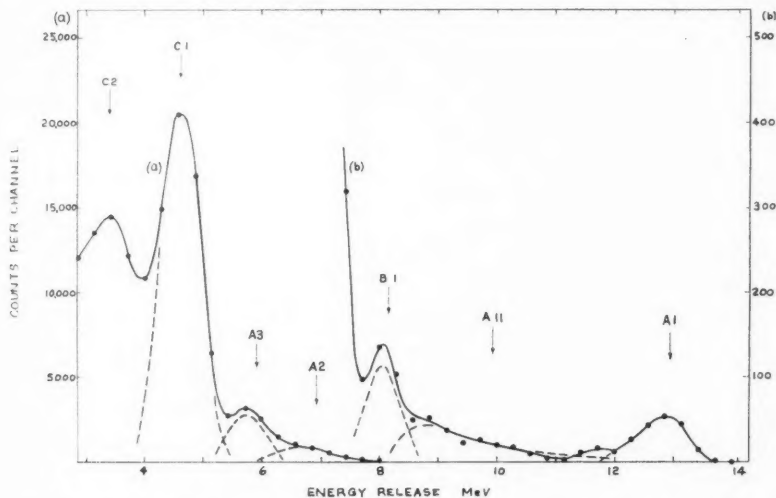


FIG. 3. Pulse height spectrum of particles above 3-Mev energy release in the chamber resulting from the photodisintegration of neon.

While there is little danger of ambiguity in the assignment of the appropriate reaction to the higher-energy peaks, there is considerable uncertainty in the low-energy region of the spectrum which is shown in greater detail in Fig. 4.

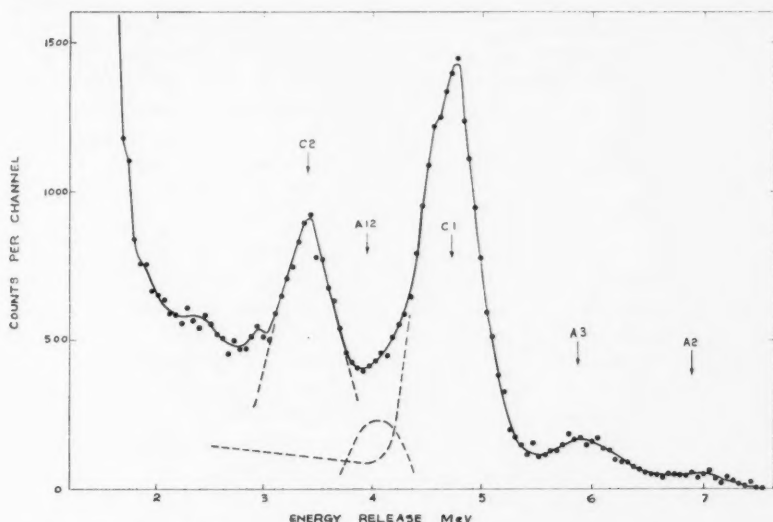


FIG. 4. Pulse height spectrum of low-energy particles resulting from the photodisintegration of neon.

Firstly, the strong peak marked C2, attributed to $\text{Ne}^{20}(\gamma_{17.6}, p)\text{F}^{19*}$ is centered at 3.38 Mev corresponding to a transition to the 1.35-Mev level of F^{19} . There is no marked spread of this peak towards lower energies as might be expected if there were a transition of similar intensity to the 1.57-Mev level of F^{19} . Secondly, the filling in between C1 and C2 in Fig. 4 would seem to arise from reaction A12, i.e. $\text{Ne}^{20}(\gamma_{14.8}, \alpha)\text{O}^{16*}$, the residual O^{16} nucleus being left in the 6.06- or 6.14-Mev states. Some of it might also arise from $\text{Ne}^{20}(\gamma, p)\text{F}^{19*}$ if the doubtful level at 0.9 Mev in F^{19} (Seale 1953) exists. In addition the distribution shows evidence for other groups at 2.93 (A5?), 2.4 (A6?), 2.0, 1.84, and 1.6 Mev (C4 and/or C11?), which might be attributed to reactions indicated in Table I, but for which no reliable cross section can be estimated. The yields from reactions A5 and A6 are expected to be small because of the low barrier penetrabilities, hence most of the counts between 2½ and 3 Mev are probably due to reaction A13, i.e. $\text{Ne}^{20}(\gamma_{14.8}, \alpha)\text{O}^{16*}$, proceeding to the levels in O^{16} near 7 Mev.

Again the large proton peak C1 was examined under high kicksorter resolution and with a reduced gamma-ray flux as it appeared that this group was rather broader than the others. The over-all stability and chamber resolution were hardly adequate to produce convincing evidence, yet, as can be judged

from Fig. 5, which consists of the addition of four separate runs, we believe that this peak is a multiple one and could be resolved into three components of similar intensity separated by about 100 kev.

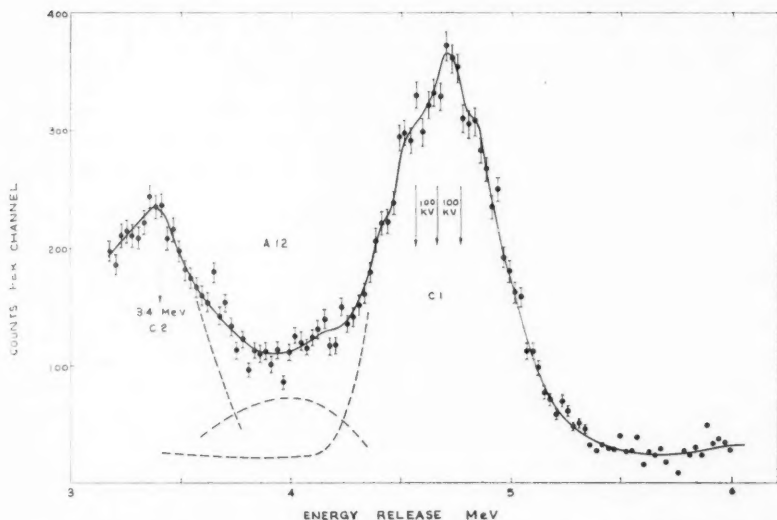


FIG. 5. Detail of the 4.7-Mev photoproton peak from the reaction $\text{Ne}^{20}(\gamma, p)\text{F}^{19}$ arising from 17.6-Mev gamma radiation.

This would suggest that the reaction $\text{Ne}^{20}(\gamma_{17.6}, p)\text{F}^{19}$ proceeds in roughly equal proportions to the ground state and the two low-lying levels of F^{19} at 110 and 197 kev of F^{19} .

(b) Cross-Section Calculations

The cross sections were estimated from the area under the peaks. In the low-energy region where the peaks overlap the areas were estimated by drawing in curves of the expected width and obviously the values so deduced are much more approximate. A wall correction was applied to the observed number of events by numerical integration based on the range of the alpha particle or proton released and this is shown in Table I in the "loss" column, as the fraction of events not counted in the peak.

The gamma flux was estimated from the counts recorded by the standard brass Geiger counter, which was placed some distance directly behind the chamber. This, together with the intensity ratio $I(17.6)/I(14.8) = 1.6/1$ at 0° , defined the flux of each component at the monitor. Corrections were then applied for absorption by the chamber walls (about 8% per single wall thickness) and for the inverse square law, the distance from the target to chamber axis being $21\frac{1}{2}$ cm, giving a mean flux believed correct to $\pm 10\%$.

Thus, finally,

$$\sigma(h\nu) = \frac{\text{events observed} + \text{wall loss}}{\left(\frac{h\nu\text{-Mev quanta/cm}^2 \text{ at the}}{\text{mean square distance}} \right) \times \left(\frac{\text{number of atoms of the isotope}}{\text{of neon in the sensitive volume}} \right)}$$

The cross-section values for the higher-energy peaks are considered to be accurate to $\pm 20\%$ while the relative values should be considerably more accurate. For the sake of consistency Table I contains data obtained only with the gridded ionization chamber. The smaller proportional counter containing pure neon at lower pressure gave values within 20% of the values listed, but was useful only for (γ, α) reactions which released more than 5-Mev energy in the counter.

(c) *Variation of Cross Sections with Gamma-Ray Energy.*

In view of the relatively large photodisintegration yields, particularly from the $\text{Ne}^{20}(\gamma_{17.6}, p)\text{F}^{19}$ reaction, obtained with the gridded ionization chamber, an attempt was made to examine the variation in cross sections with change in gamma-ray energy. By using thin lithium targets, less than 10 kev in the vicinity of the 440-kev resonance and about 30 kev thick away from the resonance, the energy of the sharp gamma-ray line could be taken from 17.59 to 18.03 Mev as the proton-bombarding energy was raised from 400 to 900 kev. The ratio $I(17.6)/I(14.8)$ varies quite sharply at the 440-kev resonance (Devons and Hine 1949) but unfortunately the behavior is not known very precisely so that the interpretation of the monitor counter data was somewhat uncertain. At higher proton energies towards 1 Mev there is also a considerable yield of $\frac{1}{2}$ -Mev radiation from $\text{Li}^7(p, p')\text{Li}^7$ (Kraus 1954), but the thick-walled brass counter is relatively insensitive to this.

Three parts of the photodisintegration pulse spectrum were examined corresponding to the 4.7-Mev group, C1, arising from $\text{Ne}^{20}(\gamma_{17.6}, p)\text{F}^{19}$; the 6-Mev group, A13, arising from $\text{Ne}^{20}(\gamma_{17.6}, \alpha)\text{O}^{16*}$; and the region between 2.5 and 3 Mev attributed to reaction A13, $\text{Ne}^{20}(\gamma_{14.8}, \alpha)\text{O}^{16*}$ (i.e. excited state transition). The photodisintegration yields per microcoulomb of bombarding protons in the vicinity of the resonance for the C1 and A13 groups followed moderately well that expected from the intensity of the 17.6-Mev radiation component according to Devons and Hine (1949). No sharp fluctuation in these yields was observed as the radiation energy was raised to 18 Mev, indicating that no sharp photodisintegration resonance occurs in this energy range. However, the data showed that the relative size of the C1 to A13 group fell quite significantly as the gamma-ray energy was raised.

No photodisintegrations were observed when the chamber was irradiated with 6- and 7-Mev gamma radiation resulting from the proton bombardment of fluorine targets in accord with the data of Woods (1952), who showed that $\sigma(\gamma, \alpha)$ was less than $4 \cdot 10^{-30} \text{ cm}^2$ at this energy.

5. DISCUSSION OF RESULTS

The alpha spectrum shows no evidence for any alpha groups which might correspond to transitions to low-lying excited states of O^{16} , confirming the

current view that the lowest excited level in this nucleus lies at 6.06 Mev above the ground state.

The values found for the (γ, α) cross sections are in agreement with what might be expected according to the selection rules deduced by Gell-Mann and Telegdi (1953), on the basis of the charge invariance of nuclear forces, for the photodisintegration of an even-even nucleus such as ${}_{10}\text{Ne}^{20}$ with $T_z = 0$, in which the ground state is an 0^+ state and all levels up to an excitation of about 11 Mev have isotopic spin zero. Electric dipole absorption of radiation of the energies used in this experiment would result in 1^- levels with $T = 1$. Direct transitions from such levels by alpha emission to the ground state of O^{16} , $T = 0$ are forbidden by the isotopic spin selection rule. Absorption into $T = 0$ states is possible by an $M1$ transition but this leads to 1^+ states which cannot proceed to the 0^+ ground state of O^{16} , nor to the first-excited state of O^{16} at 6.06 Mev which is also 0^+ , via alpha emission, without violating the conservation of angular momentum and parity. Thus $\text{Ne}^{20}(\gamma, \alpha)\text{O}^{16}$ ground state transition at these energies proceeds most likely by $E2$ absorption through a 2^+ compound state with $T = 0$. The formula of Weisskopf (Blatt and Weisskopf 1952), which provides an estimate of the upper limit to be expected for the cross section for absorption of $E2$ radiation of 17.6-Mev energy, gives 1.3 millibarns. The experimental value of 0.05 is satisfactorily less than this theoretical limit. It is also to be noted that the cross section for $\text{Ne}^{22}(\gamma_{17.6}, \alpha)\text{O}^{18}$ is considerably greater, as would be expected since no isotopic spin selection rules impose restrictions in this case.

Again $\text{Ne}^{20}(\gamma, \alpha)\text{O}^{16*}$ transitions to the excited levels of O^{16} at 6.14 Mev (3^-), 6.91 Mev (2^+), and 7.12 Mev (1^-), which are all $T = 0$ levels, cannot proceed via 1^- ($T = 1$) states in Ne^{20*} formed by $E1$ absorption, if isotopic spin is conserved. However, these levels are accessible from 1^+ or 2^+ states in Ne^{20*} formed by $M1$ and $E2$ absorption respectively. The Weisskopf formula gives, for $M1$ absorption, a cross-section limit of 8.5 millibarns for 17.6-Mev radiation. The larger cross section observed as compared with the ground state transition is presumably the result of the $M1$ absorption process. The observed factor of three larger intensity of the transitions to the 7-Mev state as compared with the 6.14-Mev state may be a result of the smaller orbital angular momentum of the emitted alphas in the transitions to the 7-Mev states. It is very unlikely that a significant fraction of the counts in the peak corresponding to an energy release of 5.9 Mev in the chamber arise from reaction $D1$, i.e. $\text{Ne}^{20}(\gamma_{17.6}, 2\alpha)\text{C}^{12}$ as this is forbidden in the same way as the transition to the ground state of O^{16} .

The mean (γ, α) cross sections for the broad 14.8-Mev component of the radiation show the same trends and are of similar magnitudes to those for the sharp 17.6-Mev component. The actual cross sections are a little larger for the 14.8-Mev radiation, an indication perhaps of the general trend of (γ, α) cross section with gamma-ray energy in this region.

The large $\text{Ne}^{20}(\gamma, p)\text{F}^{19}$ cross section must arise from transitions from 1^- levels in Ne^{20*} following $E1$ absorption. The observed cross-section value would suggest a cross section for the inverse reaction, with about 5-Mev

proton-bombarding energy, of 0.4 millibarn, which is of the order of magnitude that might be expected from a reasonable extrapolation of Sinclair's (1954) data. There is presumably a comparable (γ, n) cross section for the 17.6-Mev radiation, although the Q for the neutron reaction is -16.9 Mev. It would be expected too that the $\text{Ne}^{22}(\gamma, n)\text{Ne}^{21}$ process would be the main method of breakup of the Ne^{22*} compound nucleus, rather than the (γ, α) process observed in this experiment.

These results provide rather satisfactory confirmation of the operation of isotopic spin selection rules in the photodisintegration of Ne^{20} . The $\text{Ne}^{20}(\gamma, p)\text{F}^{19}$ cross section is about 10 times as large as the (γ, α) cross section, a result similar to that found in the photodisintegration of other light nuclei.

ACKNOWLEDGMENTS

It is a pleasure to acknowledge the interest and encouragement of Professor E. W. Titterton in this work. One of us (J. B. W.) is grateful to the Royal Society and Nuffield Foundation for the award of a bursary which made his stay at the Australian National University possible.

REFERENCES

- AJZENBERG, F. and LAURITSEN, T. 1955. *Revs. Modern Phys.* **27**, 77.
 BARNES, C. A., CARVER, J. H., STAFFORD, G. H., and WILKINSON, D. H. 1952. *Phys. Rev.* **86**, 359.
 BLATT, J. M. and WEISSKOPF, V. F. 1952. *Theoretical nuclear physics* (Chapman & Hall, Ltd.), p. 654.
 BUNEMANN, O., CRANSHAW, T. E., and HARVEY, J. A. 1949. *Can. J. Research, A*, **27**, 191.
 DEVONS, S. and HINE, M. G. N. 1949. *Proc. Roy. Soc. A*, **199**, 56, 73.
 ENGLISH, W. N. and HANNA, G. C. 1953. *Can. J. Phys.* **31**, 768.
 ERDMAN, K. L. and BARNES, C. A. 1953. *Proc. Roy. Soc. (Canada), A*, **47**, 131.
 ERDMAN, K. L. 1953. Ph.D. Thesis, University of British Columbia, Vancouver, B.C.
 FOWLER, W. A. and LAURITSEN, C. C. 1949. *Phys. Rev.* **76**, 314.
 GELL-MANN, M. and TELEGI, V. L. 1953. *Phys. Rev.* **91**, 169.
 KRAUS, A. A. 1954. *Phys. Rev.* **93**, 1308.
 PRESTON, M. A. 1950. *Phys. Rev.* **80**, 307.
 SEALE, R. L. 1953. *Phys. Rev.* **92**, 389.
 STEARNS, M. B. and McDANIEL, B. D. 1951. *Phys. Rev.* **82**, 450.
 SINCLAIR, R. M. 1954. *Phys. Rev.* **93**, 1082.
 WHITEHOUSE, W. J. and GALBRAITH, W. 1950. *Phil. Mag.* **41**, 429.
 WILKINSON, D. H. 1950. *Ionisation chambers and counters* (Cambridge University Press).
 WILLARD, H. B., BAIR, J. K., KINGTON, J. D., HAHN, T. M., SNYDER, C. W., and GREEN, F. P. 1952. *Phys. Rev.* **85**, 849.
 WOODS, S. B. 1952. Ph.D. Thesis, University of British Columbia, Vancouver, B.C.

ELECTRICAL BREAKDOWN IN XENON AND KRYPTON AT ULTRAHIGH FREQUENCIES¹

H. M. BRADFORD, D. M. FRASER, G. F. O. LANGSTROTH,²
AND A. D. MACDONALD

ABSTRACT

Breakdown electric fields have been measured in a resonant cavity for xenon and krypton gases in the pressure range of 0.05 to 100 mm of mercury, at a frequency of 2800 Mc/sec. Extensive precautions were taken to ensure gas purity.

INTRODUCTION

Measurements of the electric fields which cause breakdown in gases have been used during the past decade to investigate the nature of the collision processes which occur when a high-frequency field is applied to a gas (Herlin and Brown 1948; MacDonald and Brown 1949; MacDonald and Betts 1952). This paper presents experimentally determined values of breakdown electric fields for xenon and krypton gases of high purity.

EXPERIMENT

The experimental apparatus is similar to that used in previous investigations (Herlin and Brown 1948; MacDonald and Betts 1952). A block diagram of the microwave equipment is shown in Fig. 1. Power generated by a CW magnetron

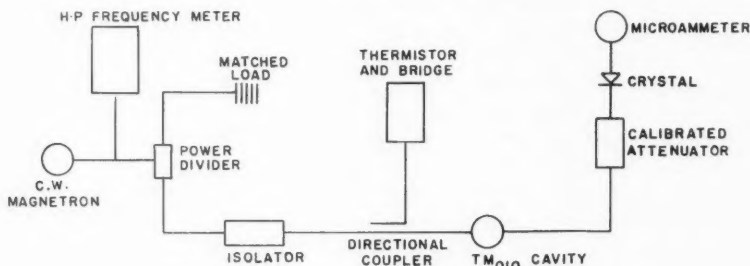


FIG. 1. Block diagram of the microwave apparatus.

operating at 2800 Mc/sec travels through a coaxial transmission line to a cylindrical cavity resonant in the TM_{010} mode. The power divider permits variation of the power reaching the cavity, and the directional coupler diverts a small, known fraction of this power to a thermistor and bridge. The directional coupler, thermistor, and bridge are replaced by a slotted section and

¹Manuscript received July 17, 1959.

Contribution from the Department of Physics, Dalhousie University, Halifax, Nova Scotia. Supported by the Defence Research Board of Canada (Grant 9512-09).

²Holder of a National Research Council Studentship.

microwave receiver when the cavity Q is being measured. During the actual breakdown measurements, the attenuator, crystal, and meter, which are calibrated against the thermistor immediately before each run, are used to indicate power levels. The electric field strength is determined from measurements of the power incident on the cavity, the cavity Q , and the voltage standing wave ratio at resonance, along with the known field configurations (Brown and Rose 1952; Rose and Brown 1952).

The resonant cavity in which breakdown takes place must be highly evacuated before admitting the gas, in order to ensure gas purity. The vacuum system used is represented by a block diagram in Fig. 2. It incorporates many

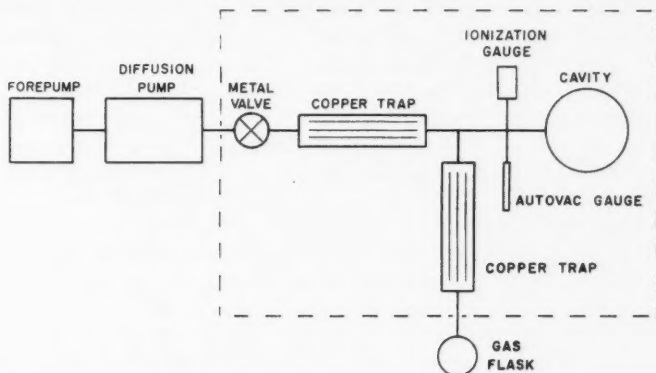


FIG. 2. Block diagram of the vacuum system. The dashed line encloses those parts which are baked in the oven.

of the techniques suggested by Alpert (1953, 1954). The resonant cavity is made of oxygen-free high-conductivity copper and is connected to the pyrex system through Kovar seals. Isolation from the pumps is accomplished through the use of a metal valve, connected by glass-metal seals and capable of withstanding baking at about 400° C. Copper foil traps are used instead of cold traps. The ionization gauge is of the Bayard-Alpert type, and ion pumping is used to obtain the lowest pressures. The pressure of the gas during the breakdown measurement is determined by means of an Autovac hot wire gauge. This gauge is used because it does not introduce vapors into the system as would manometers or McLeod gauges. Calibration of the hot wire filaments against a McLeod gauge, using a sample of the gas under study, was performed before and after each breakdown run, in order to take account of the changes occurring in the filaments during the baking of the vacuum system.

The pressure in the system, before introduction of the gas, could be kept at less than 10^{-8} mm of mercury, while isolated from the pumps. The gases used were of reagent grade, supplied by the Air Reduction Company. A sample from each flask used was taken during the breakdown measurements and analyzed in a mass spectrometer (Consolidated Electrodynamics Model 21-620).

The only impurities found in the samples of krypton used in the measurements labelled "pure krypton" in Fig. 3 were in quantities near the lower limit of detectability of the mass spectrometer. These impurities were:

- O₂—less than 5 parts in 10⁵,
- H₂O—less than 5 parts in 10⁴,
- N₂—less than 5 parts in 10⁴ (in one sample only).

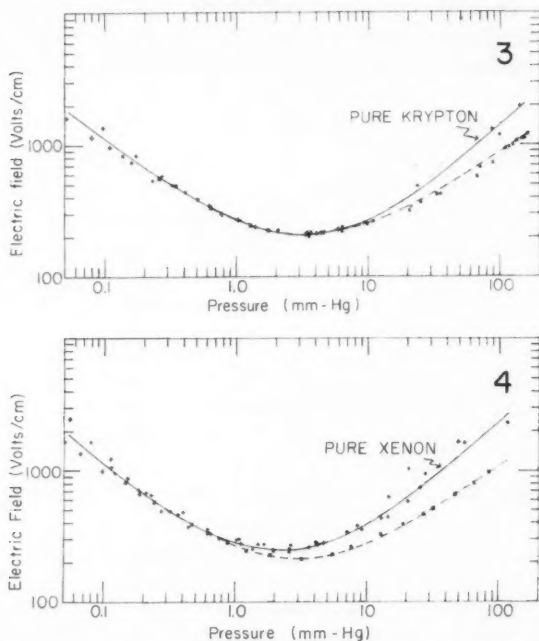


FIG. 3. The breakdown electric field for krypton gas at a frequency of 2800 Mc/sec and a characteristic diffusion length, Λ , of 0.101 cm.

FIG. 4. The breakdown electric field for xenon gas at a frequency of 2800 Mc/sec and a characteristic diffusion length, Λ , of 0.101 cm.

Impurities in the gases used for the "pure xenon" data of Fig. 4 were again in most cases near the limit of detectability, but there was more variation from sample to sample. Impurities found were as follows:

N₂ varied from less than 3 in 10⁴ to 1 in 10³,

H₂O varied from less than 5 in 10⁵ to 5 in 10⁴;

and in addition,

one sample contained traces of Ar and Kr;

one sample contained less than 1 in 10⁴ of H₂ and of CH₄;

a third sample contained less than 1 in 10⁴ of O₂ and less than 2 in 10⁵ of CH₄.

No other impurities were found.

RESULTS AND DISCUSSION

The breakdown field, that is, the electric field which makes a gas start to glow and become conducting, is presented in Fig. 3 for krypton and in Fig. 4 for xenon. In both cases the field is shown for pressures from 0.05 to 100 mm of mercury. The cylindrical cavities in which the experiments were done had a height of 0.318 cm and a characteristic diffusion length, Λ , of 0.101 cm. The measurements were made at 2800 Mc/sec, which was the resonant frequency of the lowest magnetic mode of the cavities used.

In both figures the solid lines represent the mean values of several sets of data on samples of the high-purity gas. For these measurements preliminary evacuation of the cavity to a pressure of the order of 10^{-8} mm of mercury is attained before introducing the gas to the system. The dashed lines in both figures represent the data for sets of measurements made in a system which was only partly bakable and which used alcohol-dry ice vapor traps. (Liquid nitrogen traps cannot be used because of the high boiling temperatures of xenon and krypton.) The preliminary evacuation in this case was to a pressure of about 10^{-4} mm of mercury, and the pressures of the gas during the breakdown runs were measured with Octoil manometers. We do not have mass spectrometer analyses for this latter case, but it may be assumed that there was some contamination of the gas by the system, because of the conditions described, even though reagent grade gases were used.

It is to be noted that the impurities appreciably alter the breakdown field at high pressure in the case of xenon, and to a lesser extent for krypton, while at pressures lower than about 3 or 4 mm of mercury there is no effect. This difference in the breakdown fields may be caused by air impurity, but consideration of the ionization potentials and known reactions of the major components of air does not suggest a process whereby it might happen. At any rate the experiments show that to obtain the breakdown fields characteristic of pure krypton and pure xenon, the system in which the measurements are made must be completely bakable and not contain sources of vapors.

The electric fields have been measured to an accuracy of better than 5% in all cases. As noted above, it was necessary to use a Pirani-type gauge in the measurement of pressure when obtaining the high-purity data. At both the high-pressure and the low-pressure ends of the range this gauge becomes inaccurate. Between 0.5 and 5.0 mm of mercury, pressures were measured to 2% for each point. Below this range each point has an accuracy of about 10% while above it each point has an accuracy of about 20%. Because the curves drawn represent the averages of several sets of points, the over-all accuracy is somewhat better and we estimate that the error in the breakdown curves does not exceed 5% for pressures less than 5 mm of mercury, nor 10% for pressures above this value.

ACKNOWLEDGMENTS

The authors wish to express their thanks to Dr. W. D. Jameison and Dr. C. R. Masson of the Maritime Regional Laboratory of the National Research Council for doing the mass spectrometer analyses.

REFERENCES

- ALPERT, D. 1953. *J. Appl. Phys.* **24**, 860.
——— 1954. *J. Appl. Phys.* **25**, 202.
BROWN, S. C. and ROSE, D. J. 1952. *J. Appl. Phys.* **23**, 711.
HERLIN, M. A. and BROWN, S. C. 1948. *Phys. Rev.* **74**, 291.
MACDONALD, A. D. and BROWN, S. C. 1949*a*. *Phys. Rev.* **75**, 411.
——— 1949*b*. *Phys. Rev.* **76**, 1634.
MACDONALD, A. D. and BETTS, D. D. 1952. *Can. J. Phys.* **30**, 565.
ROSE, D. J. and BROWN, S. C. 1952. *J. Appl. Phys.* **23**, 719.

THE 0-0 AND 1-0 BANDS OF THE $A(^3\Pi_i)-X(^3\Sigma^-)$ SYSTEM OF NH^1

R. N. DIXON²

ABSTRACT

NH molecules have been produced during the flash photolysis of HNCO , and the 0-0 and 1-0 bands of the $A(^3\Pi_i) \leftarrow X(^3\Sigma^-)$ system have been photographed in absorption in the third order of a 21-foot concave grating spectrograph. The intensity distribution in the bands showed that the molecules were approximately at room temperature. The lines of lowest J value are identified for 25 branches of the 0-0 band and 19 branches of the 1-0 band. The analysis of the 0-0 band leads to a correction of the published line assignments for this band. The spin splittings in both the A and X electronic states, and the Λ -doubling in the A state, are considered in detail. Wavelengths in air are given for lines of astro-physical interest.

A. INTRODUCTION

The 3360-Å bands, $A(^3\Pi_i)-X(^3\Sigma^-)$, of the NH molecule were first described by Eder (1893), and have been the subject of many subsequent investigations. Funke (1935, 1936) has published extensive assignments for the lines of the 0-0 and 1-1 bands. Recently Pannetier and Guenebaut (1958) have observed the 1-0 and 0-1 bands of the system in emission from an "atomic flame", but with only moderate resolution.

The determination of accurate vibrational and rotational constants for this system is unfortunately hampered for several reasons: (i) The internuclear distances and vibration frequencies in the two electronic states are very similar, and therefore bands with $\Delta v \neq 0$ are very weak on account of the Franck-Condon principle; in addition the Q branches of the 0-0 and 1-1 bands are confined to very narrow spectral regions with consequent overlapping, and it is difficult to make unambiguous assignments. (ii) When the spectrum is observed in emission from a flame it is very difficult to observe the region of the $\Delta v = +1$ sequence as there is an extensive OH spectrum at this wavelength. (iii) Although the Q branch assignments of the bands can be checked if satellite branches ($\Delta N \neq \Delta J$) are observed, the satellite branches are very weak except at the lowest J values, on account of the rapid transition of the $A(^3\Pi_i)$ state from Hund's coupling case (a) to case (b). In high-temperature spectra the low J levels are not highly populated, and very few satellite lines have been observed. Difficulties (ii) and (iii) could be overcome if the NH bands were obtained with a low rotational temperature.

In the present work NH molecules have been produced at room temperature and the 0-0 and 1-0 bands have been photographed in absorption.

¹Manuscript received July 10, 1959.

Contribution from the Division of Pure Physics, National Research Council, Ottawa, Canada.

Issued as N.R.C. No. 5353.

²National Research Council Postdoctorate Fellow 1957-59. Present address: Department of Physical Chemistry, The University, Sheffield 10, England.

B. EXPERIMENTAL

NH molecules were produced during the flash photolysis of isocyanic acid vapor, HNCN, using an apparatus similar to that described by Callomon and Ramsay (1957). The spectrum was observed under the same experimental conditions as the NCO spectrum (Dixon 1959). The absorption produced in a 6-meter path length through the reaction tube was photographed in the third order of a 21-foot concave grating spectrograph using Eastman Kodak I-O plates, with a resolving power of about 200,000. The 0-0 band of the $A(^3\Pi_i) \leftarrow X(^3\Sigma^-)$ system was extremely strong, and the 1-0 band appeared with about 2% of the intensity of the 0-0 band. The 1-0 band was partially overlapped by a weaker band due to the NCO radical, but the lines of the two bands were easily identified on account of the large ratio (~ 40) of the rotational constants of the two molecules. A few lines of the $^2\Sigma^+ \leftarrow ^2\Pi_{3/2}$ component of the 3064-Å OH band were also observed, but these lay outside the region of the 1-0 NH band.

A hollow-cathode iron arc lamp was used for wavelength calibration. The wavelengths of the reference lines were taken from the M.I.T. tables (Harrison 1939) and used with Edlén's (1952) vacuum corrections. One plate of the 0-0 band and two of the 1-0 band were each measured twice on a comparator equipped with a photoelectric scanning device similar to that described by Tomkins and Fred (1951). The relative accuracy of the frequencies of strong sharp lines is $\pm 0.03 \text{ cm}^{-1}$.

C. ROTATIONAL ANALYSIS

Theory predicts that a $^3\Pi_{(a)}-^3\Sigma^-$ band should have a total of 27 branches, and their lines of lowest N value are illustrated in Fig. 1. Of these, nine are main branches ($\Delta N = \Delta J = 0, \pm 1$) and correspond to the nine strong branches allowed for a $^3\Pi_{(a)}-^3\Sigma^-$ band. For the $A(^3\Pi_i)$ state of NH the transition from Hund's coupling case (a) to case (b) is very rapid with increasing rotation, as $Y = A/B$ is small (~ -2); the remaining 18 satellite branches are therefore very weak except at the lowest N values. In previous analyses only two satellite branches have been observed (Funke 1935, 1936). In the present investigation the first line has been identified for 25 of the 27 branches of the 0-0 band, and for 19 of the branches of the 1-0 band.

The lines of medium N value in the P and R branches of the 0-0 band form close triplets and were easily identified. With the $\Delta_2 F''(N)$ values obtained from these branches it was possible to assign the O , Q , and S branches, and then the P and R lines of low N . The assignments are indicated in Fig. 2. The Q branches of the 1-0 band are more degraded than those of the 0-0 band and were readily identified with the assistance of satellite lines, even though no O or S branches were observed. The assignments for the two bands are given in Tables I and II. For the 0-0 band these differ consider-

ably from the assignments given by Funke (1935, 1936), notably for the Q branches and for the P and R branches at low N value. On the basis of the present assignment it was possible to reassign Funke's measurements of the high N lines. These are given in Table III, and will be used below in the discussion of Λ -doubling. A comparison of the rotational structures of the 1-1 band reported by Funke and the 1-0 band reported here shows that Funke has correctly analyzed the 1-1 band apart from a few errors at low N .

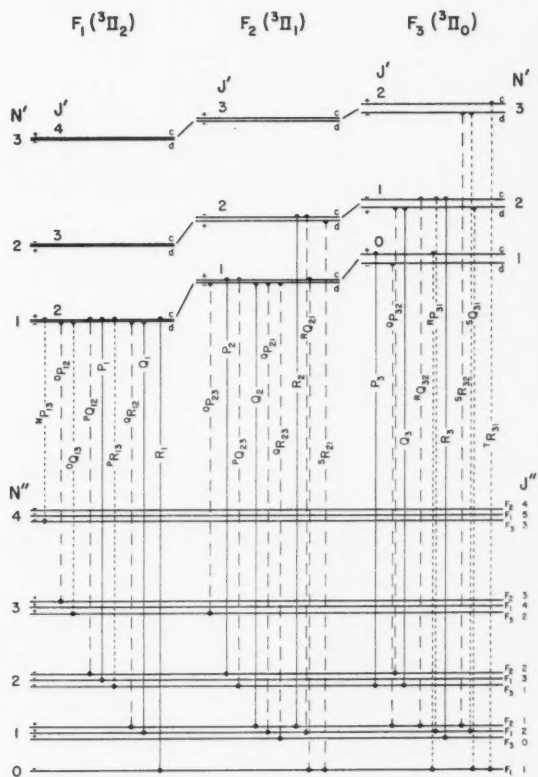


FIG. 1. Energy level diagram and first lines of a $^3\Pi_1-^3\Sigma^-$ transition.

TABLE I
Vacuum wave numbers and line assignments for the 0-0 band of NH, $A^3\Pi_1 \leftarrow X(^2\Sigma^-)$

N	oP_{12}	oQ_{13}	oP_{23}	PQ_{12}	PR_{13}	P_1	P_2	PQ_{23}	P_3	qR_{12}	Q_1	Q_2	qR_{23}
0	—	—	—	—	—	—	—	—	—	—	—	—	—
1	—	—	—	—	—	—	—	—	—	—	—	—	—
2	—	—	—	—	—	—	—	—	—	—	—	—	—
3	29,573.07	29,574.02	29,610.95	29,671.80	29,672.93*	29,672.93*	29,708.57	29,709.70	29,729.35	29,737.24	29,738.09	29,773.37*	29,775.02
4	515.25	516.12	539.99	(645.63)	646.76	618.16	635.13	671.50	683.98	743.54	744.49	767.41	768.45*
5	454.14	—	—	617.05	—	588.37	601.15	635.95	645.63*	747.16	748.23	764.15	765.07*
6	392.00	—	—	587.90	—	557.97	568.03	601.91	609.72	749.35	750.51*	762.12*	(763.07)
7	—	—	—	556.73	—	527.32	538.47	568.73	575.24	(750.51)	751.84	760.82*	761.55
8	—	—	—	526.04	—	496.58	503.31	536.10	544.12	(751.47)	752.74	759.70	760.42
9	—	—	—	495.24	—	465.90	471.52	508.07	511.64	752.94*	752.94*	757.64	758.67
10	—	—	—	—	—	435.31	440.05	476.18	483.12	(752.74)	752.74	756.55	757.64
												755.32	

N	qP_{21}	qP_{32}	Q_3	R_1	R_2	RQ_{21}	RQ_{32}	R_3	κP_{11}	sR_{21}	sR_{32}	sQ_{31}
0	—	—	—	29,770.61*	—	29,807.26	—	—	29,826.95	29,866.08	—	(29,881.45)
1	29,774.07	29,766.18	—	809.80	29,833.76	834.63	(29,846.22)	29,848.02	847.08	928.17	29,939.60	940.47
2	768.45*	782.82	29,783.92	(846.22)	863.33	894.30	872.91	874.01	—	991.28	30,000.76	30,001.73
3	765.07*	776.44	777.37	881.24*	894.09	925.15	901.89	902.84	—	30,054.73	062.77	—
4	763.20	772.59	(773.37)	915.16	925.33	926.44	931.86	932.71	—	118.07	125.05	—
5	(762.12)	769.92	(770.61)	948.41	956.07	957.84	962.23	962.98	—	181.01	187.19	—
6	(760.82)	767.70	(768.45)	981.07	987.90	989.13	992.69	993.35	—	243.43	—	—
7	—	—	766.62	30,013.15	30,018.89	30,020.19	30,023.04	30,023.66	—	—	—	—
8	—	—	(763.07)	044.69	049.54	—	—	053.73	—	—	—	—
9	—	—	—	075.64	079.78	—	—	083.48	—	—	—	—
10	—	—	—	105.99	109.56	—	—	112.83	—	—	—	—

*Overlaps a weaker line. () Overlapped by a stronger line.

TABLE II
Vacuum wave numbers and line assignments for the 1-0 band of NH, $A(^3\Pi_2) \leftarrow X(^1\Sigma^-)$

N	PQ_{12}	PQ_{10}	P_1	P_2	PQ_{23}	P_3	QR_{12}	Q_1	Q_2	QR_{23}	QP_{21}	QP_{13}	Q_3
0	—	—	—	—	—	—	—	—	—	—	—	—	—
1	—	—	—	—	—	—	—	—	—	—	—	—	—
2	32,704.03	(32,705.87)	32,705.87*	32,741.64	32,742.78	(32,762.83)	—	32,771.11	32,806.29	32,808.05	32,807.03	32,829.38	32,814.31
3	675.79	(676.02)	676.76	700.80	701.68*	714.48	—	774.52	797.61	798.75*	813.27*	802.47	(803.40)
4	642.66	—	643.76	660.94	661.83	671.51	—	773.69*	789.99	—	—	—	793.42
5	906.96	—	908.06	921.01	—	929.75	—	770.17*	782.04	—	—	—	783.13
6	—	—	570.21	580.37	—	587.82	—	764.03	(773.43)	—	—	—	771.97
7	—	—	—	—	—	—	—	755.93	(763.17)	—	—	—	759.68*
8	—	—	530.61	—	—	—	—	746.91	751.67*	—	—	—	—
9	—	—	—	—	—	—	—	—	—	—	—	—	—
10	—	—	—	—	—	—	—	—	—	—	—	—	—

N	R_1	R_2	RQ_{21}	RQ_{32}	R_3	RP_{31}
0	32,803.61*	—	32,840.30	—	—	32,860.29
1	839.83	32,864.02	864.90	32,876.73	32,878.61	877.64
2	871.84	889.13	890.13	898.92	900.03	—
3	900.81	913.95	914.96	921.87	922.85	—
4	927.32	937.70	938.79	944.43	945.22	—
5	951.63	960.04	—	—	960.52	—
6	973.84	980.80	—	—	986.41	—
7	993.95	999.79	—	—	33,004.76	—
8	—	—	—	—	—	—
9	—	—	—	—	—	—
10	—	—	—	—	—	—

*Overlaps a weaker line. () Overlapped by a stronger line.

TABLE III
Vacuum wave numbers and line assignments for the 0-0 band of NH , $A^2\Pi_1 \leftarrow X^2\Sigma^+$, after
Funke (1935, 1936) re-assigned where necessary

N	$P_1(N)$	$P_2(N)$	$P_3(N)$	$Q_1(N)$	$Q_2(N)$	$Q_3(N)$	R_1	R_2	R_3
0	—	—	—	29,738.09	—	—	—	—	—
1	29,672.80	—	—	744.47	29,767.41	29,784.00	846.17*	—	29,874.08
2	646.92*	—	—	748.22	761.11	777.38	881.18	29,803.31	902.89
3	618.22	29,635.01	29,645.65	750.45*	762.26	773.43	915.22	925.24	932.69
4	588.46	601.20	609.71	751.88	760.69	770.65	948.34	956.65	962.96
5	558.07	568.11	575.32	752.8	759.71	768.52	981.01	987.90	993.36
6	527.48	535.55	541.78	753.2	758.61	766.57	30,013.08	30,018.96	30,023.69
7	496.69	503.43	508.82	753.2	757.70	764.98	044.72	049.57	053.75
8	466.00	471.71	476.32	752.8	756.52	763.20	075.70	079.84	083.51
9	435.46	440.20	444.24	752.34	755.48	761.46	105.94	109.47	112.76
10	405.06	409.08	412.70	751.43	753.92	759.71	135.69	138.68	141.56
11	374.84	378.28	381.38	750.3	752.3	757.70	164.61	167.16	169.64
12	344.83	347.85	350.52	749.0	750.45	755.48	192.72	194.89	197.11
13	315.15	317.61	320.03	747.27	748.41	753.3	220.10	221.88	223.76
14	285.64	287.78	289.87	745.31	746.20	750.8	246.53	248.02	249.68
15	256.50	258.19	260.06	742.81	743.55	747.8	272.02	273.22	274.54
16	227.64	228.94	230.53	740.1	740.63	744.49	296.41	297.37	298.51
17	198.92	199.96	201.33	737.03*	737.03*	740.63	319.75	320.36	321.30
18	170.43	171.28	172.36	733.10*	733.10*	737.03	341.79	342.15	342.99
19	142.23	142.77	143.72	728.74*	728.74*	732.17	362.58*	362.58*	363.32
20	114.28	114.49	115.27	723.97	723.73	727.10	381.76*	382.15	382.99
21	86.39*	86.39*	86.94	718.44	717.96	721.29	399.51*	399.51*	399.51*
22	68.52*	68.52*	68.70	712.30	711.62	714.73	415.53*	415.53*	415.53*
23	630.56*	630.56*	630.56*	705.19	704.41	707.42	429.78*	429.78*	429.78*
24	602.57*	602.57*	602.57*	697.21	696.33	699.14	442.65	442.06*	442.06*
25	28,974.50*	28,974.50*	28,974.50*	688.28	687.15	689.94	453.20	452.39*	452.39*
26	946.68	946.03*	946.03*	678.08	676.97	679.65	461.52	460.61*	460.61*
27	918.41	917.41*	917.41*	666.98*	665.43	668.02	467.81	466.59*	466.59*
28	889.56	888.45*	888.45*	653.65	652.81	655.00*	470.95	470.03	470.03
29	860.32	859.06*	859.06*	639.13*	638.19*	640.62*	471.87H	470.03	470.03
30	830.23	—	—	623.39*	622.48*	624.50	470.03*	467.78*	467.78*
31	799.47	798.06*	798.06*	—	—	—	—	—	—
32	767.51	766.22*	766.22*	—	—	—	—	—	—
33	734.52	733.09	732.36	—	—	—	—	—	—
34	—	—	—	—	—	—	—	—	—

Note: H Head. *Blended line.

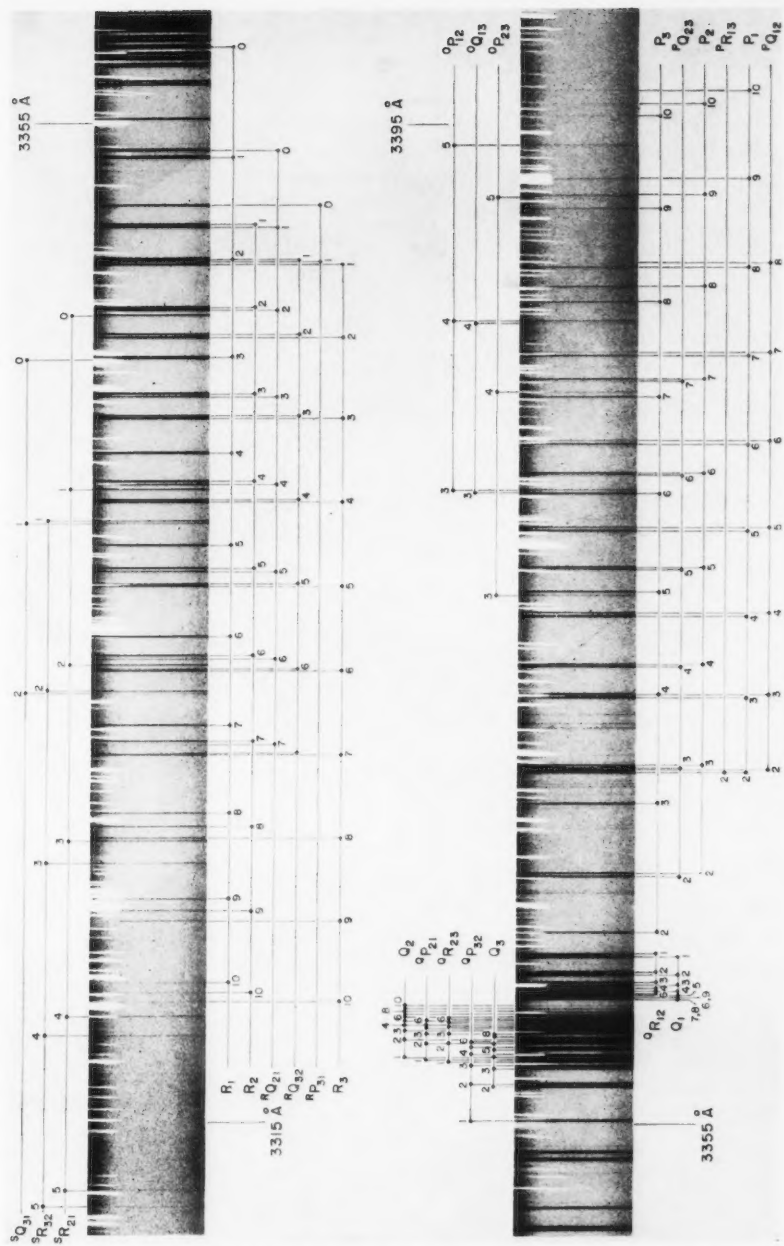


FIG. 2. The 0-0 band of $\text{NH } A(3\Pi_1) - X(3\Sigma^-)$, photographed in absorption in the third order of a 21-foot concave grating spectrograph.

D. CONSTANTS FROM THE 0-0 BAND

1. The Level $X(^3\Sigma^-); v = 0$

A molecule in a $^3\Sigma$ state has three levels for each N value, with $J = N+1$, (F_1); $J = N$, (F_2); and $J = N-1$, (F_3). The triplet splitting has been treated theoretically by Schlapp (1937) and the complete expressions for the rotational term values are given by Herzberg (1950) as:

$$(1) \quad F_1(N) = B_v N(N+1) - D_v N^2(N+1)^2 + \delta_{12}(N),$$

$$(2) \quad F_2(N) = B_v N(N+1) - D_v N^2(N+1)^2,$$

$$(3) \quad F_3(N) = B_v N(N+1) - D_v N^2(N+1)^2 + \delta_{32}(N),$$

where

$$(4) \quad \delta_{12}(N) = -\lambda + (2N+3)B_v - \{(2N+3)^2 B_v^2 + \lambda^2 - 2\lambda B_v\}^{1/2} + \gamma(N+1),$$

$$(5) \quad \delta_{32}(N) = -\lambda - (2N-1)B_v + \{(2N-1)^2 B_v^2 + \lambda^2 - 2\lambda B_v\}^{1/2} - \gamma N.$$

B_v and D_v are effective rotational constants, and γ and λ describe the spin splitting. Thus, the $F_2(N)$ levels follow the simple rotator formula. The constants B_0'' and D_0'' of NH $X(^3\Sigma^-)$ were therefore determined in the usual manner, using least squares, from the 0-0 band combination differences $\Delta_2 F_2''(N)$, obtained from the relations:

$$(6) \quad \Delta_2 F_2''(N) = {}^Q R_{12}(N-1) - {}^Q P_{12}(N+1) = R_2(N-1) - P_2(N+1) \\ = {}^S R_{32}(N-1) - {}^Q P_{32}(N+1).$$

The spin splittings $\delta_{12}''(N)$ and $\delta_{32}''(N)$ were each obtained from six different relationships between the branches of the 0-0 band, either as the separation between two adjacent lines or as the difference between two combination differences (see Fig. 1). From equations (4) and (5) it is seen that:

$$(7) \quad \delta_{12}''(N-1) + \delta_{32}''(N+1) = -(2\lambda'' + \gamma'')$$

and experimentally this sum was found to be essentially constant. λ'' and γ'' were then determined using an iterative process. The calculated splittings for each N value are compared in Fig. 3 with the mean of the experimental values obtained from unblended lines.

The lower state combination differences for the 1-0 band agreed with those for the 0-0 band within the experimental error. The rotational constants for the $X(^3\Sigma^-); v = 0$ level are collected in Table IV.

TABLE IV
Constants for the $X(^3\Sigma^-)$ state of NH

$B_0'' = 16.3454 \pm 0.0015 \text{ cm}^{-1}$	$D_0'' = 16.85 \pm 0.15 \times 10^{-4} \text{ cm}^{-1}$
$\lambda'' = 0.928 \pm 0.007 \text{ cm}^{-1}$	$\gamma'' = -0.053 \pm 0.002 \text{ cm}^{-1}$
$\Delta G''(\frac{1}{2}) = 3125.6 \pm 0.2 \text{ cm}^{-1}$	$\alpha'' = 0.646 \pm 0.002 \text{ cm}^{-1}$

NH is similar to O_2 in having a $^3\Sigma^-$ ground state. In O_2 transitions involving the reorientation of the electron spin ($\Delta N = 0$, $\Delta J = \pm 1$) give rise to a

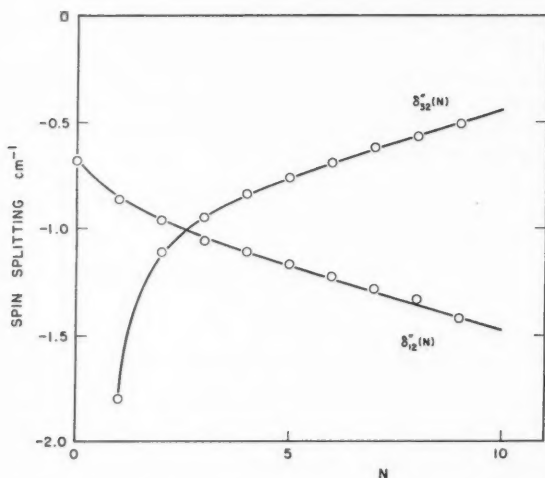


FIG. 3. The observed spin splitting in the $v = 0$ level of the $X(^2\Sigma^-)$ state of NH.

microwave absorption spectrum (Strandberg, Meng, and Ingersoll 1949). The transitions are made possible by the magnetic dipole moment of a molecule in a triplet state. NH should have a similar spectrum, and the frequencies of the lines would be given by $|\delta''_{12}(N)|$ and $|\delta''_{32}(N)|$. Figure 3 shows that the strongest lines would be around 1 cm^{-1} (30,000 Mc/s) if the rotational temperature of the NH molecules were not too high.

2. The Level $A(^3\Pi_i)$; $v = 0$

The $A(^3\Pi_i)$ state of NH tends toward Hund's coupling case (a) at low N and is inverted. Thus there are three substates $^3\Pi_2$, $^3\Pi_1$, and $^3\Pi_0$, the levels of which can be designated F_1 , F_2 , and F_3 respectively. Each of these levels exhibits Λ -doubling. For the labelling of the Λ -doublets we shall follow the c and d nomenclature proposed by Mulliken (1931) and indicated in Fig. 1.

Budó (1936) has given approximate expressions for the rotational term values of a $^3\Pi_{(a)}$ state of intermediate coupling, but these were found to be inadequate for the representation of the levels of NH of moderate N value, where the rotational distortion becomes significant while the state has not yet approached Hund's case (b). Gilbert (1936) has considered the $^3\Pi_{(a)}$ state including the effects of rotational distortion, but neglecting Λ -doubling, and has shown that the term values of the three levels for each J are the roots W of a third-order secular equation:

$$(8) \quad \mathbf{S}^{-1} \mathbf{H}_a \mathbf{S} = \mathbf{W}.$$

Gilbert gives expressions for the elements of \mathbf{H}_a in terms of J and the rotational constants B_v , D_v , and A_v . \mathbf{S} is the unitary transformation matrix which diagonalizes \mathbf{H}_a .

The Determination of B'_0 and D'_0

Although it is not possible to give simple expressions for the individual term values $F_i(J)$ Gilbert has shown that their sum obeys:

$$(9) \quad \sum F_i(J) = B_e\{3J(J+1)-1\} - D_e\{3J^2(J+1)^2 + 12J(J+1) + 5\}.$$

B'_0 and D'_0 can therefore be determined from the sum of the three combination differences $\Delta_2 F'_i(J)$ using the relationship:

$$(10) \quad \frac{\sum \Delta_2 F'_i(J)}{3(J+\frac{1}{2})} = (4B'_e - 22D'_e) - 8D'_e(J+\frac{1}{2})^2$$

where the $\Delta_2 F'_i(J)$ are the mean values of $\Delta_2 F'_{ic}(J)$ and $\Delta_2 F'_{id}(J)$.

Many of the lines in the 0-0 band are overlapped and the following procedure was used to determine the constants of the $^3\Pi$ levels. The term values of the upper state were determined by adding the term value of the appropriate lower level, calculated from the ground state rotational constants in Table IV, to the measured frequency of each line in the band. These were

TABLE V
Constants for the $A(^3\Pi_0)$ state of NH

(a) Constants using the mean energies of the Λ -doublets		
$B'_0 = 16.3221 \pm 0.0020 \text{ cm}^{-1}$	$\alpha' = 0.744 \pm 0.001 \text{ cm}^{-1}$	
$D'_0 = 17.58 \pm 0.15 \times 10^{-4} \text{ cm}^{-1}$	$\beta' = 0.4 \pm 0.1 \times 10^{-4} \text{ cm}^{-1}$	
$A'_0 = -34.72 \pm 0.02 \text{ cm}^{-1}$	$A_1 = -34.74 \pm 0.03 \text{ cm}^{-1}$	
$\nu_{00} = 29,776.76 \pm 0.03 \text{ cm}^{-1}$	$\Delta G'(\frac{1}{2}) = 3034.00 \pm 0.05 \text{ cm}^{-1}$	
$\gamma' = 0.04 \pm 0.005 \text{ cm}^{-1}$		
(b) Constants of the Λ -doubling, and revised values of A'_0 , A'_1 , and ν_{00} when Λ -doubling effects are included		
	$v = 0$	$v = 1$
C_0	$-2.63 \pm 0.02 \text{ cm}^{-1}$	$-2.53 \pm 0.02 \text{ cm}^{-1}$
C_1	$-0.005 \pm 0.005 \text{ cm}^{-1}$	$-0.005 \pm 0.005 \text{ cm}^{-1}$
C_2	$0.0318 \pm 0.0005 \text{ cm}^{-1}$	$0.0293 \pm 0.0010 \text{ cm}^{-1}$
C_3	$-1.30 \pm 0.05 \times 10^{-5} \text{ cm}^{-1}$	$-1.29 \pm 0.10 \times 10^{-5} \text{ cm}^{-1}$
κ_0	$-1.6 \pm 0.3 \text{ cm}^{-1}$	$-1.6 \pm 0.3 \text{ cm}^{-1}$
A'	$-35.02 \pm 0.06 \text{ cm}^{-1}$	$-35.04 \pm 0.06 \text{ cm}^{-1}$
ν_{00}	$29,777.09 \pm 0.05 \text{ cm}^{-1}$	

averaged for each level, using only those values determined from unblended lines. The upper level combination differences were then formed from these term values, and the B'_0 and D'_0 of Table V(a) were determined by the method of least squares using equation (10).

The Band Origin ν_{00}

The band origin was derived from the upper level term values by summing over all levels with the same J and using the above determined values for B'_0 and D'_0 in equation (9). Thus $\nu_{00} = T_i(J) - F_i(J) = 29,976.76 \text{ cm}^{-1}$, on the assumption that the Λ -doubling does not influence equation (9).

The Spin-Coupling Constant A'_0

The coupling constant A for the interaction between the spin and electronic angular momenta of a $^3\Pi_{(d)}$ state may be determined for each value of J from an equation derived by Gilbert:

$$\begin{aligned}
 (11) \quad \frac{1}{4}B^{-2}[3(F_3-F_1)^2 + \{(F_3-F_2) - (F_2-F_1)\}^2] \\
 = 3(Y-2)^2 - 8 + 12J(J+1) - 24\mu J(J+1)\{2J(J+1)+1\} \\
 + 12Y\mu\{2J(J+1)-1\} + 48\mu^2 J^2(J+1)^2\{J(J+1)+1\}
 \end{aligned}$$

where $Y = A/B$, $\mu = D/B$, $J = 2, 3, 4, \dots$. Using this equation a value of A'_0 was calculated for each J value from the mean energy of the $F'_{ic}(J)$ and $F'_{id}(J)$ levels. The values obtained for A'_0 were not constant with J , as is seen in Fig. 4.

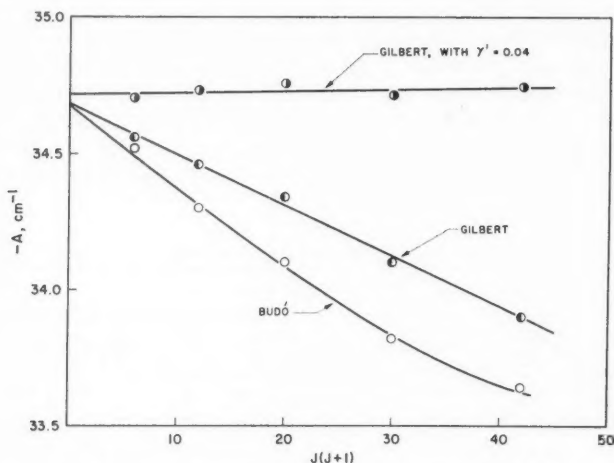


FIG. 4. The spin coupling constant A'_0 for the $v = 0$ level of the NH $A(^3\Pi_i)$ state, showing the variation with J when terms containing γ' are neglected.

Mulliken (1930) has suggested that in addition to the spin splitting of a $^3\Pi_{(d)}$ state given by the coupling constant A there can be further spin-splitting terms $f_i(N)$ as follows:

$$(12) \quad ^3\Pi_2, \quad J = N+1 \quad f_1(N) = \gamma N$$

$$(13) \quad ^3\Pi_1, \quad J = N \quad f_2(N) = -\gamma$$

$$(14) \quad ^3\Pi_0, \quad J = N-1 \quad f_3(N) = -\gamma(N+1)$$

If the upper level term values are modified to take account of such terms it is found that a value of A'_0 that is essentially constant with J can be obtained with $\gamma' = +0.04 \text{ cm}^{-1}$ (Fig. 4). However, this is not necessarily the correct value of A for the level, as it is calculated from the mean energies of the Λ -doublets. This will be discussed below.

Λ -Doubling

The finer interactions of a $^3\Pi$ state with other states of the molecule contribute extra terms ϕ_{ic} and ϕ_{id} to be added to the rotational energy. In general these cause a splitting of the degeneracy of the c and d levels, giving Λ -doubling:

$$(15) \quad \delta_{cd}(N)_i = F_{ic}(N) - F_{id}(N) = \phi_{ic}(N) - \phi_{id}(N).$$

For the low N values these doublings were derived directly from the observed upper level term values, and at high N from Funke's measurements (reassigned) of Table III by the relationship:

$$(16) \quad 2\delta_{cd}(N+\frac{1}{2})_i \simeq \delta_{cd}(N)_i + \delta_{cd}(N+1)_i = R_i(N) - Q_i(N) - Q_i(N+1) + P_i(N+1).$$

The interaction of a $^3\Pi$ state with a $^3\Sigma$ state has been considered in detail by Hebb (1936). The Λ -doublings in each substate $^3\Pi_0$, $^3\Pi_1$, or $^3\Pi_2$ can be given in terms of three constants C_0 , C_1 , and C_2 and the elements S_{ji} of the transformation matrix \mathbf{S} of equation (8). Here, the suffix j refers to the case (a) nomenclature, $j = 1 \equiv ^3\Pi_0$, $j = 2 \equiv ^3\Pi_1$, $j = 3 \equiv ^3\Pi_2$, and the suffix i refers to the elements appropriate to the term value $F_i(J)$. When Hebb's equations were applied to NH it was found that for $J > 10$ there was need of a higher order term in J , and an extra term $C_3J^2(J+1)^2$ was accordingly added. For his calculations Hebb has grouped together levels with the same symmetry for each J value, and for his equations we must use:

$$(17) \quad \delta_1(J) = \delta_{cd}(N = J-1)_1 = F_{1c}(J) - F_{1d}(J),$$

$$(18) \quad \delta_2(J) = -\delta_{cd}(N = J)_2 = F_{2d}(J) - F_{2c}(J),$$

$$(19) \quad \delta_3(J) = \delta_{cd}(N = J+1)_3 = F_{3c}(J) - F_{3d}(J).$$

Thus the Λ -doublings are given by:

$$(20) \quad \delta_i(J) = C_0S_{1i}^2 + C_1[2J(J+1)]^{\frac{1}{2}}S_{1i}S_{2i} + [C_2 + C_3J(J+1)][J(J+1)S_{2i}^2 + 2\frac{1}{2}(J-1)J(J+1)(J+2)]^{\frac{1}{2}}S_{1i}S_{3i}.$$

The constants C_0 , C_1 , C_2 , and C_3 were determined using equation (20) by the method of least squares, making use of the summation:

$$(21) \quad \Sigma \delta_i(J) = C_0 + C_2J(J+1) + C_3J^2(J+1)^2.$$

In Fig. 5 the experimental Λ -doublings are compared with values calculated

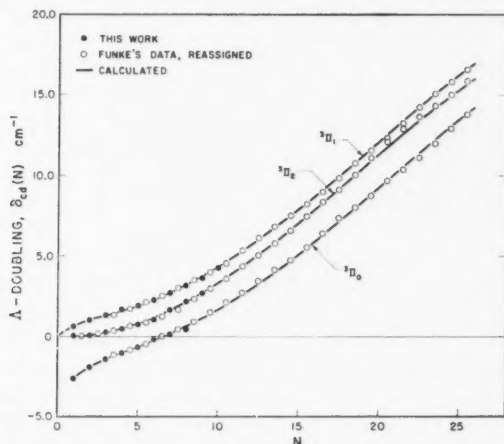


FIG. 5. Λ -doubling, $F_{ic}(N) - F_{id}(N)$, of the $v = 0$ level of NH, $A(^3\Pi_1)$.

according to equation (20) with the constants of Table V(b). The agreement is good, taking into account that in Funke's measurements some of the branches merged at high N values.

If the $A(^3\Pi_i)$ and the $X(^3\Sigma^-)$ states, which are separated by ν cm $^{-1}$, have the same quantum number L of total orbital angular momentum, and are related in the manner that Van Vleck (1929) describes as "pure precession", then the Λ -doubling constants are given by:

$$(22) \quad C_0 = 2\epsilon + \delta + \gamma + 2\alpha + \kappa,$$

$$(23) \quad C_1 = 4\epsilon + \delta,$$

$$(24) \quad C_2 = \epsilon,$$

where:

$$(25) \quad \gamma = A^2 L(L+1)/\nu,$$

$$(26) \quad \delta = 4ABL(L+1)/\nu,$$

$$(27) \quad \epsilon = 2B^2 L(L+1)/\nu,$$

α is a spin-spin interaction constant which Hebb claims is always positive, and κ is a contribution to the Λ -doubling of $^3\Pi_0$ arising from the interaction with $^1\Sigma$ and $^5\Sigma$ states. From the experimental values of C_1 and C_2 and equations (23) and (24) we obtain $\delta = -0.132$ cm $^{-1}$ and $\epsilon = 0.0318$ cm $^{-1}$, compared with $\delta = -0.152$ cm $^{-1}$ and $\epsilon = 0.0358$ cm $^{-1}$ calculated from equations (26) and (27) with $L = 1$. The relationship of "pure precession" is therefore approximately true. The calculated value of $\theta = 2\epsilon + \delta + \gamma$ is extremely small, and C_0 is therefore almost entirely given by $(2\alpha + \kappa)$.

The Spin-Splitting Constant γ'

In the calculation of A'_0 using equation (11) it was found necessary to introduce a spin-splitting constant $\gamma' = +0.04$ cm $^{-1}$ in order to obtain a value of A'_0 that was invariant with J . As the F_2 levels lie approximately half-way between the F_1 and F_3 levels of the same J their term values have little effect on the calculated value of A'_0 . In order to investigate the spin-splitting terms $f_i(N)$ of equations 12 to 14 more fully, with particular reference to $f_2(N)$, the term values for $J = 0$ to $J = 12$ were calculated using equation (8) with the above determined values of B'_0 , D'_0 , and A'_0 . The differences $\frac{1}{2}\{F_{ic}(N) + F_{id}(N)\}_{\text{obs}} - F_i(N)_{\text{calc}}$ are plotted against N in Fig. 6(a). It is seen that neither the curve for $F_2(N)$ nor that for $F_3(N)$ have the expected dependence on N , although the separation between the curves for $F_1(N)$ and $F_3(N)$ does increase with N . Now the Λ -doubling of the $F_3(1)$ level is $C_0 = -2.63$ cm $^{-1}$. If the Λ -doubling is not symmetrical [$\phi_{ic}(N) \neq -\phi_{id}(N)$] not only will this have a marked effect on the residuals of Fig. 6(a) for $F_3(N)$, but it will also lead to an incorrect value of A'_0 , therefore affecting the calculated values of $F_1(N)$ and $F_2(N)$. From Hebb's (1936) equations we can derive the contribution to $\frac{1}{2}\{\phi_{ic}(N) + \phi_{id}(N)\}$ arising from the interaction of the $^3\Pi$ state with $^3\Sigma^-$ states. In addition, Van Vleck (1932) has shown that for Hund's case (a) the $^3\Pi_0$ component can interact with $^1\Sigma$ and $^5\Sigma$

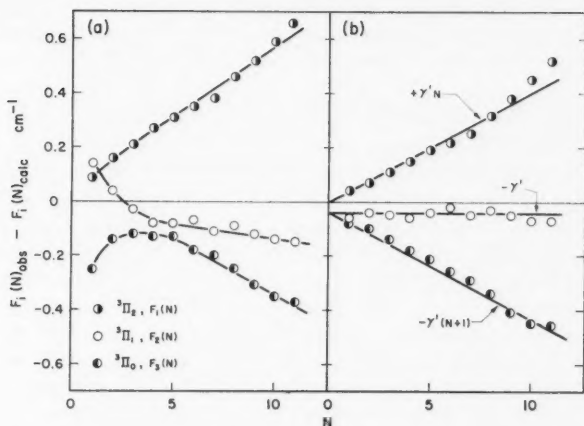


FIG. 6. The difference between the mean energy of the observed rotational term values $F_{ic}(N)$ and $F_{id}(N)$ for the $v = 0$ level of NH, $A(^3\Pi_i)$, and the values calculated: (a) according to equation (8), (b) including the effect of equation (28) with $\kappa_0 = -1.6 \text{ cm}^{-1}$. The full lines in (b) are the $f_i(N)$ of equations 12 to 14 with $\gamma' = 0.04 \text{ cm}^{-1}$.

states, giving the contribution κ to C_0 (equation 22). These same states also cause a shift of the mean energy of the $F_3(1)$ level by $\frac{1}{2}\{\phi_{3c}(1) + \phi_{3d}(1)\} = \frac{1}{2}\kappa_0$. If the $^3\Pi_0$ component interacts with only $^{1,5}\Sigma^+$ states, $\kappa_0 = \kappa$; with only $^{1,5}\Sigma^-$ states, $\kappa_0 = -\kappa$. Thus an extra term is to be added to the expression (8) for the mean energy of $F_{ic}(J)$ and $F_{id}(J)$:

$$(28) \quad \frac{1}{2}\{\phi_{ic}(J) + \phi_{id}(J)\} = \frac{1}{2}\kappa_0 S_{1t}^2 - C_2 S_{3t}^2 + \frac{1}{2}\theta(1 - S_{3t}^2) \\ + \frac{1}{4}C_1\{[2J(J+1)]^{\frac{1}{2}}S_{1t}S_{2t} + [2J(J+1) - 4]^{\frac{1}{2}}S_{2t}S_{3t}\} \\ + \frac{1}{2}C_2J(J+1) + \frac{1}{2}C_3J^2(J+1)^2.$$

In the present case $\theta (= 2\epsilon + \delta + \gamma)$ can be neglected, and the last two terms contribute to the effective B_v and D_v values, and can be ignored. Further, the term $-C_2S_{3t}^2$ and the term with coefficient C_1 contribute a maximum of 0.02 cm^{-1} . Thus the term involving κ_0 is dominant. The introduction of κ_0 necessitates a revisal of A'_0 and v_{00} . Various values of κ_0 were tried in an attempt to produce values of $\{\frac{1}{2}(F_{ic} + F_{id}) - F_{i(calc)}\}$ with a dependence on N as predicted by equations 12 to 14. It was found that with $\kappa_0 = -1.6 \pm 0.3 \text{ cm}^{-1}$ and $A'_0 = -35.02 \text{ cm}^{-1}$ this could be achieved simultaneously for all three levels $F_i(N)$, and that $\gamma' = +0.04 \text{ cm}^{-1}$, in agreement with the value postulated above (see Fig. 6 (b)).

If κ is the main contribution to C_0 , then κ and κ_0 are both negative. One might infer from this that the $b(^1\Sigma^+)$ state of NH lies above the $A(^3\Pi_i)$ state, but this conclusion is far from being unambiguous.

Thus it is possible to derive expressions that will represent the observed rotational term values of the $A(^3\Pi_i)$; $v = 0$ level of NH to within the experimental accuracy. These involve the nine rotational constants A'_0 , B'_0 , D'_0 , γ' ,

C_0 , C_1 , C_2 , C_3 , and κ_0 . Although this is sufficient for $J \leq 12$, Funke (1935) has shown that for $J \leq 30$ an additional term $H'_v J^3(J+1)^3$ is needed, where $H'_0 = 5 \times 10^{-8} \text{ cm}^{-1}$.

E. CONSTANTS FROM THE 1-0 BAND

1. The Lower State: $\Delta G''(\frac{1}{2})$ and α''

The lower state vibrational interval $\Delta G''(\frac{1}{2})$ and rotational constant α'' were obtained by plotting the difference in frequency between corresponding lines in the 1-0 band (these measurements) and the 1-1 band (Funke 1935, 1936) against $N''(N''+1)$. Differences from the various branches agreed to within the experimental error, indicating that there is no significant difference between the spin splitting in the two levels $v'' = 0$ and 1. Values of the difference were obtained for $N = 1$ to 7, and within this range the plot gave a straight line, indicating that $D''_1 \simeq D''_0$. From the intercept of the line, $\Delta G''(\frac{1}{2}) = 3125.6 \text{ cm}^{-1}$, and from the slope $\alpha'' = B''_0 - B''_1 = 0.646 \text{ cm}^{-1}$.

2. The Upper State

$\Delta G'(\frac{1}{2})$ and α'

The differences in frequency between lines of the same J' in the 1-0 and 0-0 bands were found to vary from one branch to another. Thus the spin splittings in the $v' = 1$ and $v' = 0$ levels are not identical. The upper level term values for $v' = 1$ were therefore determined in the manner described above for the $v' = 0$ level, and the following relationship was used (cf. equation 9):

$$(29) \quad \frac{1}{6} \left[\sum \{T'_{ic}(J) + T'_{id}(J)\}_{v'=1} - \sum \{T'_{ic}(J) + T'_{id}(J)\}_{v'=0} \right] \\ = \Delta G'(\frac{1}{2}) + (B'_1 - B'_0) \left[J(J+1) - \frac{1}{3} \right] - (D'_1 - D'_0) \left[J^2(J+1)^2 + 4J(J+1) + \frac{5}{3} \right].$$

A plot of the experimental values of the L.H.S. of this equation for $J = 2$ to $J = 7$ against $J(J+1)$ had a definite curvature; therefore $D'_1 \neq D'_0$. The values of $\Delta G'(\frac{1}{2})$, $\alpha' = B'_0 - B'_1$, and $\beta' = D'_1 - D'_0$ given in Table V(a) were determined by the method of least squares.

The Spin-Coupling Constant A'_1

The constant A'_1 was derived from the experimental term values in the manner described above for $v' = 0$, using equation (11). It was again found necessary to postulate a spin-splitting constant $\gamma' = +0.04 \text{ cm}^{-1}$ in order to obtain a value of $A' = -34.74 \text{ cm}^{-1}$ that was invariant with J .

Λ -Doubling

The Λ -doubling of the $v' = 1$ level is only available for $N \leq 7$ from the present analysis of the 1-0 band. However, values for N up to 24 were obtained from Funke's measurements on the 1-1 band, using equation (16). These two sets of values agreed in the region of overlap, and showed a dependence on N very similar to that for the $v' = 0$ level. The constants C_0 , C_1 , C_2 , and C_3 were determined by the methods outlined above and are given in Table V(b). It is seen that the constant C_2 , which determines the main contribution

to the doubling at high N , is appreciably lower than for the $v' = 0$ level. This would be expected on "pure precession" arguments, as B' decreases by the same order of magnitude (see equations 24 and 27).

γ' and κ_0

The differences between the observed term values for $v' = 1$ (mean of c and d levels) and those calculated from equation (8) with the constants determined above (Table V(a)) showed the same dependence on N as is illustrated in Fig. 6(a) for $v' = 0$. Data were only available for $N \leq 8$, and within this range the same constants $\gamma' = +0.04 \text{ cm}^{-1}$ and $\kappa_0 = -1.6 \text{ cm}^{-1}$ as determined for the $v' = 0$ level could explain the deviations for $v' = 1$.

F. APPLICATION TO ASTROPHYSICS

Should NH molecules exist in interstellar space they could be detected by their ultraviolet absorption. These molecules would have a rotational temperature close to 0°K , and the majority would therefore be in the lowest rotational and vibrational level of the ground state (Herzberg 1950, p. 496). It is thus of interest to tabulate the wavelengths in air of those transitions that can arise from this lowest level. This is done in Table VI for the 0-0

TABLE VI
Wavelengths in air and rotational line strengths for the lines of the NH $A(^3\Pi_0) \leftarrow X(^3\Sigma^-)$ system arising from the lowest rotational level ($N=0$, $J=1$) of the ground state

Line	Wavelength in air, Å		Rotational line strength, %*
	0-0 band	1-0 band	
$R_1(0)$	3358.056	3047.558	53.4
$RQ_{21}(0)$	3353.923	3044.151	31.0
$P_{21}(0)$	3351.710	3042.302	11.6
$SR_{21}(0)$	3347.318	3038.971	2.2
$SO_{21}(0)$	3345.590	3037.533	1.8
$TR_{21}(0)$	3335.534	3029.641	0.02

*The relative vibrational transition probability of the 1-0 band is of the order of 2% of that of the 0-0 band.

and 1-0 bands of the $A(^3\Pi_0) \leftarrow X(^3\Sigma^-)$ system. Not all these lines have been observed directly and free from overlapping in the laboratory, but their wavelengths could be calculated using other measured line positions and mean lower level combination differences. The relative rotational line strengths were calculated according to the approximate equations given by Budó (1937). No direct measurement was made of the intensity ratio of the 1-0 and 0-0 bands; this was estimated from the rotational energies of the last lines observed in the P and R branches of the two bands on the assumption that the rotational distribution approximated to that for room temperature. The value of 2% in Table VI is therefore only an order of magnitude.

ACKNOWLEDGMENTS

The author wishes to thank Dr. Herzberg and his colleagues for their encouragement during this work. He is also indebted to the National Research

Council for a postdoctorate fellowship, during the tenure of which this work was carried out. Thanks are also due to Miss L. L. Howe for assisting with the calculations.

REFERENCES

- BUDÓ, A. 1936. *Z. Physik*, **98**, 437.
——— 1937. *Z. Physik*, **105**, 579.
CALLOMON, J. H. and RAMSAY, D. A. 1957. *Can. J. Phys.* **35**, 129.
DIXON, R. N. 1959. *Phil. Trans. Roy. Soc. London* (in press).
EDER, J. M. 1893. *Denkschr. Wien Akad.* **60**, 1.
EDLÉN, B. 1952. *J. Opt. Soc. Am.* **43**, 339.
FUNKE, G. 1935. *Z. Physik*, **96**, 787.
——— 1936. *Z. Physik*, **101**, 104.
GILBERT, C. 1936. *Phys. Rev.* **49**, 619.
HARRISON, G. R. 1939. *M.I.T. wavelength tables* (John Wiley & Sons Inc., New York).
HEBB, M. H. 1936. *Phys. Rev.* **49**, 610.
HERZBERG, G. 1950. *Spectra of diatomic molecules* (D. Van Nostrand Co. Inc., New York).
MULLIKEN, R. S. 1930. *Revs. Modern Phys.* **2**, 107.
——— 1931. *Revs. Modern Phys.* **3**, 95.
PANNETIER, G. and GUENEBAUT, H. 1958. *Bull. soc. chim. France*, 1463.
SCHLAPP, R. 1937. *Phys. Rev.* **51**, 342.
STRANDBERG, M. W. P., MENG, C. Y., and INGERSOLL, J. G. 1949. *Phys. Rev.* **75**, 1524.
TOMKINS, F. S. and FRED, M. 1951. *J. Opt. Soc. Am.* **41**, 641.
VAN VLECK, J. H. 1929. *Phys. Rev.* **33**, 467.
——— 1932. *Phys. Rev.* **40**, 544.

THEORY OF THE PRESSURE-INDUCED ROTATIONAL SPECTRUM OF HYDROGEN¹

J. VAN KRANENDONK AND Z. J. KISS²

ABSTRACT

The theory of induced infrared absorption developed previously is applied to the pressure-induced rotational spectrum of hydrogen. The intensity of the rotational band is due mainly to the quadrupolar induction effect, and to a small interference effect between the quadrupolar and overlap moments. From the experimental data on the binary absorption coefficients, values of the angle-dependent overlap moments are obtained for H_2 -He, H_2 -H₂, H_2 -Ne, H_2 -N₂, and H_2 -A. A calculation of the overlap moment for pure H_2 is presented. Rosen-type wave functions appear to be inadequate for a calculation of the small angle-dependent rotational as well as vibrational overlap moments. The temperature dependence of the binary absorption coefficient is calculated, taking into account the quantum effects in the pair distribution function, and found to be in good agreement with the experimental data. The dependence on the ortho-para ratio is also discussed. The double rotational line $S(1)+S(1)$ has been observed and its intensity measured.

1. INTRODUCTION

The pressure-induced rotational spectrum of hydrogen has recently been studied experimentally in compressed gases (Kiss, Gush, and Welsh 1959), as a function of the density and the temperature of the gas, and for various ortho-para ratios. This spectrum has been investigated independently by Colpa and Ketelaar (1958*a, b*). Calculations of the binary absorption coefficients of the rotational spectrum, which were based on the quadrupolar induction effect and on classical statistics for the pair distribution function, have been published (Kiss *et al.* 1959; Colpa *et al.* 1958*b*). In the present paper the calculation of the binary absorption coefficient is extended to lower temperatures by taking into account the quantum effects in the pair distribution function, and the contribution of the overlap induction effect to the intensity is discussed.

In the present calculations of the intensity of the rotational spectrum we assume that the intermolecular forces are independent of the orientations of the molecules. For such purely central forces there is no coupling between the rotational and translational motions of the molecules, and the total energy of the gas is equal to the sum of the rotational energy E_r and the translational energy E_t , $E = E_r + E_t$, where r and t are the quantum numbers specifying the rotational and translational motions of the molecules. According to the general theory of induced absorption (Van Kranendonk 1957), the spectrum is then built up additively out of the separate rotational lines which arise from definite rotational transitions accompanied by arbitrary changes in the translational motion of the molecules. The true rotational lines correspond to transitions in which the rotational quantum number J of at least one

¹Manuscript received June 29, 1959.

Contribution from the Physics Department, University of Toronto, Toronto, Ontario.

²Holder of a Canadian Kodak Fellowship, 1958-1959.

molecule changes such that the total rotational energy is different before and after the absorption ($E_{r'} \neq E_r$). Transitions in which only the translational energy changes and in which the total rotational energy remains unchanged can also take place in virtue of the strong dependence of the induced dipole moments on the intermolecular separations. These transitions give rise to the translational branch of the spectrum, which has been observed in mixtures of the rare gases (Kiss and Welsh 1959a), and for which evidence has also been obtained in the rotational spectra of hydrogen and hydrogen-foreign gas mixtures (Kiss *et al.* 1959). The translational absorption arises from pure translational transitions ($\Delta J_t = 0, \Delta m_t = 0$), and from transitions in which the translational jump is accompanied by an orientational transition ($\Delta m_t \neq 0$) in one or more molecules, or by two equal but oppositely directed rotational transitions ($\Delta J_t = -\Delta J_k, J'_t = J_k$). The absorption arising from all these transitions will be referred to as the translational absorption.

The integrated intensity, in the pure gas, of a definite rotational line is given by (Van Kranendonk 1957)

$$(1) \quad \bar{\alpha}(r, r') = (4\pi^2/3\hbar V) \sum_{t < t'} (P_r P_t - P_{r'} P_{t'}) |\langle r | \mathbf{u} | r' t' \rangle|^2.$$

V is the total volume of the gas; P_r and P_t are the normalized Boltzmann factors for the rotational and translational states respectively; $\mathbf{u} = \mathbf{u}(\omega^N, \mathbf{R}^N)$ is the total induced dipole moment which is a function of the orientations $\omega^N \equiv (\omega_1, \dots, \omega_N)$ and of the positions $\mathbf{R}^N \equiv (\mathbf{R}_1, \dots, \mathbf{R}_N)$ of the N molecules. The term $P_r P_t$ in (1) corresponds to absorption, and the term $P_{r'} P_{t'}$ to stimulated emission. The sum in (1) runs over all pairs of translational states t, t' for which $E_r + E_t < E_{r'} + E_{t'}$. If the rotational line $r \rightarrow r'$ does not extend to zero frequency, the sum over t and t' in (1) may be extended over *all* pairs of translational states, since the terms for which $E_r + E_t > E_{r'} + E_{t'}$ then give no appreciable contribution to this sum. In virtue of the completeness of the translational states, one then obtains the following expression for the integrated intensity (1) (Van Kranendonk 1957):

$$(2) \quad \bar{\alpha}(r, r') = (4\pi^2/3\hbar V) (P_r - P_{r'}) \int |\mathbf{M}_{rr'}(\mathbf{R}^N)|^2 f(\mathbf{R}^N) d\mathbf{R}^N.$$

The distribution function $f(\mathbf{R}^N)$ is defined as

$$(3) \quad f(\mathbf{R}^N) = \sum_t P_t |\psi_t(\mathbf{R}^N)|^2,$$

and $\mathbf{M}_{rr'} = \langle r | \mathbf{u} | r' \rangle$. According to the result (2), the integrated intensity $\bar{\alpha}(r, r')$ is equal to the intensity for a "frozen" configuration \mathbf{R}^N of the centers of mass of the molecules, averaged over all configurations \mathbf{R}^N with the help of the configurational distribution function (3).

For the integrated translational absorption no theorem analogous to (2) holds, as is directly evident from the fact that the intensity for a frozen configuration would be zero in this case. The restriction $t < t'$, now implying $E_t < E_{t'}$, is essential because the translational branch extends to zero fre-

quency. The calculation of the integrated translational intensity is therefore more complicated. We restrict ourselves in the present paper to the true rotational spectrum and we discuss the calculation of the translational intensity in a separate paper.

2. GENERAL EXPRESSIONS FOR THE BINARY ABSORPTION COEFFICIENTS OF THE ROTATIONAL LINES

The expression (2) for the absorption coefficient $\bar{\alpha}(r, r')$ can be developed in powers of the density $n = N/V$ of the gas in much the same way as was done previously for the vibrational spectrum (Van Kranendonk 1957). The only difference is that in the vibrational case the vibrating molecule plays a particular role, whereas in the rotational case all the molecules should be treated on a par. One must then introduce \mathbf{U} -functions by means of the equations

$$(4) \quad \begin{cases} \mathbf{M}(12) = \mathbf{U}(12); \\ \mathbf{M}(123) = \mathbf{U}(123) + \mathbf{U}(12) + \mathbf{U}(13) + \mathbf{U}(23); \\ \text{etc.} \end{cases}$$

Proceeding in this way, the expression for the binary absorption coefficient $\bar{\alpha}_1$ in the expansion

$$(5) \quad \bar{\alpha} = \bar{\alpha}_1 n^2 + \bar{\alpha}_2 n^3 + \dots$$

of the absorption coefficient in powers of the density is found to be given by

$$(6) \quad \bar{\alpha}_1(B) = \frac{1}{2} \kappa \sum^{(B)} (P_r - P_{r'}) \int |\mathbf{M}_{rr'}(\mathbf{R})|^2 g_0(\mathbf{R}) d\mathbf{R}.$$

$\kappa = 4\pi^2/3\hbar$; the sum in (6) extends over all transitions $r \equiv (J_1, m_1, J_2, m_2)$ to $r' \equiv (J'_1, m'_1, J'_2, m'_2)$, in the pair of molecules 1, 2 that contribute to the rotational line B , and $g_0(\mathbf{R})$ is the low-density limit of the pair distribution function $g(\mathbf{R})$. The quantity

$$(7) \quad \mathbf{M}_{rr'}(\mathbf{R}) = \langle r | \mathbf{y}(\omega_1, \omega_2; \mathbf{R}) | r' \rangle$$

is the matrix element of the pair dipole moment \mathbf{y} . This pair dipole moment is expanded in terms of spherical harmonics of the orientations of the molecules,

$$(8) \quad \mu_\kappa(\omega_1, \omega_2; R) = 4\pi \sum_{\lambda_1 \mu_1 \lambda_2 \mu_2} C_\kappa(\lambda_1 \mu_1 \lambda_2 \mu_2, R) Y_{\lambda_1}^{\mu_1}(\omega_1) Y_{\lambda_2}^{\mu_2}(\omega_2).$$

$\kappa = 0, \pm 1$ refers to 0, ± 1 components of \mathbf{y} in a co-ordinate system the z -axis of which lies along \mathbf{R} , and $\omega_i \equiv (\theta_i, \phi_i)$ specifies the orientation of molecule i relative to \mathbf{R} as polar axis. For homonuclear diatomic molecules $C_\kappa = 0$ for λ_1 or λ_2 odd. We further note the symmetry property

$$(9) \quad C_\kappa(\lambda_1 \mu_1 \lambda_2 \mu_2, R) = -C_\kappa(\lambda_2 \mu_2 \lambda_1 \mu_1, R),$$

which is a consequence of the invariance of the Hamiltonian of the two

interacting molecules under an inversion at a point midway between the molecules, and the relations

$$(10) \quad \begin{cases} C_{\kappa}(\lambda_1\mu_1\lambda_2\mu_2, R) = C_{-\kappa}(\lambda_1-\mu_1\lambda_2-\mu_2, R)^*, \\ (11) \quad \begin{cases} C_{\kappa}(\lambda_1\mu_1\lambda_2\mu_2, R) = 0 & \text{unless } \mu_1+\mu_2 = \kappa, \end{cases} \end{cases}$$

which follow from reality requirements and from the transformation properties for rotations around the z -axis respectively.

When the expansion (8) is substituted into (6), the resulting expression for the binary absorption coefficient can be written in the form

$$(12) \quad \bar{\alpha}_1(B) = \frac{1}{2}\kappa \sum_{\lambda_1\lambda_2} L_{\lambda_1\lambda_2}(B) I_0(\lambda_1\lambda_2),$$

$$(13) \quad L_{\lambda_1\lambda_2}(B) = \sum^{(B)} [P(J_1)P(J_2) - P(J'_1)P(J'_2)] L_{\lambda_1}(J_1, J'_1) L_{\lambda_2}(J_2, J'_2),$$

$$(14) \quad I_0(\lambda_1\lambda_2) = \int \sum_{\kappa\mu_1\mu_2} |C_{\kappa}(\lambda_1\mu_1\lambda_2\mu_2, R)|^2 g_0(\mathbf{R}) d\mathbf{R},$$

where the notation is the same as in the vibrational case (Van Kranendonk 1958). We take into account the terms in the expansion (8) corresponding to $(\lambda_1, \lambda_2) = (2, 0), (0, 2),$ and $(2, 2)$, and we neglect the terms corresponding to higher values of the λ 's. The angle-independent term $\lambda_1 = \lambda_2 = 0$ vanishes because of the symmetry property (9). For the *single rotational lines* corresponding to the transitions $J \leftrightarrow J+2$, the binary absorption coefficient (12) is then given by

$$(15) \quad \bar{\alpha}_1(J) = \kappa L(J) [I_0(20) + L' I_0(22)].$$

The factors $L(J)$ and L' , defined as

$$(16) \quad L(J) = L_2(J, J+2) [P(J) - P(J+2)],$$

$$(17) \quad L' = \sum_{J=0}^{\infty} L_2(J, J) P(J),$$

where

$$(18) \quad L_2(J, J) = \frac{J(J+1)(2J+1)}{(2J-1)(2J+3)}, \quad L_2(J, J+2) = \frac{3(J+1)(J+2)}{2(2J+3)},$$

determine the dependence of the absorption coefficients on the distribution of the molecules over the rotational states, whereas the quantities $I_0(20)$ and $I_0(22)$ determine the temperature dependence of the absorption coefficients due to that of the pair distribution function. For the *double rotational lines* corresponding to the double transitions $J, J' \leftrightarrow J+2, J'+2$ the binary absorption coefficient is

$$(19) \quad \bar{\alpha}_1(J, J') = \kappa [1 - \frac{1}{2}\delta(J, J')] L(J, J') I_0(22),$$

$$(20) \quad L(J, J') = L_2(J, J+2) L_2(J', J'+2) [P(J)P(J') - P(J+2)P(J'+2)].$$

Finally, the *total binary absorption coefficient* of the whole rotational band, but exclusive of the translational branch (cf. Section 1), is given by

$$(21) \quad \bar{\alpha}_1 = \kappa [L \cdot I_0(20) + M \cdot I_0(22)],$$

$$(22) \quad L = \sum_{J=0}^{\infty} L(J), \quad M = L \cdot L' + \sum_{J \neq J'=0}^{\infty} L(J, J').$$

The calculation of the binary absorption coefficients is thus reduced to the calculation of the quantities $I_0(20)$ and $I_0(22)$, defined by eq. (14), i.e. to the calculation of the coefficients C_κ in the expansion (8) of the induced dipole moment. As in the case of the vibrational spectrum (Van Kranendonk 1958), we assume that the induced dipole moment consists of a short range overlap moment arising from the overlap forces between the molecules, and a long range moment due to the quadrupolar induction effect. The calculation of these two parts of the induced moment is presented in the next section.

3. CALCULATION OF THE INDUCED ROTATIONAL DIPOLE MOMENT

The main contribution to the induced rotational dipole moment comes from the quadrupolar induction effect (Van Kranendonk 1958). The intensity of the rotational spectrum resulting from this induction effect has been calculated by Colpa *et al.* (1958*b*) and by Kiss *et al.* (1959). In our notation, the non-vanishing coefficients in the expansion (8) for this part of the induced moment are given by

$$(23) \quad \left\{ \begin{array}{ll} C_0(2000) = \frac{3}{\sqrt{5}} \frac{\alpha Q}{R^4}; & C_1(2100) = -\frac{3}{\sqrt{15}} \frac{\alpha Q}{R^4}; \end{array} \right.$$

$$(24) \quad \left\{ \begin{array}{ll} C_1(2120) = -\frac{4\sqrt{3}}{15} \frac{\gamma Q}{R^4}; & C_1(222-1) = -\frac{\sqrt{2}}{5} \frac{\gamma Q}{R^4}; \end{array} \right.$$

plus 10 other coefficients which follow from (23), (24) by means of the symmetry relations (9) and (10). Q is the quadrupole moment, $\alpha = \frac{1}{3}(2\alpha_{\perp} + \alpha_{\parallel})$ is the average polarizability, and $\gamma = \alpha_{\parallel} - \alpha_{\perp}$ is the anisotropy of the polarizability of a hydrogen molecule in the normal state. The phases of the spherical harmonics in (8) have been chosen to be $+1$ rather than $i^{|m|+m}$. The spherical components μ_κ are accordingly defined as $\mu_0 = \mu_z$, $\mu_{\pm 1} = (\mu_x \pm i\mu_y)/\sqrt{2}$.

The rotational overlap dipole moment for a pair of hydrogen molecules is given by

$$(25) \quad \left\{ \begin{array}{l} \Psi_{ov} = -\mathbf{N}/D, \end{array} \right.$$

$$(26) \quad \left\{ \begin{array}{l} \mathbf{N} = -\int \Psi_e^*(\Sigma_i e_i \mathbf{r}_i) \Psi_e d1d2d3d4, \end{array} \right.$$

$$(27) \quad \left\{ \begin{array}{l} D = \int \Psi_e^* \Psi_e d1d2d3d4. \end{array} \right.$$

Ψ_e (1234) is the electron wave function as a function of the position and spin co-ordinates of the four electrons, depending parametrically on the nuclear co-ordinates. The sum over i in (24) runs over the four protons ($e_a = e_b = e_c = e_d = e$) and over the four electrons ($e_1 = e_2 = e_3 = e_4 = -e$),

and \mathbf{r}_i is the position vector of the i th particle. For ψ_e we use the same type of wave function as was used for the vibrational case, viz.

$$(28) \quad \psi_e = (1 - P_{13} - P_{14} - P_{23} - P_{24} + P_{13}P_{24})\psi_{ab}(12)\psi_{cd}(34)\chi(12)\chi(34),$$

where P_{ij} is the operator exchanging the electrons i and j , $\chi(12)$ is the singlet spin function, and

$$(29) \quad \psi_{ab}(12) = a(1)b(2) + b(1)a(2).$$

The one-electron orbitals are distorted Rosen-type wave functions (Van Kranendonk and Bird 1951),

$$(30) \quad \begin{cases} a(1) = (Z/\pi)^{1/2} e^{-Zr_{a1}}(1 + \mathbf{l}_a \cdot \mathbf{r}_{a1}); \\ (31) \quad \mathbf{l}_a = \kappa_{ab} + \lambda_{ac} + \lambda_{ad}. \end{cases}$$

Z is the effective nuclear charge; $\mathbf{r}_{a1} = \mathbf{r}_1 - \mathbf{r}_a$; $\kappa_{ab} = \kappa_{ab}\mathbf{r}_{ab}/r_{ab}$, $\lambda_{ac} = \lambda_{ac}\mathbf{r}_{ac}/r_{ac}$, etc. The term containing κ describes the distortion of orbital a due to atom b ; the terms containing λ_{ac} and λ_{ad} describe the distortions induced in a by the atoms c and d respectively. The orbitals b , c , and d are defined similarly, with

$$(32) \quad \begin{cases} \mathbf{l}_b = -\kappa_{ab} + \lambda_{bc} + \lambda_{bd}; & \mathbf{l}_c = \kappa_{cd} - \lambda_{ac} - \lambda_{bc}; \\ \mathbf{l}_d = -\kappa_{cd} - \lambda_{ad} - \lambda_{bd}. \end{cases}$$

The dipole moment (25) vanishes if the overlap between the two molecules and the distortions described by the terms containing λ 's are neglected. We calculate the moment (25) to the first non-vanishing order in the square of the overlap and the λ 's, treating the squares of the overlap integrals and the parameters λ as small quantities of the first order. The resulting expression for ψ_{ov} is equal to the sum of the following two terms:

$$(33) \quad \psi_{\text{def}} = -\frac{2S}{1+S^2} (\psi'_{ab} + \psi'_{cd});$$

$$(34) \quad \psi_{\text{exch}} = \frac{1}{2(1+S^2)^2} [\Sigma \psi_{aa}(S_{bc}^2 + S_{bd}^2 + 2S_{bc}S_{bd}) + 2 \Sigma \psi_{ac}(S_{ac} + S_{ad} + S_{bc} + S_{bd})].$$

The summation signs indicate that three additional terms should be written corresponding to cyclic permutations of a , b , c , and d . The quantities

$$(35) \quad \begin{cases} \psi_{aa} = e \int a(1)(\mathbf{r}_1 - \mathbf{r}_a)a(1)d1, \\ \psi_{ab} = e \int a(1)[\mathbf{r}_1 - \frac{1}{2}(\mathbf{r}_a + \mathbf{r}_b)]b(1)d1, \\ S = \int a(1)b(1)d1, \\ S_{ac} = \int a(1)c(1)d1 \end{cases}$$

appearing in (33) and (34) are to be evaluated by putting all λ 's equal to zero, whereas the quantities ψ'_{ab} and ψ'_{cd} in (33) contain only the terms in

\mathbf{u}_{ab} and \mathbf{u}_{cd} respectively that are linear in the λ 's. The moment (33) is therefore proportional to the λ 's and is called the deformation moment, whereas the moment (34) is proportional to the square of the overlap integral between the two molecules, and is called the exchange moment. The quantities (35) can be easily evaluated, giving

$$(36) \quad \begin{cases} \mathbf{u}_{aa} = 2eZ^{-2}\mathbf{l}_a; & \mathbf{u}_{ab} = e\mathbf{A}_{ab} \cdot \mathbf{l}_{ab}; \\ \mathbf{A}_{ab} = (Z^3/\pi) \int e^{-Z(ra_1+rb_1)} \mathbf{r}_1 \mathbf{r}_1 d\mathbf{r}_1; \\ \mathbf{l}_{ab} = (1 + \frac{1}{2}\mathbf{l}_a \cdot \mathbf{r}_{ab})\mathbf{l}_b + (1 - \frac{1}{2}\mathbf{l}_b \cdot \mathbf{r}_{ab})\mathbf{l}_a; \end{cases}$$

and similarly for \mathbf{u}_{bb} , \mathbf{u}_{ac} , etc. The moments (33) and (34) have been evaluated for the two orientations $\theta_1 = 0$, $\theta_2 = \pi$ and $\theta_1 = 0$, and $\theta_2 = \frac{1}{2}\pi$ of the two molecules, and for a number of intermolecular separations R . The resulting moments turn out to decrease very nearly exponentially with increasing R , and to lead to the following values of the expansion coefficients in (8):

$$(37) \quad \begin{cases} C_\kappa(2K00) = -C_\kappa(002K) = \xi_\kappa e^{-R/\rho}; \end{cases}$$

$$(38) \quad \begin{cases} \xi_0 = -0.16e\sigma; & \xi_{\pm 1} = -0.03e\sigma; & \rho = 0.126\sigma; \end{cases}$$

where $\sigma = 2.93 \text{ \AA}$ is the molecular diameter appearing in the Lennard-Jones potential. The coefficients (37) should be added to the corresponding coefficients (23) arising from the quadrupolar induction effect to get the total expansion coefficients. This completes the evaluation of the induced rotational dipole moment.

4. CALCULATION OF THE BINARY ABSORPTION COEFFICIENTS OF THE ROTATIONAL LINES

When we substitute the expressions (23), (24), and (37) for the expansion coefficients into the expression (14) for the integrals I_0 , we obtain the following expressions for the binary absorption coefficients:

For the single rotational lines, cf. eq. (15),

$$(39) \quad \bar{\alpha}_1(J) = L(J) \left[(\lambda_0^2 + 2\lambda_1^2)I + \mu^2 J + \mu(\lambda_0 - \frac{2}{\sqrt{3}}\lambda_1)K \right] \tilde{\gamma} + L(J)L'\mu'^2 J \tilde{\gamma}.$$

For the double rotational lines, cf. eq. (19),

$$(40) \quad \bar{\alpha}_1(J, J') = [1 - \frac{1}{2}\delta(J, J')] L(J, J') \mu'^2 J \tilde{\gamma}.$$

For the total binary absorption coefficient, cf. eq. (21),

$$(41) \quad \bar{\alpha}_1 = L \left[(\lambda_0^2 + 2\lambda_1^2)I + \mu^2 J + \mu \left(\lambda_0 - \frac{2}{\sqrt{3}}\lambda_1 \right) K \right] \tilde{\gamma} + M \mu'^2 J \tilde{\gamma}.$$

The dimensionless quantities λ_0 , λ_1 , μ , and μ' are defined as (cf. Van Kranendonk 1958)

$$(42) \quad \lambda_\kappa = (\xi_\kappa/e\sigma) e^{-\sigma/\rho}; \quad \mu = \frac{\alpha Q}{e\sigma}; \quad \mu' = \left(\frac{88}{225} \right)^{\frac{1}{2}} \frac{\gamma Q}{e\sigma};$$

and the quantity

$$(43) \quad \bar{\gamma} = (4\pi^2 e^2 \sigma^5 / 3\hbar),$$

has the dimension of a binary absorption coefficient. The integrals I , J , and K are defined as

$$(44) \quad \begin{cases} I = 4\pi \int_0^\infty e^{-2(x-1)\sigma/\rho} g_0(x) x^2 dx, \\ J = 12\pi \int_0^\infty x^{-8} g_0(x) x^2 dx, \\ K = \frac{24\pi}{\sqrt{5}} \int_0^\infty x^{-4} e^{-(x-1)\sigma/\rho} g_0(x) x^2 dx, \end{cases}$$

where $x = R/\sigma$. At high temperatures classical statistics may be used, and the pair distribution function is then equal to the Boltzmann factor $\exp[-V(x)/kT]$, where $V(x)$ is the intermolecular potential for which we choose the Lennard-Jones potential

$$(45) \quad V(x) = 4\epsilon(x^{-12} - x^{-6}).$$

At intermediate temperatures, $g_0(x)$ may be expanded in powers of Planck's constant. The resulting expansions of the integrals (44) are written in the form

$$(46) \quad I = I_{cl} - \Lambda^{*2} I^{(2)} + \Lambda^{*4} I^{(4)} + \dots,$$

and similarly for J and K , where $\Lambda^* = (\hbar^2/m\epsilon\sigma^2)^{1/2}$. The integrals I_{cl} , $I^{(2)}$, and $I^{(4)}$, etc. have been evaluated numerically for a number of reduced temperatures $T^* = kT/\epsilon$. The results are collected in Table I. We note here that in Table I of a previous publication (Van Kranendonk 1958) the headings

TABLE I

Classical values and first and second quantum corrections of the radial integrals I , K , and J
 $\rho = 0.126 \sigma$

T^*	I_{cl}	K_{cl}	J_{cl}	$I^{(2)}$	$K^{(2)}$	$J^{(2)}$	$I^{(4)}$	$K^{(4)}$	$J^{(4)}$
1.0	2.26	8.32	16.15	1.85×10^{-1}	1.41	2.75	4.72×10^{-2}	4.93×10^{-1}	8.90×10^{-1}
1.5	2.09	7.19	13.40	5.42×10^{-2}	0.614	1.20	8.36×10^{-3}	1.36	2.39
2.0	2.14	6.98	12.50	1.84	0.372	0.732	2.20×10^{-2}	6.08×10^{-2}	1.05
2.5	2.25	7.03	12.16	0.38	0.263	0.518	5.78×10^{-4}	3.44	5.79×10^{-2}
3.0	2.39	7.20	12.05	-0.35	0.203	0.400	0.37	2.23	3.67
3.5	2.54	7.42	12.06	-0.76	0.165	0.325	-1.61	1.57	2.54
4.0	2.70	7.67	12.13	-1.00	0.140	0.274	-2.31	1.18	1.87
5.0	3.02	8.19	12.37	-1.25	0.108	0.210	-2.45	7.47×10^{-2}	1.14
6.0	3.34	8.72	12.66	-1.36	0.089	0.172	-2.14	5.26	7.78×10^{-2}
7.0	3.66	9.25	12.97	-1.40	0.076	0.146	-1.78	3.96	5.68
8.0	3.98	9.76	12.29	-1.40	0.068	0.127	-1.46	3.12	4.37
9.0	4.29	10.27	13.60	-1.39	0.061	0.114	-1.19	2.55	3.48
10.0	4.60	10.76	13.91	-1.37	0.056	0.103	-0.97	2.14	2.85

of the 4th and the 5th columns of this table should be $10^3 \cdot I^{(2)}/4\pi$ and $10^3 \cdot J^{(2)}/12\pi$ respectively. In the calculations the correct values of $I^{(2)}$ and $J^{(2)}$ were used.

We first discuss the total binary absorption coefficient at $T = 300^\circ \text{K}$. Using the theoretical value of James and Coolidge (1942) for the quadrupole moment, $Q = 0.45ea_0^2$, and the experimental values $\alpha = 5.7a_0^3$ and $\gamma = 1.6a_0^3$ (Volkman 1935), the numerical values of the various terms in the expression (41) for the total binary absorption coefficient are given by

$$(47) \quad \tilde{\alpha}_1 = (0.01 + 1.04 - 0.08 + 0.02)\tilde{a} = 0.99\tilde{a},$$

where $\tilde{a} = 10^{-34} \text{sec}^{-1} \text{cm}^6$. The first term is the intensity due to the overlap moment alone, and is quite small. The second and fourth terms are due to the quadrupolar induction effect, and give the main contribution to the total intensity. The third term represents the interference effect between the quadrupolar and overlap moments. The experimental value of $\tilde{\alpha}_1$, given by Kiss *et al.* (1959) is the total intensity inclusive of the translational absorption, whereas (47) is the calculated intensity exclusive of the translational absorption (cf. Section 1). The experimental value must therefore be corrected for this effect. This has been done by analyzing the shape of the rotational absorption lines (Kiss and Welsh 1959b), and the resulting experimental value of $\tilde{\alpha}_1$ is $1.19\tilde{a}$. The theoretical value (47) is in good agreement with this value as far as the order of magnitude is concerned, but is about 20% too small. The quadrupolar induction effect gives a contribution of $1.06\tilde{a}$ and thus accounts for 90% of the observed intensity. This value depends on the quantities Q , α , γ , σ , and ϵ , all of which are known rather accurately for hydrogen. The calculated value of the quadrupolar intensity should therefore be rather accurate. The inclusion of the overlap induction effect reduces the intensity by $0.07\tilde{a}$, giving a final value about 20% smaller than the experimental one. It is possible that this discrepancy is due to an inaccuracy in the calculated quadrupolar intensity, or to the fact that we use a simple model for the total induced dipole moment, in which only the terms of longest (R^{-4}) and shortest ($\exp -R/\rho$) range are taken into account. Thus in addition to the R^{-4} terms, there will be terms varying as R^{-6} , etc. It is, however, more likely that the calculation of the overlap moment discussed in Section 3, which is based on the use of Rosen-type wave functions, is not reliable. Support for this conclusion is obtained from an analysis of the vibrational-rotational spectrum of hydrogen. The most important part of the vibrational overlap moment is independent of the orientations of the molecules (Van Kranendonk 1958). The order of magnitude of this part of the overlap moment is given correctly by the calculation based on Rosen-type wave functions. However, the angle-dependent part of the vibrational overlap moment is an order of magnitude smaller than the isotropic part, and is not given correctly by the calculations. A detailed analysis of the intensities in the vibrational spectrum, carried out by Hunt (1959), has shown that the phenomenological value of the angle-dependent part of the overlap moment, obtained by fitting the calculated absorption coefficients to the experimental ones, is of the same order of magnitude as the calculated value but of opposite sign. In the case of the rotational overlap moment, the isotropic part of the moment vanishes identically as a result of the symmetry relation (9), and only a small angle-dependent part survives. When we neglect the first term in the expression (41) for the

total binary absorption coefficient, the contribution of the overlap moment to the total intensity can be described by means of the single parameter $\lambda = \lambda_0 - (2/\sqrt{3})\lambda_1$. The expression (41) then becomes

$$(48) \quad \tilde{\alpha}_1 = L(\mu^2 J + \lambda \mu K) \tilde{\gamma} + M \mu'^2 J \tilde{\gamma}.$$

All the quantities appearing in this expression are known, except λ . An empirical value of λ can be obtained by adjusting the value of (48) to the experimental value of λ . This has been done for $T = 300^\circ \text{K}$, giving $\lambda_{\text{exp}} = 0.8 \times 10^{-4}$, whereas the calculated value of λ (cf. Section 3) is $\lambda_{\text{theor}} = -0.5 \times 10^{-4}$. As in the case of the vibrational overlap moment, we reach the conclusion that the calculations based on Rosen-type wave functions are not elaborate enough to yield a reliable value for the angle-dependent part of the overlap moment. We therefore adopt for λ the empirical value 0.8×10^{-4} , and calculate the temperature dependence of $\tilde{\alpha}_1$, and the intensities of the separate rotational lines, using this value for λ . A theoretical determination of λ , based on the use of more realistic wave functions for two interacting hydrogen molecules, will not be attempted in the present paper.

The temperature dependence of $\tilde{\alpha}_1$ has been calculated using the expression (48) with $\lambda = 0.8 \times 10^{-4}$. The quantities L and M appearing in (48) have been calculated numerically as functions of the temperature for equilibrium and normal hydrogen, and the results are collected in Table II, where L and

TABLE II
Statistical factors L and M for hydrogen

T^*	Equilibrium H_2		Normal H_2	
	L	M	L	M
0.5	1.000	0.500	0.700	0.455
1.0	0.967	0.500	0.700	0.455
1.5	0.882	0.493	0.700	0.455
2.0	0.810	0.481	0.698	0.455
2.5	0.762	0.470	0.697	0.453
3.0	0.729	0.460	0.692	0.450
3.5	0.705	0.452	0.684	0.446
4.0	0.686	0.444	0.675	0.441
5.0	0.656	0.429	0.652	0.429
6.0	0.630	0.415	0.629	0.415
7.0	0.606	0.400	0.606	0.400
8.0	0.584	0.386	0.584	0.386
9.0	0.564	0.373	0.564	0.373
10.0	0.545	0.360	0.545	0.360

M are given as functions of $T^* = kT/\epsilon$, in which $\epsilon/k = 37.0^\circ \text{K}$ for pure hydrogen as well as for mixtures of hydrogen with foreign gases. The resulting temperature variation of $\tilde{\alpha}_1$ is shown in Fig. 1 for the equilibrium ortho-para ratio at each temperature. The agreement with the experimental temperature variation of $\tilde{\alpha}_1$ is seen to be very good. There is a marked difference between the temperature dependence of the total intensity of the vibrational band and that of the pure rotational band. For the vibrational band the intensity is independent of the distribution of the molecules over the rotational states

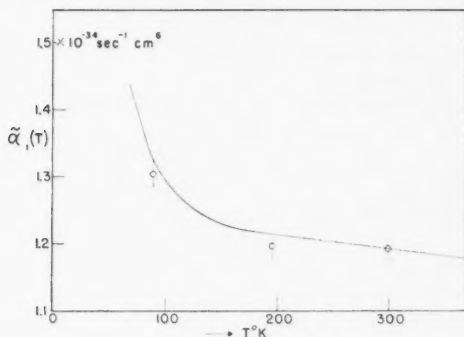


FIG. 1. The temperature variation of the binary absorption coefficient of equilibrium hydrogen.

(Van Kranendonk 1958), and the temperature dependence is due entirely to the temperature dependence of the pair distribution function. For the pure rotational band this is not so; an important part of the temperature variation of $\tilde{\alpha}_1$ is due to the factors L and M appearing in (48). These factors depend on the distribution of the molecules over the rotational states, and therefore on the temperature.

The variation of the total intensity (48) with varying ortho-para ratio at a given temperature is due entirely to the dependence of the factors L and M on this ratio. Neglecting the small term proportional to M , the ratio of the intensities for normal and equilibrium hydrogen is given by

$$(49) \quad \tilde{\alpha}_1(\text{norm.})/\tilde{\alpha}_1(\text{eq.}) = L(\text{norm.})/L(\text{eq.}),$$

where L is given by eq. (22). According to (49), the intensity at liquid air temperature should be 8% less for normal than for equilibrium hydrogen. Experimentally (Kiss 1959) the value of $\tilde{\alpha}_1$ for normal hydrogen at $T = 85^\circ \text{K}$ is about 7% less, in satisfactory agreement with the theoretical value.

The intensities of the separate rotational lines can be calculated using the expression (39). The calculated intensity ratios can be used to analyze the observed absorption contours; this will be discussed in detail in a separate paper. At liquid air temperature the $S(0)$ and $S(1)$ lines are well resolved, and the observed ratio of the intensities for equilibrium hydrogen is then equal to $S(0)/S(1) = 1.06$, whereas the theoretical value of this ratio is 1.14. The double rotational transition $S(1)+S(1)$ has also been observed, and the intensity of this line is estimated to be about $3.2 \times 10^{-37} \text{ sec}^{-1} \text{ cm}^6$. The value calculated from (41) with $\gamma = 1.6a_0^3$ is equal to $4.5 \times 10^{-37} \text{ sec}^{-1} \text{ cm}^6$. A more accurate measurement of the intensity is necessary to decide whether the difference between the calculated and observed value is significant.

Finally, we discuss the rotational spectrum of hydrogen induced by foreign gases (Kiss *et al.* 1959). The total binary absorption coefficient for a mixture of hydrogen with a foreign gas b is given by

$$(50) \quad \bar{\alpha}_{1b} = \frac{1}{2}L(\mu^2J + \lambda\mu K)\bar{\gamma}.$$

If we assume that the constants characterizing the intermolecular potential for two different molecules are given by $\sigma = \frac{1}{2}(\sigma_1 + \sigma_2)$ and $\epsilon = (\epsilon_1\epsilon_2)^{\frac{1}{2}}$, all the quantities appearing in (50) are known for the mixtures of interest, except λ . Values of λ for the various mixtures can be determined by fitting the value of (50) to the observed values of $\bar{\alpha}_{1b}$. This leads to the following values: $\lambda(\text{H}_2\text{-He}) = 0.5 \times 10^{-4}$; $\lambda(\text{H}_2\text{-H}_2) = 0.8 \times 10^{-4}$; $\lambda(\text{H}_2\text{-Ne}) = 3 \times 10^{-4}$; $\lambda(\text{H}_2\text{-N}_2) = 2 \times 10^{-4}$; $\lambda(\text{H}_2\text{-A}) = 6 \times 10^{-4}$. Thus in all these cases a small positive value of λ is required. In each case the quadrupolar induction effect accounts for at least 90% of the total intensity, and the values of λ given here should therefore be regarded only as order of magnitude estimates. This is true in particular for the mixtures, for which the constants ϵ and σ are not well known.

In conclusion we can say that the theory of the induced infrared absorption based on the (exp -4) model for the induced dipole moment accounts satisfactorily for the observed properties of the pressure-induced pure rotational spectrum of hydrogen in the pure gas and in mixtures.

ACKNOWLEDGMENTS

The authors wish to express their gratitude to Dr. W. H. Watson for placing the facilities of the Computation Centre of the University of Toronto at their disposal. The authors also wish to thank Dr. J. L. Hunt for his assistance with the numerical calculations.

REFERENCES

- COLPA, J. P. and KETELAAR, J. A. A. 1958a. *Mol. Phys.* **1**, 14.
 ——— 1958b. *Mol. Phys.* **1**, 343.
 HUNT, J. L. 1959. Ph.D. Thesis, University of Toronto, Toronto, Ontario.
 JAMES, H. M. and COOLIDGE, A. S. 1942. *Astrophys. J.* **87**, 438.
 KISS, Z. J., GUSH, H. P., and WELSH, H. L. 1959. *Can. J. Phys.* **37**, 362.
 KISS, Z. J. and WELSH, H. L. 1959a. *Phys. Rev. Letters*, **2**, 4.
 ——— 1959b. *Can. J. Phys.* (submitted).
 VAN KRANENDONK, J. and BIRD, R. B. 1951. *Physica*, **17**, 953.
 VAN KRANENDONK, J. 1957. *Physica*, **23**, 825.
 ——— 1958. *Physica*, **24**, 347.
 VOLKMANN, H. 1935. *Ann. Physik*, **24**, 451.

NOTES

A NOTE ON *s*-WAVE AVERAGE NEUTRON CROSS SECTIONS*

KAMAL K. SETH

It was shown by Thomas (1955a) that the average cross-section problem (Feshbach *et al.* 1955) corresponds to the averaging of the collision matrix over a region containing many resonances, and hence consists of replacing the logarithmic derivative f by its average $\langle f \rangle = \langle R \rangle^{-1} + B$. The average R function is given by

$$\langle R \rangle = R^\infty + i\pi s$$

where $s = \langle \gamma^2 \rangle / \langle D \rangle$ is related to (and sometimes confusingly called) the strength function, and $R^\infty = \int [s / (E' - E)] dE'$ (the integral extends over the energy interval of averaging). For the *s*-wave neutrons one conventionally puts the boundary parameter $B = 0$, and obtains (Lane and Lynn 1957) (putting $\rho = kR$ and omitting the summation over spin states for the sake of simplicity)

$$(1) \quad \langle \sigma_t \rangle_{l=0} = 4\pi\lambda^2 \frac{(\sin \rho - \rho R^\infty \cos \rho)^2 + \pi \rho s (1 + \pi \rho s \cos^2 \rho)}{(1 + \pi \rho s)^2 + (\rho R^\infty)^2},$$

which is naturally the same expression which is obtained for the total cross section for an optical, square-edge, spherically symmetric potential well (eq. 3.10 in Feshbach *et al.* 1955) if the following identity is established.

$$\alpha_1 \equiv R^\infty \text{ and } \alpha_2 \equiv \pi s.$$

Here α_1 and α_2 are the real and the imaginary parts respectively of the reciprocal of the logarithmic derivative for the potential at the surface.

It is impractical to use eq. 1 in the analysis of the experimental data for the purpose of determining R^∞ and s . For small values of kR Feshbach, Porter, and Weisskopf (1955) approximated eq. 1 by

$$(2) \quad \langle \sigma_t(E) \rangle_{l=0} = 4\pi(R')^2 + 2\pi^2\lambda^2 \sqrt{E} \langle \Gamma_n^0 \rangle / \langle D \rangle$$

where $R' = \lambda(\rho - \tan^{-1} \rho R^\infty) \cong R(1 - R^\infty)$, and $\sqrt{E} \Gamma_n^0 = 2\rho\gamma^2$. It was shown by Lane and Lynn (1957) that this expression neglects the resonance-resonance interference term which is of the same order in ρ as the first term, i.e., of the order ρ^2 . Lane and Lynn (1957) obtained

$$(3) \quad \langle \sigma_t(E) \rangle_{l=0} = \{4\pi(R')^2 - \pi^2\lambda^2 E \langle \langle \Gamma_n^0 \rangle / \langle D \rangle \rangle^2\} + 2\pi^2\lambda^2 \sqrt{E} \langle \Gamma_n^0 \rangle / \langle D \rangle$$

by expanding both the numerator and the denominator of the right-hand side of eq. 1 and retaining terms of orders up to ρ^2 . This expression was used in a preliminary analysis by the author (Seth 1958a) to resolve the discrepancy

*Supported by the United States Atomic Energy Commission.

between the thin and thick sample results for strength function $\langle \Gamma_n^0 \rangle / \langle D \rangle$ obtained by Marshak and Newson (1957) from the analysis of the average total cross-section experiments for nuclei with atomic weights between 35 and 75. The energy-independent term in the braces in eq. 3 (identified with $4\pi(R)^2$ by Marshak and Newson (1957)) was shown to be negative for $A = 50$, and found to be important whenever the strength function has a large value (Seth 1958*b*). A more exhaustive study has revealed that while eq. 3 is quite accurate (within 5% of eq. 1) for energies $E < 5$ kev, it may be in gross error for higher energies. It is found that inclusion of terms of order ρ^3 makes the expression unwieldy without improving its accuracy appreciably. In order to be able to analyze total cross-section data in the region of $\text{Li}(p, n)$ neutron energies simply and with accuracy we find the following approximation useful:

$$\begin{aligned} \langle \sigma_t(E) \rangle_{t=0} = & 4\pi\lambda^2 \{ \sin^2(\rho + \beta) + \left(\frac{\pi\rho s}{d^2} \right) (1 - 2\pi\rho s/d^2) \cos 2(\rho + \beta) \\ & + (\pi s/d)^2 [\cos^2 \rho - \sin^2(\rho + \beta)] \}. \end{aligned}$$

Here $\beta \equiv -\tan^{-1} \rho R^{\infty} \cong \rho R^{\infty} \doteq k(R' - R)$ and $d \equiv [1 + (\rho R^{\infty})^2]^{1/2} \cong 1$, since R^{∞} is small. This permits further simplification

$$(4) \quad \langle \sigma_t(E) \rangle_{t=0} = 4\pi\lambda^2 \sin^2 kR' - \pi^3\lambda^2 E (\langle \Gamma_n^0 \rangle / \langle D \rangle)^2 \cos 2kR' + 2\pi^2\lambda^2 \sqrt{E} (\langle \Gamma_n^0 \rangle / \langle D \rangle) \cos 2kR'.$$

This expression is found to be much more accurate than eq. 3 without being any more complicated. In Fig. 1 we have plotted the errors in eqs. 3 and 4 expressed as a percentage of the exact cross section in eq. 1. The values of $\langle \Gamma_n^0 \rangle / \langle D \rangle$ and (R'/R) used are those obtained by Feshbach, Porter, and Weisskopf (1956) for the Saxon-type optical potential, $V = V_0(1 + i\xi)/\{1 + \exp[(r-R)/d]\}$ with $V_0 = 42$ Mev, $\xi = 0.08$, $R = 1.35A^{1/3}$ fermis, and $d = 0.45$ fermi. At 50 kev Lane and Lynn's (1957) approximation is seen (Fig. 1(a)) to be in error by $\sim 10\%$ for all values of A , reaching maximum values of 20 to 25% at $A \cong 60$ and 170. The situation rapidly deteriorates with increasing energy. At 500 kev the error is $\sim 100\%$ almost everywhere, becoming as high as 250% at $A \cong 170$. In contrast, our approximation, eq. 4, is seen (Fig. 1(b)) to have less than 1% error for all values of energy in the regions $70 \leq A \leq 120$ and $A \geq 180$. The error at other places usually increases with energy and oscillates between positive and negative values which are never greater than $\pm 25\%$, usually within 10%. At low energies, $E < 10$ kev, of course eq. 4 is equivalent to eq. 3 and has the same low errors, $< 1\%$. Further, it may be noted that not only is the magnitude of errors in our approximation smaller but the energy dependence of the errors is weaker than in Lane and Lynn's (1957). Thus Lane and Lynn's errors increase by a factor ~ 35 (from 2 to 5% to 70 to 170%) over an energy interval from 10 kev to 500 kev, while, over the same energy interval, our errors show almost no increase for most atomic weights; in the worst case they increase by a factor ~ 10 (from $\sim 2\%$ to $\sim 20\%$).

It may be mentioned here that the form of eq. 4 was suggested by the fact that simple averaging of the single-level Breit-Wigner formula as derived

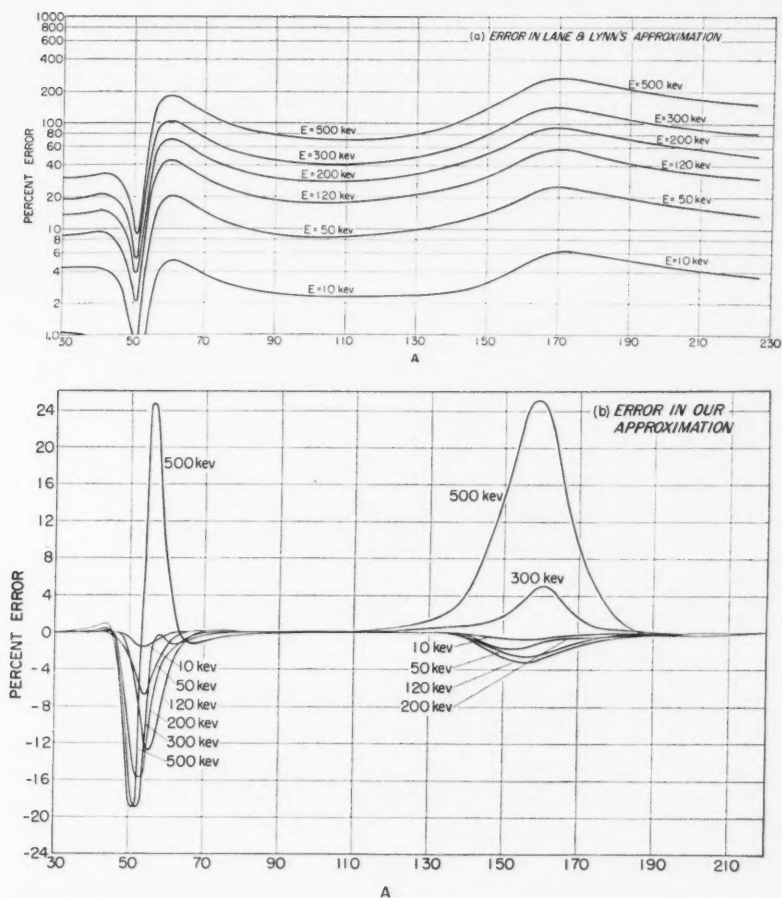


FIG. 1. Percentage error in the different approximations to eq. 1 for exact s-wave average cross section. (a) Lane and Lynn's (1957) approximation, eq. 3; note the logarithmic scale for the ordinate. (b) Our approximation; errors less than $\pm 0.1\%$ have not been drawn.

from the R -matrix theory (with the inclusion of the "background matrix", R^∞ , whose effect is to replace R by R' everywhere in the conventional single-level expression) yields exactly the first and the third terms of the eq. 4. The second term, as mentioned earlier, represents the average contribution of the resonance-resonance interference and can not be obtained by a single-level approximation. However, its proportionality to $(\langle \Gamma_n^0 \rangle / \langle D \rangle)^2$ can be easily established by evaluating the average contribution of the corresponding term in the scattering cross section obtained by simply adding two single-level scattering amplitudes, or by suitable averaging of a more sophisticated two-level formula (Lane and Thomas 1958).

It must be pointed out that the use of any of the above expressions in interpreting data is only valid if the experiment measures true cross section. It is usual, however, to measure σ_t by a transmission experiment. In such a case the above expressions can only be used for analyzing cross sections obtained by very thin samples ($n\langle\sigma_t\rangle \ll 1$, where n is the sample thickness). For thicker samples, methods based on single-level area considerations have been used (Marshak and Newson 1957; Seth 1958*a*, *b*). Thomas (1955*b*) has also developed a suitable expression for interpretation of average transmissions in terms of the average collision function, and the method, though cumbersome, has been used successfully (Darden 1955; Boreli and Darden 1958).

- BORELI, F. and DARDEN, S. E. 1958. *Phys. Rev.* **109**, 2079.
 DARDEN, S. E. 1955. *Phys. Rev.* **99**, 748.
 FESHBACH, H., PORTER, C. E., and WEISSKOPF, V. F. 1955. *Phys. Rev.* **96**, 448.
 ——— 1956. Unpublished (as reported by WEISSKOPF, V. F. 1956. *Physica*, **18**, 952).
 LANE, A. M. and LYNN, J. E. 1957. Atomic Energy Research Establishment, report T/R 2210.
 LANE, A. M. and THOMAS, R. G. 1958. *Revs. Modern Phys.* **30**, 257.
 MARSHAK, H. and NEWSON, H. W. 1957. *Phys. Rev.* **106**, 110.
 SETH, K. K. 1958*a*. *Revs. Modern Phys.* **30**, 442.
 ——— 1958*b*. *Bull. Am. Phys. Soc.* **3**, 224.
 THOMAS, R. G. 1955*a*. *Phys. Rev.* **97**, 224.
 ——— 1955*b*. *Phys. Rev.* **98**, 77.

RECEIVED JULY 2, 1959.
 DEPARTMENT OF PHYSICS,
 DUKE UNIVERSITY,
 DURHAM, NORTH CAROLINA.

NOTES ON A PHOTOGRAPH OF THE STARK EFFECT

J. S. FOSTER

The accompanying photograph may serve temporarily as a suitable illustration of the Stark effect and indeed is being so used by Professor Jenkins in a reference work where the text is necessarily limited. The photograph is somewhat enlarged from a plate taken with a Lo Surdo d-c. source in which the electric fields accompanying the cathode fall of potential are distributed over an axial distance of only 2 millimeters. Owing to heavy-particle excitation, relatively strong light is emitted from the core of the otherwise dark space.

The phenomenon so revealed entered physics through the quantum theory of spectra and the rather intricate web of experimental facts is interpreted in quantum mechanics.

The present illustration shows polarized components of the parhelium group $2^1P-6^1(S,D,F,G,H,P)$ roughly centered round the diffuse series line $\lambda 4144$. Analyses for individual lines are essentially asymmetric ($\pm m$ states degenerate) while the group builds up an over-all symmetry as the external electric field increases (mutual repulsion between states with same $|m|$ value.) Incidentally, molecular lines in the background show little or no displacements.

PLATE I

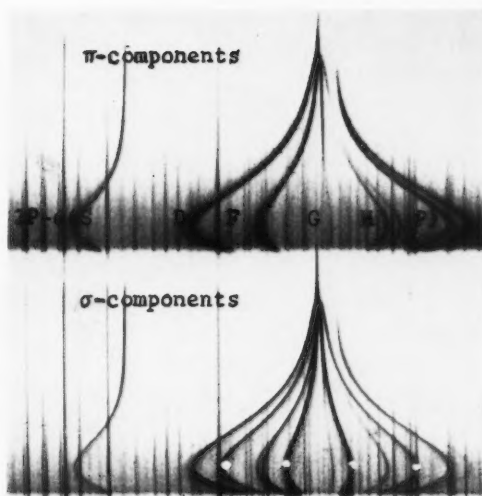
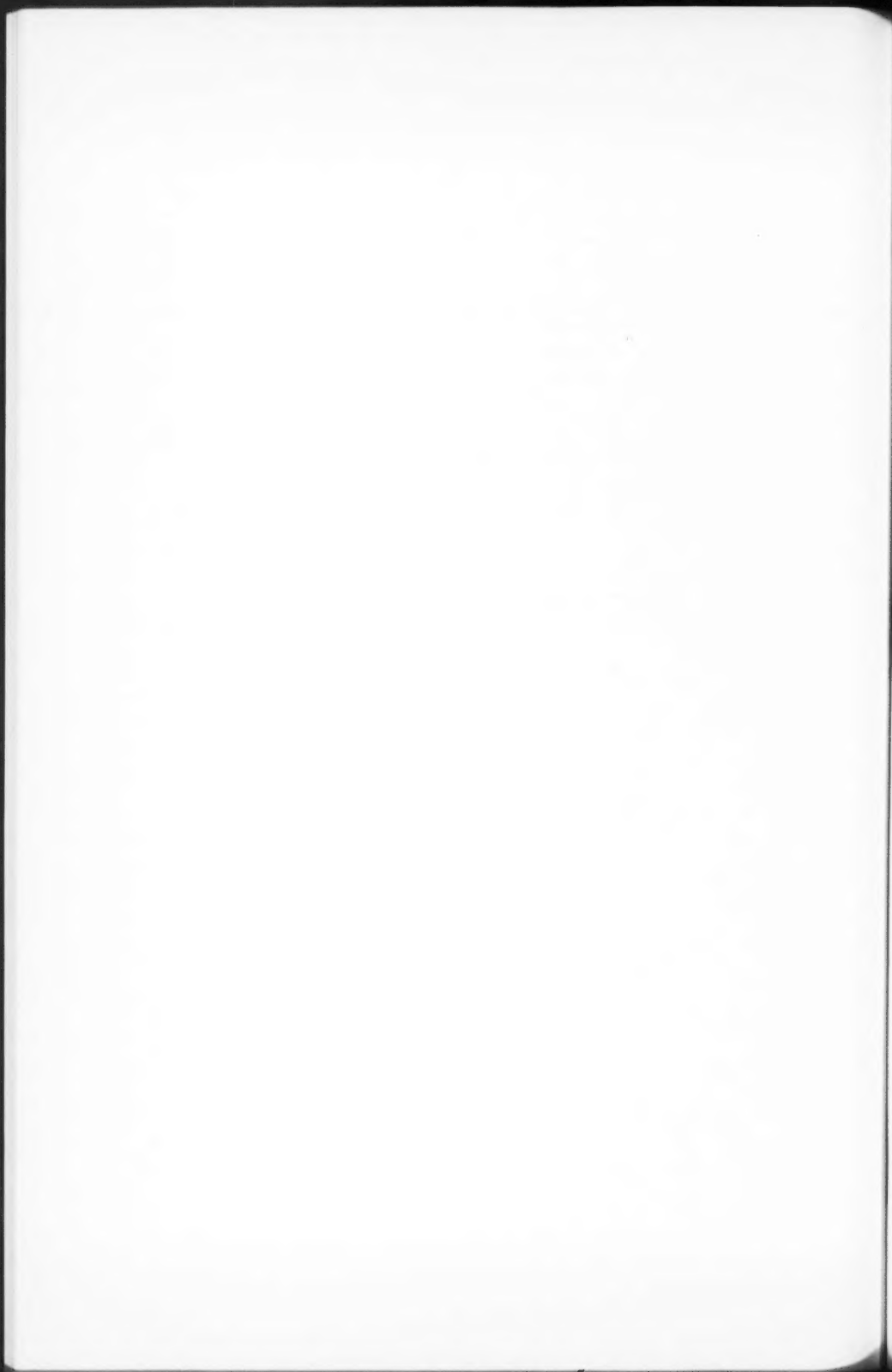


FIG. 1. Parhelium group 2^1P-6^1S (S, D, F, G, H, P) in external electric fields 0-85,000 v/cm. Frequencies increase toward the right.



1. For the maximum displacements, just under 100 cm^{-1} , the field is $85,000 \text{ v/cm}$. It is therefore apparent that a few thousand volts per centimeter is enough to cause the necessary displacements and bring out the new electric combination lines, corresponding to Δl equal to any possible value.

2. 2^1P-6^1P on the extreme right is a member of the first series recognized as having a complex pattern ($2\pi/2\sigma$) for each of its members in external electric fields. The pattern is characterized by a very weak outer σ component. More generally, for any parhelium transition $l' \leftrightarrow l$ the normal pattern is $(l+1)\pi/2l\sigma$ if $l' = l$ and $(l+1)\pi/(2l-1)\sigma$ if $l' > l$. A great variety of normal patterns is possible.

3. White dots mark the four, i.e. $(n-|m|)$, σ components corresponding to transitions from $|m| = 2$ initial states and these components illustrate very well the symmetry which develops as the displacements become large compared with the zero field separations. When $(n-|m|)$ is odd, however, there is a "central" component and of course the state of highest $|m|$ value is undisplaced to first approximation.

4. In the π image, 2^1P-6^1H appears to vanish as it passes under the zero field position of 2^1P-6^1P . Indeed, many components must vanish when the displacement reaches the critical value at which a factor in the intensity goes to zero.

From text books one may conclude that these well-established features are not widely known. Meantime experiments are proceeding under very high resolution.

RECEIVED JUNE 27, 1959.
RADIATION LABORATORY,
MCGILL UNIVERSITY,
MONTREAL, QUE.

LETTERS TO THE EDITOR

Under this heading brief reports of important discoveries in physics may be published. These reports should not exceed 600 words and, for any issue, should be submitted not later than six weeks previous to the first day of the month of issue. No proof will be sent to the authors.

The Function of Constitutional Supercooling in Crystal Growth

This letter is a comment intended to correct one basic misconception presented in a recent paper by J. S. Kirkaldy on "Crystal growth and the thermodynamics of irreversible processes" (Kirkaldy 1959). It concerns itself only with the conclusions that the author makes with respect to the existence of constitutional supercooling in the liquid ahead of cellular or dendritic interface morphologies. Kirkaldy concludes, erroneously, that constitutional supercooling is eliminated at the cell caps as a necessary consequence of the minimum entropy production condition. It will be shown here that such a conclusion is unwarranted since it necessitates a violation of one of the boundary conditions of the problem.

The principle of minimum rate of entropy production in non-equilibrium systems, like the principle of minimum free energy in equilibrium systems, presents the optimum thermodynamic state of the system but it does not indicate the probability of reaching this state in a finite time. A severely segregated freezing crystal exhibits a lower rate of entropy production than a crystal freezing homogeneously and is therefore preferred (Kirkaldy 1959). However, if no constitutional supercooling exists in the liquid, the interface remains planar and the crystal is homogeneous, i.e., the crystal continues to freeze in a non-optimum manner. At a certain degree of constitutional supercooling a cellular interface forms and a segregated crystal is produced. It is through the existence of constitutional supercooling that the desired end state is reached. It will be shown in a later publication (Bolling and Tiller, to be published) that cells will only form if the caps are stable at a higher temperature than a planar interface. Because of the change in equilibrium temperature due to curvature, this will only occur when a critical degree of constitutional supercooling is reached.

The interface morphology does not change in order to eliminate the constitutional supercooling, although the author was once of this opinion, the interface morphology changes through the aid of the constitutional supercooling to produce the segregated state of lower rate of entropy production. In fact very little constitutional supercooling is eliminated when cells form. Rather than carry out a rigorous treatment of the problem it may be simply shown that, for most growth conditions, constitutional supercooling cannot be eliminated at the cell caps without violating the flux condition at the cell caps.

The solute flux condition at the cell caps is

$$(1) \quad R(1-k)C = -D \text{ grad } C,$$

where R is the rate of freezing, k the solute partition coefficient between the two phases, D the diffusion coefficient, and C the solute concentration in the liquid. The concentration C is given by $C = C_0 + \Delta C$, where C_0 is the concentration far from the interface and ΔC is the build-up at the interface. For a planar interface $\Delta C = C_0(1-k)/k$ so that $\Delta C = C_0$ for $0.5 \leq k \leq 1$, which is the case for Sn as solute in Pb. For a cellular interface $\Delta C = \alpha C_0(1-k)/k$ where $\alpha < 1$. The condition of zero constitutional supercooling at the interface is given by

$$(2) \quad m_L \text{ grad } C = \text{grad } T,$$

where m_L is the liquidus slope. Now let R and $\text{grad } T$ be adequate for cell formation with Pb+10⁻² wt.% Sn. With the same R and $\text{grad } T$ it is obvious that for Sn in Pb equations (1) and (2) cannot be simultaneously satisfied with $C_0 > 2 \times 10^{-2}$ wt.%. Thus, constitutional supercooling cannot possibly be eliminated at the caps of cells for most growth conditions if $C_0 > 10^{-1}$ wt.%. For example, if $C_0 = 1$ wt.%, $m_L \text{ grad } C \sim 10 \text{ grad } T$ for normal freezing conditions.

The general conclusion must be that cells will adopt that morphology compatible with thermal and constitutional constraints that produces the minimum rate of entropy production. The constitutional supercooling acts as a bridge for this morphology change. After the interface morphology change the constitutional supercooling still remains.

BOLLING, G. F. and TILLER, W. A. To be published.

KIRKALDY, J. S. 1959. Can. J. Phys. 37, 739.

RECEIVED AUGUST 4, 1959.
DEPARTMENT OF METALLURGY,
WESTINGHOUSE ELECTRIC CORPORATION,
PITTSBURGH 35, PENNSYLVANIA.

W. A. TILLER

Can. J. Phys. Vol. 37 (1959)

Zero Spin of the 1265-keV State in Pt^{194}

It is known that the first two excited states of Pt^{194} at 328 and 621 keV have spin 2 and even parity (Johns and Nablo 1954; Mandeville, Varma, and Saraf 1955). The purpose of this letter is to present angular correlation evidence that the third excited state at 1265 keV has zero spin and, presumably, even parity. The spin sequence, 0-2-2-0, in this nuclide is therefore identical with that in Os^{188} (King and Johns 1959) and this zero level represents the second example of the existence of beta vibrations in the region of intermediate coupling between the rare earth nuclei and those near the 126-neutron closed shell.

Neutron irradiation of iridium produces 70-day Ir^{192} and 19-hour Ir^{194} . While most of the Ir^{194} nuclei decay directly to the ground state of Pt^{194} , the Ir^{192} nuclei all decay via cascading gamma rays. Thus even with iridium enriched to 89% in Ir^{192} , the gamma-gamma coincidences from Ir^{192} are not negligible. One-milligram samples of enriched iridium metal sealed in small quartz vials were irradiated in the Brookhaven reactor for 3 hours and used in an unopened condition. For each cascade of interest the angular correlation function was recorded with carefully centered "point" sources for nine angles between 90° and 270° using equipment described in an earlier publication (King and Johns 1959). Solid angle corrections, for the $1\frac{1}{2}$ in. \times 2 in. NaI (TI) crystals used, were experimentally determined, using the method described by Lawson and Fraunfelder (1953), for a series of gamma-ray energies from 129 to 1330 keV.

Since both the 937-328- and 643-621-keV cascades start from the 1265-keV level in Pt^{194} and involve spin sequences of the form $J-2-0$, one might expect the correlation functions for these cascades to be identical in an ideal experiment. Unfortunately, the resolution of a scintillation spectrometer is insufficient to make possible a clean separation of the many radiations present and so corrections must be made for competing cascades.

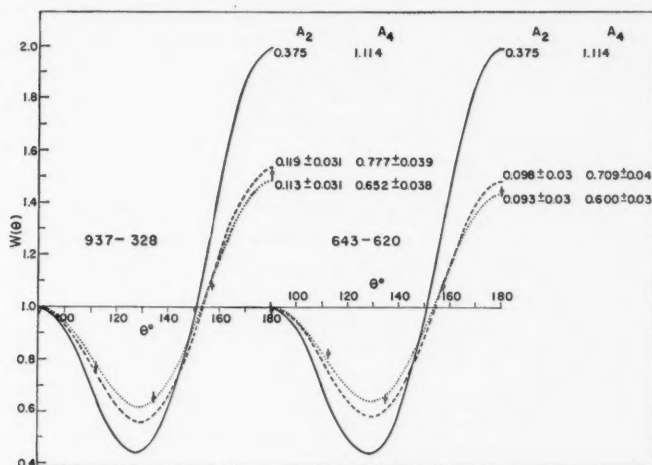


FIG. 1. Angular correlation functions for the two cascades depopulating the 1265-keV level in Ir^{194} . The dotted curves show the least-squares fit to the experimental points. The dashed curves are the same corrected for the finite solid angle of the detectors. The solid curves are the expected theoretical functions.

The single-channel spectrum obtained in this work was very similar to that presented in Fig. 2 of Mandeville's paper referred to above and is not shown here. Data was recorded with the scintillation spectrometers set to register coincidences between the following portions of the single-channel spectrum: 621-643-keV photopeak with itself, 328-keV photopeak with the 937-keV photopeak, and 328-keV photopeak with the entire spectrum above 1000 keV. From the results of the last-mentioned pair, an estimate of the contribution to the observed 328-937 coincidence rate from competing cascades can be made. Figure 1 presents the experimental correlation data after the subtraction of a small correction ($<10\%$) for accidental coincidences, together with the least-squares fit to the experimental points.

The figure also shows the experimental curves corrected for the finite solid angles of the detectors and the theoretical curve expected for a 0-2-0 cascade. Before the solid angle

corrected curves are compared with theory, they must be adjusted for the effects of competing cascades in Ir^{192} and Ir^{194} . The data available shows that the subtraction of these effects accentuates the anisotropy of the curves of Fig. 1. Using our best estimates of these corrections, the value of $W(130)$ is depressed to 0.5 while $W(180)$ is raised to 1.75. Because the magnitudes of these corrections are somewhat uncertain, we have preferred to publish only our experimental curves and draw our conclusions from them.

The two cascades under investigation are both of the form $J-2-0$ where J has an integral value less than 5. The only choice for J which gives a large positive A_4 coefficient is zero; none of the other choices of J give correlation functions resembling the experimental ones. Thus despite the rather poor agreement between the experimental coefficients and the theoretical coefficients for a $0-2-0$ cascade, one can conclude with confidence that the 1265-kev state has zero spin. A consideration of the intensities of the beta rays feeding this level suggests that its parity is even, though this conclusion cannot be drawn from the present experiment.

These results were presented to the fourteenth congress of the Canadian Association of Physicists early in June, 1959. The authors would like to acknowledge a recent communication from Dr. Marklund of Uppsala describing work on Ir^{194} which he presented to the Stockholm conference during the same week. His conclusions are in agreement with ours.

- JOHNS, M. W. and NABLO, S. V. 1954. *Phys. Rev.* **96**, 1599.
KING, W. J. and JOHNS, M. W. 1959. *Can. J. Phys.* **37**, 755.
LAWSON, J. S. and FRAUENFELDER, H. 1953. *Phys. Rev.* **91**, 649.
MANDEVILLE, C. E., VARMA, J., and SARAF, B. 1955. *Phys. Rev.* **98**, 94.

RECEIVED AUGUST 10, 1959.
DEPARTMENT OF PHYSICS,
McMASTER UNIVERSITY,
HAMILTON, ONTARIO.

M. W. JOHNS
J. D. MACARTHUR

THE PHYSICAL SOCIETY

MEMBERSHIP of the Society is open to all who are interested in Physics. FELLOWS pay an Entrance Fee of £1 1s. (\$3.15) and an Annual Subscription of £2 2s. (\$6.00).

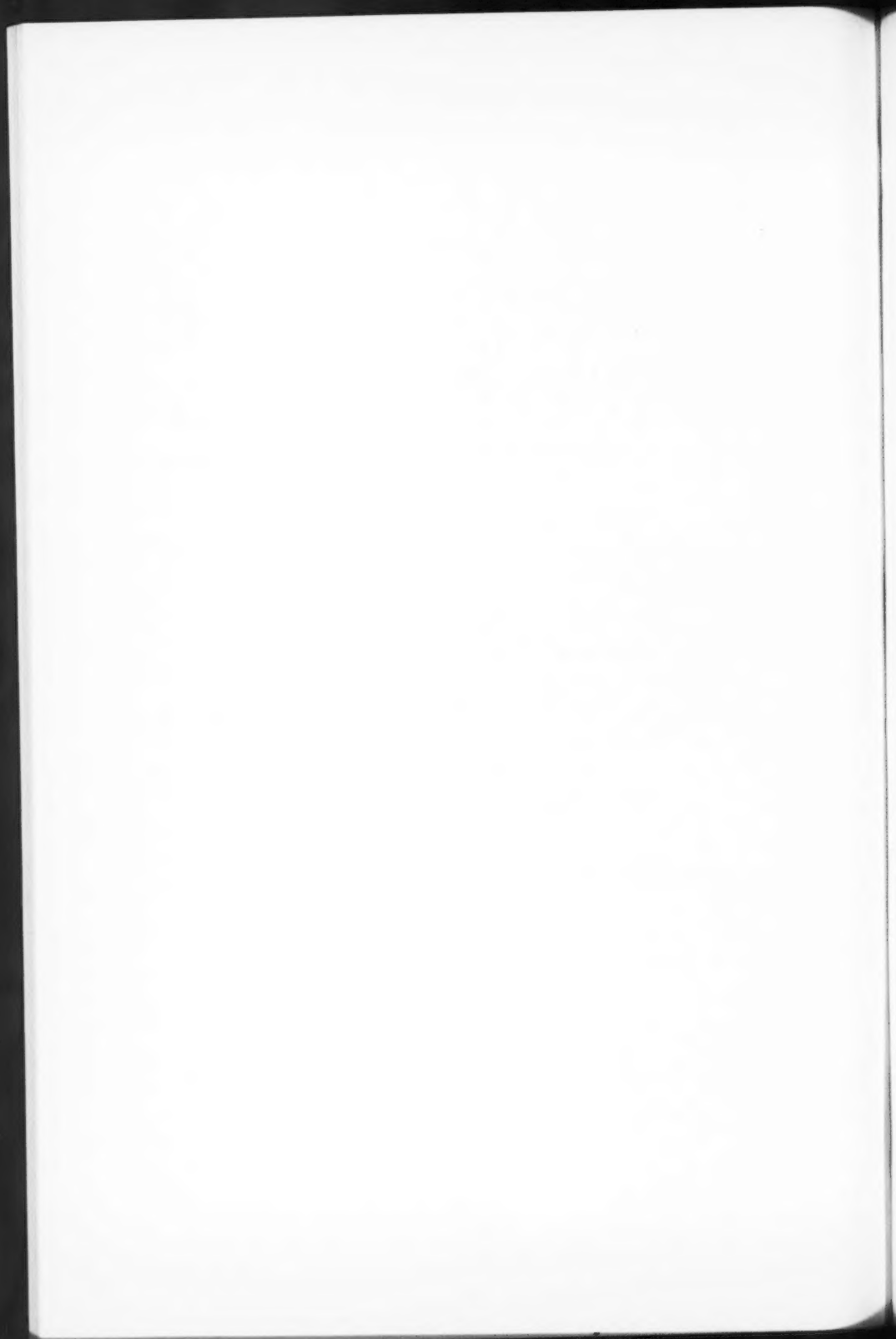
STUDENTS: A candidate for Studentship must be between the ages of 18 and 26, and pays an Annual Subscription of 5s. (\$0.75).

MEETINGS: Fellows and Students may attend all Meetings of the Society including the annual Exhibition of Scientific Instruments and Apparatus.

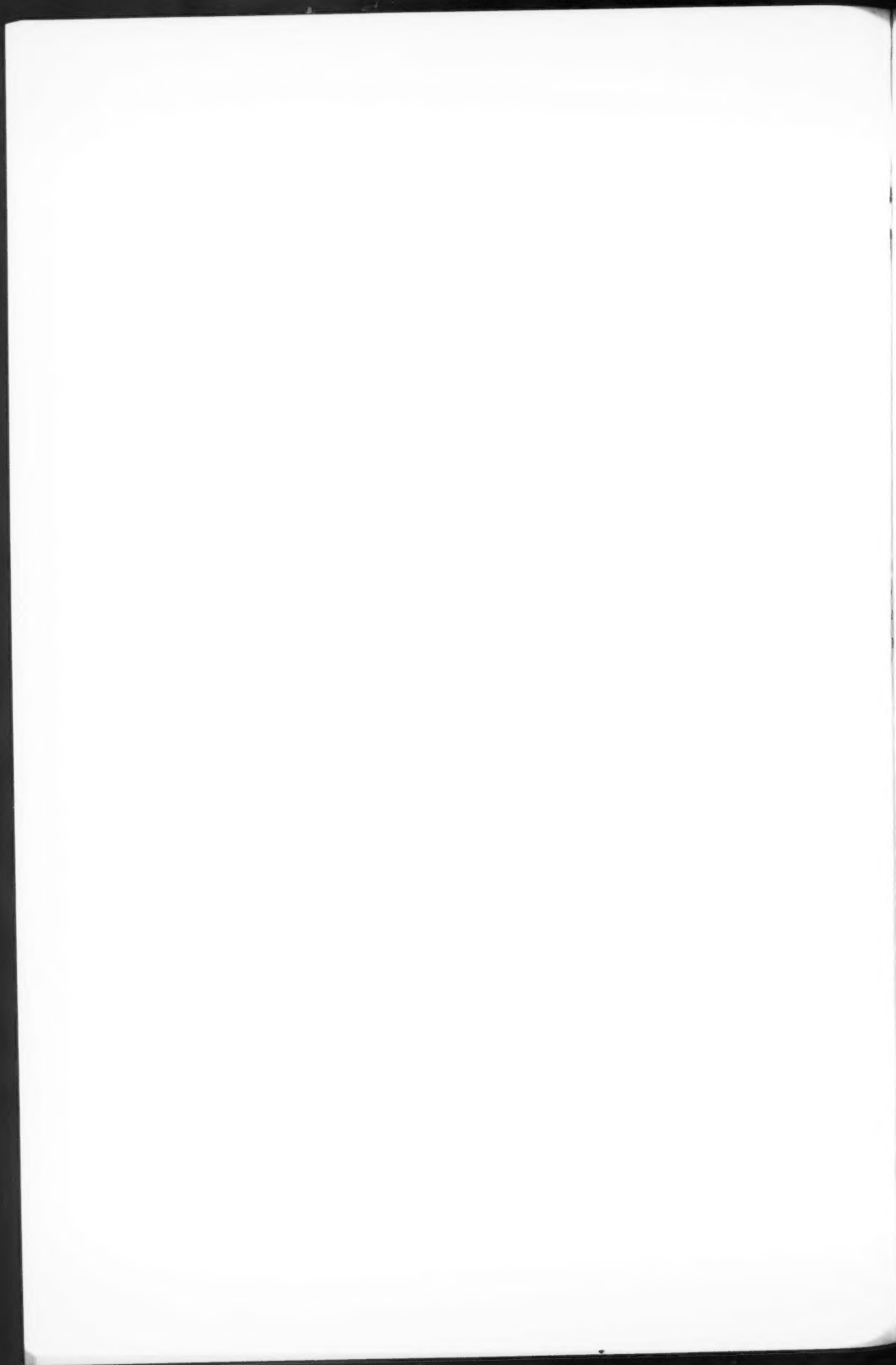
PUBLICATIONS include the *Proceedings of the Physical Society*, published monthly, and *Reports on Progress in Physics*, published annually. Volume XXI, 1958, is now available (price £3 3s. (\$9.45)). Members are entitled to receive any of the Publications at a reduced rate.

Further information can be obtained from:

THE PHYSICAL SOCIETY
1, LOWTHER GARDENS, PRINCE CONSORT ROAD
LONDON, S.W.7, ENGLAND







NOTES TO CONTRIBUTORS

Canadian Journal of Physics

MANUSCRIPTS

General.—Manuscripts, in English or French, should be typewritten, double spaced, on paper $8\frac{1}{2} \times 11$ in. **The original and one copy are to be submitted.** Tables and captions for the figures should be placed at the end of the manuscript. Every sheet of the manuscript should be numbered. Style, arrangement, spelling, and abbreviations should conform to the usage of recent numbers of this journal. Greek letters or unusual signs should be written plainly or explained by marginal notes. Characters to be set in boldface type should be indicated by a wavy line below each character. Superscripts and subscripts must be legible and carefully placed. Manuscripts and illustrations should be carefully checked before they are submitted. Authors will be charged for unnecessary deviations from the usual format and for changes made in the proof that are considered excessive or unnecessary.

Abstract.—An abstract of not more than about 200 words, indicating the scope of the work and the principal findings, is required, except in Notes.

References.—References should be listed **alphabetically by authors' names**, unnumbered, and typed after the text. The form of the citations should be that used in current issues of this journal; in references to papers in periodicals, titles should not be given and only initial page numbers are required. The names of periodicals should be abbreviated in the form given in the most recent *List of Periodicals Abstracted by Chemical Abstracts*. All citations should be checked with the original articles and each one referred to in the text by the authors' names and the year.

Tables.—Tables should be numbered in roman numerals and each table referred to in the text. Titles should always be given but should be brief; column headings should be brief and descriptive matter in the tables confined to a minimum. Vertical rules should not be used. Numerous small tables should be avoided.

ILLUSTRATIONS

General.—All figures (including each figure of the plates) should be numbered consecutively from 1 up, in arabic numerals, and each figure referred to in the text. The author's name, title of the paper, and figure number should be written in the lower left corner of the sheets on which the illustrations appear. Captions should not be written on the illustrations.

Line drawings.—Drawings should be carefully made with India ink on white drawing paper, blue tracing linen, or co-ordinate paper ruled in blue only; any co-ordinate lines that are to appear in the reproduction should be ruled in black ink. Paper ruled in green, yellow, or red should not be used. All lines must be of sufficient thickness to reproduce well. Decimal points, periods, and stippled dots must be solid black circles large enough to be reduced if necessary. Letters and numerals should be neatly made, preferably with a stencil (**do NOT use typewriting**) and be of such size that the smallest lettering will be not less than 1 mm high when the figure is reduced to a suitable size. Many drawings are made too large; originals should not be more than 2 or 3 times the size of the desired reproduction. Whenever possible two or more drawings should be grouped to reduce the number of cuts required. In such groups of drawings, or in large drawings, full use of the space available should be made; the ratio of height to width should conform to that of a journal page ($4\frac{1}{2} \times 7\frac{1}{2}$ in.), but allowance must be made for the captions. **The original drawings and one set of clear copies (e.g. small photographs) are to be submitted.**

Photographs.—Prints should be made on glossy paper, with strong contrasts. They should be trimmed so that essential features only are shown and mounted carefully, with rubber cement, on white cardboard, with no space between those arranged in groups. In mounting, full use of the space available should be made. **Photographs are to be submitted in duplicate**; if they are to be reproduced in groups one set should be mounted, the duplicate set unmounted.

REPRINTS

A total of 50 reprints of each paper, without covers, are supplied free. Additional reprints, with or without covers, may be purchased at the time of publication.

Charges for reprints are based on the number of printed pages, which may be calculated approximately by multiplying by 0.6 the number of manuscript pages (double-spaced typewritten sheets, $8\frac{1}{2} \times 11$ in.) and including the space occupied by illustrations. Prices and instructions for ordering reprints are sent out with the galley proof.

Contents

<i>R. W. Smith</i> —The grey tin \rightleftharpoons white tin transition in tin-mercury alloys - -	1079
<i>Robert W. Williams</i> —Heavy-liquid chambers - - - - -	1085
<i>K. L. Chopra and T. S. Hutchison</i> —Ultrasonic attenuation in superconducting and normal mercury - - - - -	1100
<i>J. P. Hobson</i> —First adsorbed layer of nitrogen on pyrex at 77.4° K - - - -	1105
<i>M. J. Laubitz</i> —Design of gradientless furnaces - - - - -	1114
<i>C. H. Millar, T. A. Eastwood, and J. C. Roy</i> —The decay of Bi ²⁰⁸ - - - -	1126
<i>T. R. Hartz</i> —Radio star scintillations and ionospheric disturbances - - -	1137
<i>H. J. Hay and J. B. Warren</i> —The photodisintegration of neon - - - -	1153
<i>H. M. Bradford, D. M. Fraser, G. F. O. Langstroth, and A. D. MacDonald</i> —Electrical breakdown in xenon and krypton at ultrahigh frequencies - -	1166
<i>R. N. Dixon</i> —The 0-0 and 1-0 bands of the $A(^3\Pi_1)-X(^3\Sigma^-)$ system of NH - -	1171
<i>J. Van Kranendonk and Z. J. Kiss</i> —Theory of the pressure-induced rotational spectrum of hydrogen - - - - -	1187
Notes:	
<i>Kamal K. Seth</i> —A note on <i>s</i> -wave average neutron cross sections - - -	1199
<i>J. S. Foster</i> —Notes on a photograph of the Stark effect - - - - -	1202
Letters to the Editor:	
<i>W. A. Tiller</i> —The function of constitutional supercooling in crystal growth	1204
<i>M. W. Johns and J. D. MacArthur</i> —Zero spin of the 1265-kev state in Pt ¹⁹⁴	1205

